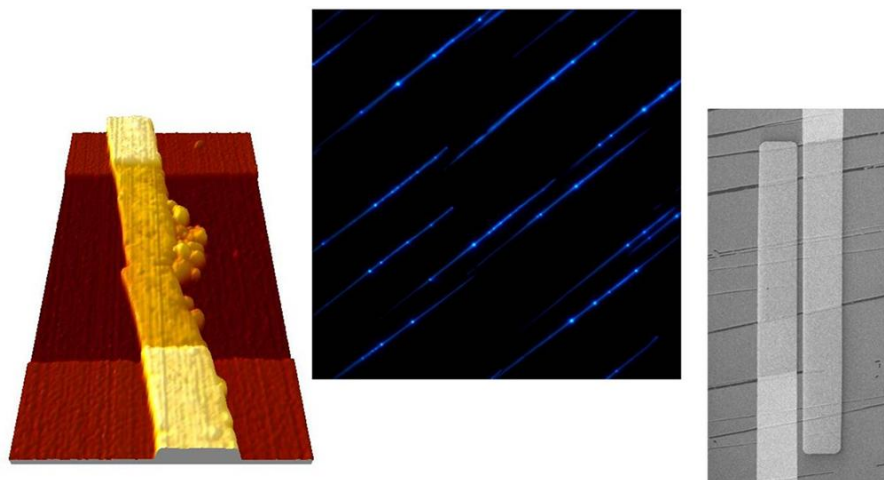


Growth and Integration of Organic Nanofibers in Devices

Ph.D. Thesis

Mads Clausen Institute
University of Southern Denmark



Kasper Thilasing-Hansen

July 26, 2010

Front side images:

- (Left) $1.6 \times 3 \mu\text{m}^2$ atomic force microscope image of a p6P nanofiber with gold electrodes on top.
- (Middle) $100 \times 100 \mu\text{m}^2$ fluorescence image of p6P nanofibers.
- (Right) $60 \times 120 \mu\text{m}^2$ scanning electron microscope image of p6P nanofibers between gold electrodes

Preface

This thesis has been submitted as a partial fulfillment of the requirements to obtain a Ph.D. degree at the University of Southern Denmark (SDU). The main part of the work has been carried out at Mads Clausen Institute (MCI) in Sønderborg and a smaller part at Institute of Physics (SDU) in Odense. During this project period I have in the beginning been part of the NanoOptics group and later the NanoSyd group both groups presided by Professor Horst-Günter Rubahn.

I started my Ph.D. in October 1, 2005 as a part of the Institute of Physics at SDU in Odense. In autumn 2006 to spring 2007 all equipment related to the NanoOptics group was packed and re-installed at the new university facility "Alsion" in Sønderborg, where my supervisor Horst-Günter Rubahn was appointed as head of the new research center NanoSyd, which included the new cleanroom research facility at Alsion. From October 1, 2007 to January 31, 2009 I had a leave from my Ph.D. in order to fulfill a technical position at the cleanroom facility, being responsible for installation of new process equipment inside the cleanroom and making the entire cleanroom fulfill the stringent specifications, which is required in order to run such a research facility. On the negative side, these aspects have of course interrupted my Ph.D. period, but on the positive side it has given me a very useful insight in running and using a cleanroom research facility.

The project has been supervised by Professor Horst Günter Rubahn and was financed by the University of Southern Denmark. The project should be seen as first attempt in an up-scaled implementing of organic para-hexaphenylene nanofibers in devices. To derive full benefit of this thesis, the reader should possess basic knowledge of molecular and solid state physics. Apart from this thesis, a number of publications have also been made related to this project. These are listed in appendix A.

I am grateful to a number of people for their help, support and collaboration during this project. First of all I like to thank my supervisor Horst-Günter Rubahn for his support in editing this report and valuable scientific discussions. I like to thank all the members of the NanoSyd group. In particular, I like to thank Jakob Kjelstrup-Hansen for his tremendous support both scientifically as well as personally. Especially, Jakobs support in device fabrication, scientific discussions and editing of this report has been very valuable. I like to thank Luciana Tavares for collaborating on implementing nanofibers in optoelectronic devices, Frank Balzer for valuable discussions regarding nanofiber growth and Vladimir Bordo for answering questions regarding plasmonics.

I am grateful to Ph.D. student Till Leissner and Professor Michael Bauer from the Christian-Albrechts University of Kiel for the opportunity to use the PEEM setup and the collaboration and help in obtaining and analyzing data.

Finally, I like to thank my family and friends for their support and encouragement. Especially, I like to thank and apologize to my lovely wife, Rikke, and my two wonderful kids, Ida and Emma, for me being absent during the last part of this project.

July 26, 2010

Kasper Thilsing-Hansen
Mads Clausen Institute - University of Southern Denmark
Alsion 2
DK-6400 Sønderborg
Denmark

Abstract

This report focuses on transfer of larger areas of mutually aligned organic *para*-hexaphenylene (p6P) nanofibers from their growth substrate muscovite mica onto pre-structured device platforms. In order to fulfill functionality of the devices, the morphology of the nanofibers has to fulfill specific requirements, e.g. certain width to length ratios. Thus nanofiber growth on larger muscovite mica substrates is an important issue, which is also covered in this report. The three main topics in this report are:

1. Large scale growth of p6P nanofibers.
2. Transfer of p6P nanofibers.
3. Device integration of p6P nanofibers, exemplified by *field effect transistor* (FET), plasmon polariton coupling and security marker substrates.

The morphologies (lengths, heights and widths) of p6P nanofibers grown on a muscovite mica substrate depend strongly on the muscovite mica substrate temperature during growth. Especially, growing p6P nanofibers on large muscovite mica substrates complicates the heating procedure of the mica substrate due to the poor thermal conductivity of muscovite mica. A homogeneous muscovite mica surface temperature has been achieved by adding a thermally conductive layer between the mica and a hotplate. Together with a precise measurement of the mica surface temperature, resulting in a critical temperature of 453 K, a quantitative control of the mica surface temperature has been achieved, which in turn led to growth of homogeneously distributed p6P nanofibers on 75x25mm² muscovite mica substrates. In addition to that, *atomic force microscope* (AFM) images have revealed that a p6P nanofiber grown at the critical temperature not only originates from 3-dimensional p6P crystallites forming a 1-dimensional crystallite chain, but also from 1-dimensional crystallite chains adding to the already existing p6P nanofiber.

Transfer of p6P nanofibers from their growth substrate is inevitable in order to implement p6P nanofibers in devices. Controlled transfer of 200x200μm² nanofiber areas from the growth substrate to prefabricated silicon substrates has been achieved with an orientation control of ±5° by a novel stamping technique in an air atmosphere with defined temperature and humidity. *Atomic force microscopy* (AFM) images reveal a distortion of transferred p6P nanofibers in terms of height and width: the nanofiber height is reduced by a factor two and the width is correspondingly increased by a factor two. This distortion is inevitable using mechanical stamping techniques.

Subsequently, arrays of mutually aligned p6P nanofibers have been implemented in devices. Firstly, as simple ordered arrays on holograms, serving as a new generation of anti-counterfeit markers. Secondly, into a prefabricated, Silicon based FET device using the novel stamping technique. Electrical contact to transferred nanofibers has been achieved for both top and bottom configurations of the FET device. Finally, nanofibers have been integrated on a prefabricated structured gold-on-silicon sample, serving as *surface plasmon polariton* (SSP) active substrate. *Photoemission electron microscopy* (PEEM) images of transferred p6P nanofibers on such substrates have been obtained. These include images where *surface plasmon polaritons* (SPPs) are excited in the gold/vacuum interface by a pulsed laser beam, resulting in nanofiber localized beating patterns in the PEEM images.

Dansk Resumé

Denne rapport fokuserer på overførsel af større områder af gensidigt parallel organiske para-hexaphenylene (P6P) nanofibers fra deres vækst substrat moskovitiske glimmer til præstruktureret komponent platforme. For at opfylde komponentens funktionalitet, stilles særlige krav til nanofibrenes morfologi, f.eks. et vist forhold mellem bredde og længde. Således er nanofiber vækst på større moskovitiske glimmer substrater et vigtigt forhold, som også er omfattet af denne rapport. De tre hovedemner i denne rapport er:

1. Para-hexaphenylene (p6P) nanofiber vækst på større moskovitiske glimmer substrater.
2. Overførsel af p6P nanofibre.
3. Integration af p6P nanofibre i komponenter, eksemplificeret ved felt effekt transistor (FET), plasmon polariton kobling og sikkerhedsmarkør substrater.

Morfologien (længde, højde og brede) af p6P nanofibre groet på moskovitisk glimmer er stærkt afhængig af det moskovitiske glimmers temperatur under væksten. Især p6P nanofibre groet på store moskovitiske glimmer substrater komplicerer opvarmningsproceduren pga. glimmer substratets ringe varmeledningsevne. En homogen overfladetemperatur af moskovitiske glimmer er opnået ved at tilføje et termisk ledende lag mellem glimmeret og en varmeplade. Sammen med en præcis måling af glimmer overfladetemperatur, hvilket resulterede i en kritisk temperatur for nanofiber vækst på 453 K, er en kvantitativ kontrol af glimmer overfladetemperatur opnået, hvilket igen førte til vækst af ensartet fordelt p6P nanofibre på 75x25mm² moskovitiske glimmer substrater. Udover dette afslørede atomar kraft mikroskop (AFM) billeder, at en p6P nanofiber groet ved den kritiske temperatur ikke kun stammer fra 3-dimensionelle p6P krystalliter, der danner en 1-dimensionel kæde af krystalliter, men også fra 1-dimensionelle kæder af krystalliter, der tilslutter sig den allerede eksisterende P6P nanofiber.

Overførsel af P6P nanofibre fra deres vækst substrat er uundgåeligt for at implementere p6P nanofibre i komponenter. Kontrolleret overførsel af 200x200µm² nanofiber områder fra vækst substratet til præfabrikerede silicium substrater er opnået med en kontrol af nanofibrenes orientering på $\pm 5^\circ$, vha. af en ny stempingsteknik i en atmosfære med veldefineret temperatur og luftfugtighed. Atomar kraft mikroskop (AFM) billeder viser en fordrejning af det oprindelige højde-bredde forhold ved overførte p6P nanofibre: nanofiber højden er reduceret med en faktor to og bredden er tilsvarende steget med en faktor to. Denne fordrejning er uundgåelig ved brug af mekanisk stempingsteknikker.

Efterfølgende er områder med gensidigt parallelle p6P nanofibre blevet implementeret i komponenter. Første som simple ordnede områder af nanofibre på hologrammer, der tjener som en ny generation af sikkerhedsmarkører. Derefter i præstrukturerede, silicium baseret FET komponenter vha. den nye stempingsteknik. Elektrisk kontakt til overførte nanofibre er opnået for både top- og bundkontakt konfigurationer af FET komponenten. Endelig er nanofibre blevet implementeret på en præstruktureret guld-på-silicium prøve, der tjener som et overflade plasmon polariton (SSP) aktivt substrat. Fotonemission elektron mikroskop (PEEM) billeder af overførte p6P nanofibre på disse substrater er opnået. Disse billeder omfatter, overflade plasmon polaritoner (SPPs) exciteret med en pulserende laserstråle et guld/vakuum interface, hvilket resulterer i nanofiber lokaliseret mønstre i PEEM billederne.

Contents

Preface	3
Abstract	5
Dansk Resumé	7
1 Introduction	13
1.1 Bottom-up technology.....	13
1.1.1 1-Dimensional nanostructures	14
2 Large Scale Nanofiber Growth	17
2.1 Growth theory	18
2.1.1 Para-HexaPhenyl	18
2.1.2 Muscovite mica	19
2.1.3 Para-HexaPhenyl on muscovite mica	20
2.2 Experimental setup.....	22
2.2.1 Vacuum system	23
2.2.2 Heating system.....	23
2.2.3 p6P oven.....	26
2.2.4 Nanofiber growth procedure	26
2.3 Experimental results	27
2.3.1 Homogeneity and critical temperature.....	27
2.3.2 Wetting layer, crystallites and nanofiber clustering	29
2.3.3 Annealing and breaks	31
2.4 Summary and outlook	33
3 Transfer and Integration of p6P Nanofibers	35
3.1 Introduction to nanofiber stamping	35
3.2 Nanofiber stamping machine	37
3.3 Experimental results	40
3.3.1 Temperature and humidity dependence	40
3.3.2 Distortion of transferred nanofibers	44
3.4 Large scale transfer of nanofibers to foil.....	46
3.4.1 Transferring nanofibers to foil.....	46

3.5	Summary and outlook	48
4	Electrical Properties of p6P Nanofibers.....	51
4.1	Principle of Organic Field Effect Transistors	51
4.1.1	Organic Light Emitting Field Effect Transistors	53
4.2	Field effect transistor device design	54
4.2.1	Nanofiber field effect transistor.....	55
4.3	Electrical characterization setup	57
4.4	Experimental results.....	57
4.5	Summary and outlook	60
5	Plasmon coupling to p6P Nanofibers	61
5.1	Surface plasmon polariton theory.....	61
5.2	Experimental setup.....	64
5.3	Sample preparation	65
5.4	Experimental results.....	66
5.4.1	Intensity pattern analysis	68
5.5	Summary and outlook	73
6	Another application	75
6.1	Organic nanofibers as security markers	75
6.1.1	Levels of security	77
6.2	Summary and outlook	79
7	Conclusion	81
A	List of Publications.....	83
	Refereed papers	83
	Book article.....	83
	Refereed proceedings.....	83
	Conference abstracts.....	84
B	Process Recipe	87
	Nanofiber transfer test substrate	87
	Field Effect Transistor (FET) device for bottom contact configuration.....	88
	Field Effect Transistor (FET) device for top contact configuration	90
	PEEM sample	91
C	Mechanical drawings	93

Hotplate	93
Sample holder	95
Stamp box	97
Bibliography.....	101

Chapter 1

1 Introduction

The invention of semiconducting circuits from the middle of last century led to the revolutionary development of computers and an increasing demand for miniaturized electronic circuits arose. This led to the age of microtechnology and in the last decade nanotechnology. The standard top-down technology for fabrication of microelectronic circuit is today pushed close to its limits. The patterning technology used today is deep UV lithography (patterning wavelength of 193nm), which can allow structure sizes in the order of 50nm [1]. This is limited by the diffraction effect that occurs in a wave based patterning technique. Much effort is dedicated to continue the down scaling by additional improvements such as the use of immersion lithography to increase the numerical aperture, thereby lowering the diffraction limit. This has further pushed down the resolution around 30nm [2]. Further reduction in feature size will be a huge obstacle with light based lithography techniques and alternative methods are therefore under much investigation. One route is to continue in the resist based top-down technology. This includes *electron beam lithography* (EBL) [3] which can provide resolutions in the few nanometer range, but which is not interesting for large scale industrial applications, due to low throughput. Also *nanoimprint lithography* (NIL) has drawn much attention, due to its ability to pattern large areas with high resolution and high throughput [4], but still technical challenges remaining.

1.1 Bottom-up technology

An alternative strategy is the bottom-up technology, where structures in the nanometer range (also called nanostructures) are grown from the bottom and up, with individual molecules or atoms as building blocks. The size of these structures are not defined by any patterning technique, but are basically limited by the size of their individual building blocks and the technique of which they are grown. Depending on the type of nanostructure, its size, shape and physical properties can be controlled by the use of special growth conditions (such as temperature, pressure, electric field etc.) and particular building blocks which in the case of molecular nanostructures can be tailored via synthetic chemistry. This has opened for novel classes of materials e.g. 1-dimensional (1-D) nanostructures, such as nanotubes and nanowires [5, 6] and 0-D nanostructures, such as quantum dots [7], with unique electrical and optical properties. In the past there have been some argument of what the terms nanotechnology and nanostructure cover, but a general definition of 0-D nanostructures is that it encompasses structures with side lengths less than 100nm in all three dimensions, and 1-D nanostructures are

structures with side lengths less than 100nm in two dimensions [8]. Even though bottom-up nanotechnology has not had a huge commercial breakthrough as foreseen entering the new century, nanotechnology is still perceived as the technology of the future.

1.1.1 1-Dimensional nanostructures

In the recent years 1-D nanostructures have drawn a lot of attention within the scientific community, due to their large application potential within the fields of e.g sensing [9, 10, 11, 12], electronics [13, 14], photovoltaic's [15, 16] and optoelectronics and photonics [17, 18]. A major field of research has been inorganic semiconducting nanowires pioneered by Charles Lieber, Peidong Yang and Lars Samuelson. Such nanowires have electrical and optical properties that can be used in the fields of electronics, optics and photonics. Some of this research has included the development of methods to integrate such nanowires into device platforms [19], by transferring the nanowires from their growth substrates. This is an important step in the ability to implement such devices on a high volume basis.

Another novel class of 1-D nanostructures is organic, molecular-based nanostructures, such as self-assembled Perylenetetracarboxyldiimide (PTCDI) based nanowires showing intriguing properties in the field of *Organic Field Effect Transistors* (OFET) [20]. Yet another class of organic 1-D nanostructures, that have drawn a lot of attention, is oligomer based nanowires, due to their interesting optical, electrical and optoelectrical properties. Especially rod-like molecules, such as pentacene [21], oligo-thiophenes [22] and oligo-phenylenes [23] built-up by π -conjugated systems, are among the most studied. One of these oligo-phenylene, para-hexaphenylene (p6P), has been reported to grow elongated and mutual parallel 1-D nanostructures, also known as organic para-hexaphenylene nanofibers or just p6P nanofibers, on a heated and freshly cleaved muscovite mica substrate [24]. These particular p6P nanofibers and its implementation in devices will be the main topic of this report.

It has previously been demonstrated that p6P nanofibers can be transferred from the growth substrate, muscovite mica, to any desired substrate by means of a simple drop-cast technique, and then afterwards mechanically manipulated in order to achieve the desired configuration [25]. However, large scale implementation of p6P nanofibers has so far been hindered by their soft, van-der-Waals-bonded nature that makes them very fragile.

In this work, it is demonstrated how larger areas of p6P nanofibers can be transferred from the growth substrate onto a device platform maintaining the mutual parallel nature of the nanofibers. In addition, initial investigations on nanofiber-based devices are presented; these include *Photon Emission Electron Microscopy* (PEEM) investigations of *Surface Plasmon Polaritons* (SPP) coupling to p6P nanofibers and nanofiber based *Field Effect Transistors* (FET). Large scale

growth of p6P nanofibers, together with a novel method of controlling the growth substrate temperature will also be presented. In the end of the report a more commercial use of p6P nanofibers will be presented.

It should be stated that the only organic 1-D nanostructures appearing in this work are p6P nanofibers. If the term nanofiber is used, it is implicit a p6P nanofiber.

Chapter 2

2 Large Scale Nanofiber Growth

In recent years elongated nanoscopic aggregates, also called nanofibers, based on organic phenylene oligomers have been widely investigated. Nanofibers have been fabricated on different growth substrates [26],[27], made by different organic molecules as base molecule [28] and prepared by different evaporation techniques [29], [24]. Here, the focus will be on nanofibers made from the organic oligomer para-hexaphenyl (p6P) grown on muscovite mica. These nanofibers show a range of useful applications in the field of opto-electronics, such as well defined and highly polarized blue luminescence [30], waveguiding [31] and electroluminescence [32] obtained from thin p6P film. The nanofibers are grown under high vacuum conditions (10^{-8} mbar) by Molecular Beam Epitaxy (MBE) onto a heated muscovite mica substrate, forming elongated and mutually parallel nanofibers.

The photoluminescence image in Figure 2.1 shows such a nanofiber sample on mica. It also gives an idea about the problems integrating these nanofibers in different devices. The nanofibers are mutually parallel, as mentioned earlier, but they also contain kinks and deviations in height and width as noted from *Atomic Force Microscope* (AFM) measurements. This makes it difficult to transfer and implement the nanofibers as for example the active part in an *Organic Field Effect Transistor* (OFET) structure. It is more desirable to have the nanofibers more separated, homogeneous and larger in width, height and length. In that way it is possible to investigate individual nanofibers in e.g. an OFET structure.

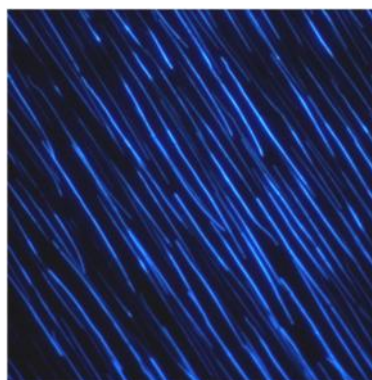


Figure 2.1: $100 \times 100 \mu\text{m}^2$ photoluminescence image of p6P nanofibers on muscovite mica.

The key challenge in controlling the nanofiber length, width and separation is to control the mica surface temperature and the deposition rate. This might sound like a trivial task, but since muscovite mica has very poor heat conductivity, the thermal contact between the mica and the heating substrate is crucial. At the same time it is desirable to grow large nanofiber samples, which makes it even more difficult, due to the poor heat conductivity of mica. This chapter will describe and resolve these issues.

2.1 Growth theory

Growth of organic para-hexaphenyl (p6P) nanofibers on muscovite mica, has been intensively investigated for the last decade. The reason for this is the quite unique formation of elongated mutual parallel nanofibers on muscovite mica, due to a fortunate match between the growth substrate (muscovite mica) and the sublimated molecule (p6P).

2.1.1 Para-HexaPhenyl

Para-hexaphenyl consists of six phenylene rings, where an isolated phenylene ring (the two-dimensional structure shown in Figure 2.2a) consists of six Carbon atoms and six Hydrogen atoms. Carbon belongs to valence group IV and an isolated Carbon atom has electron orbital structure $(1s)^2(2s)^2(2p)^2$. To form the two-dimensional phenylene ring structure the electron orbital of Carbon hybridizes to $(1s)^2(sp^2)^3(2p)$, where two of the sp^2 orbital (marked turquoise in Figure 2.2a) form strong σ -bonds between the Carbon atoms and the remaining sp^2 orbital's bond to Hydrogen atoms. The $2p_z$ orbital (marked pink in Figure 2.2a) form weak aromatic π -bond between the Carbon atoms and it is this weak aromatic π -bond which determines the *Highest Occupied Molecular Orbital* (HOMO) and *Lowest Unoccupied Molecular Orbital* (LUMO).

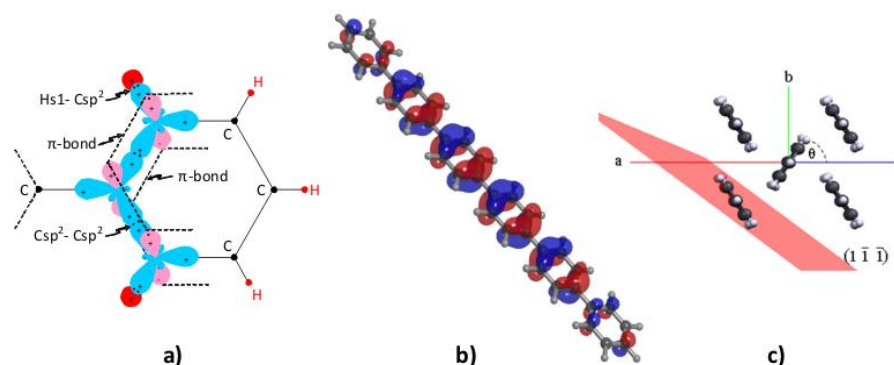


Figure 2.2: (a) A phenylene ring consist of six Carbon atoms bound together by strong σ -bonds (the Carbon sp^2 hybrid atomic orbital) and weak aromatic π -bonds (the remaining Carbon p atomic orbital). (b) Para-hexaphenyl consists of six phenylene rings bound together in a linear chain by single σ -bonds. The aromatic π -bonds determine the HOMO and LUMO levels (here the HOMO level is shown). (c) Para-hexaphenyl crystallizes in a herringbone structure with two molecules per unit cell.

If one of the Carbon sp^2 orbitals bonds to an additional phenylene ring, a linear chain of phenylene rings with single σ -bonds between them is formed. Para-hexaphenyl (shown in Figure 2.2b) consists of six such phenylene rings. Again the Carbon $2p$ orbitals make a weak, aromatic and delocalized π -bond over the entire molecule and are determinant for the energy levels around HOMO and LUMO. Figure 2.2b shows the HOMO level for *para*-hexaphenyl. Due to atomic charges on the hydrogen atoms [33] the p6P molecules crystallizes in the herringbone structure

shown in Figure 2.2c, forming layers of parallel p6P molecules with only van der Waals interaction between each layer, along the plane at the molecule end and perpendicular to the molecular long axes. In the herringbone structure the molecular long axes are parallel to each other with an angle of 66° between the molecular planes. The molecular bonding within the herringbone structure is mainly Van der Waals interaction, but also π - π interactions along the long molecular will occur between adjacent molecules [39].

The symmetry for p6P is (as for all oligophenylenes) the monoclinic space group $P2_1/c$, it has two molecules per unit cell with unit cell parameters as shown in Table 2.1.

Table 2.1: Lattice constants for para-hexaphenyl [34]. β is the angle between the unit cell a- and c-vector, ϕ is the angle between the long molecular axis and unit cell bc-plane and θ is the angle between the short molecular axis and the unit cell ac-plane.

Molecule	a (Å)	b (Å)	c (Å)	β ($^\circ$)	ϕ ($^\circ$)	θ ($^\circ$)
Para-hexaphenyl	26.24	5.57	8.09	98.2	71	55

Due to the p6P molecule symmetry, the transient dipole for both absorption and emission is parallel to the long molecular axis, causing both the absorption and the emission to be highly polarized for a crystalline film. The crystalline film exhibit a broad absorption band at 350nm [35] and clear blue-light emission with distinguishable vibronic peaks, the (0-1) exciton transition being the strongest at 422nm.

2.1.2 Muscovite mica

Muscovite mica with formula $K_2Al_4(Si_6Al_2O_{20})(OH)_4$ is a sheet silicate substrate consisting of two tetrahedral (Si,Al) O_4 sheets ("T") with an octahedral AlO_6 sheet ("O") in between (see Figure 2.3b). The "T" and "O" sheets are bound together by Al^{3+} cations and OH^- oxanions, forming "TOT" layers, which are linked together by interlayer cations, such as Potassium (K^+). Cleaving takes place along the interlayer cations, revealing the (001) plane of muscovite mica, where the K^+ ions are randomly divided between the two new surfaces. The cleaving is almost perfect leaving large domains (cm^2) of atomically flat areas [36].

Muscovite mica is a dioctahedral mica, meaning that only two out of three octahedral AlO_6 sites are occupied by Al^{3+} cations which changes the binding to the tetrahedral sheet. Figure 2.3a depicts a muscovite mica surface (the (001) surface), where the tetrahedral are marked yellow, the octahedral light blue and the potassium cation dark blue. The missing Al^{3+} cation, cause the (Si,Al) O_4 tetrahedrals to tilt leaving atomic groves in the surface, thus changing the (001) plane symmetry from a threefold symmetry to an one-fold symmetry [37].

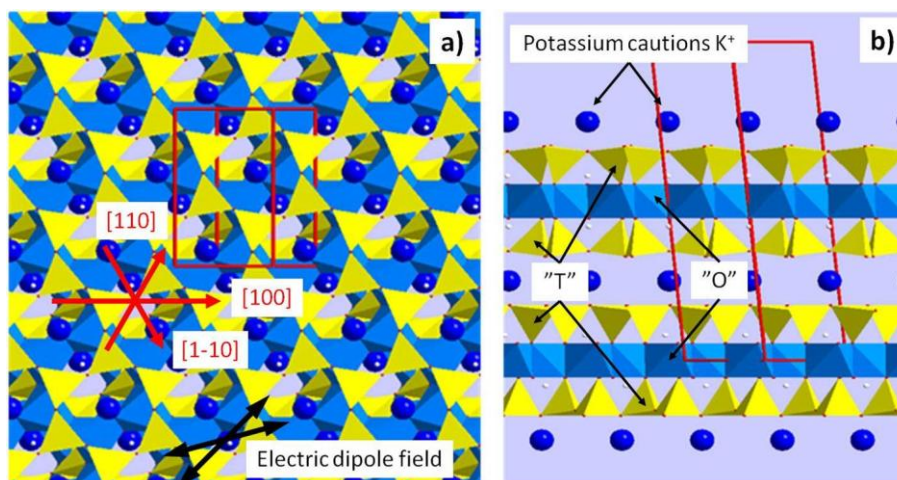


Figure 2.3: (a) A cleaved muscovite mica surface (001) plane. Groves in the surface occurs in one of the $\langle 110 \rangle$ directions in this case the $[1-10]$ direction. Electric dipole fields are believed to occur $90 \pm 15^\circ$ off the groove direction. (b) Muscovite mica consist of two tetrahedral $(\text{Si,Al})\text{O}_4$ sheets ("T") with a octahedral AlO_6 sheet ("O") in between. The "TOT" layers are divided by potassium cations (K^+) (edited and reprinted with permission of Frank Balzer).

Figure 2.3a shows the three high symmetry directions $[1-10]$, $[100]$ and $[110]$ of the (001) muscovite mica surface. The atomic grooves alternately follow one of the two $\langle 110 \rangle$ directions, i.e. the grooves follows the $[1-10]$ direction for odd numbers of muscovite mica layers and the $[110]$ direction for even numbers of muscovite mica layers, with an angle of 120° between the two directions. The grooves never follow the $[100]$ direction. To distinguish the grooved $\langle 110 \rangle$ direction from the non-grooved $\langle 110 \rangle$ direction, the two directions are often marked "g" and "ng", respectively. In addition to the grooves a freshly cleaved mica surface is positive charged due to the K^+ cations and is believed to have surface electric dipole fields pointing $90 \pm 15^\circ$ off the groove direction [38]. It is this fortunate combination of surface electric dipole field, surface groove and lattice size that makes muscovite mica interesting for molecular beam epitaxy of oligo-phenylenes.

2.1.3 Para-HexaPhenyl on muscovite mica

Deposition of p6P onto freshly cleaved muscovite mica at elevated temperatures leads to the formation of elongated and mutual parallel nanofibers e.g. the nanofiber sample shown in Figure 2.1 is grown at a muscovite mica surface temperature of 440K. For increasing temperatures the nanofibers increase mainly in length from a few micrometer to hundreds of micrometer, but also in width from 100nm to 800nm and in height from 20nm to 150nm until a critical temperature is reached. Above this critical temperature no nanofiber growth occurs [39]. The reason for this one-dimensional nanofiber growth is a combination of epitaxial and dipole assisted growth as pictured in Figure 2.4.

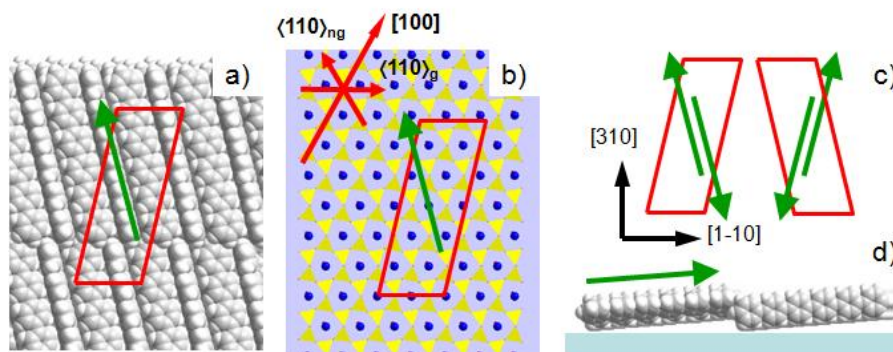


Figure 2.4: (a) The (1-1-1) face of bulk p6P together with the surface unit cell (red). The green arrow indicates long molecular axes. (b) The p6P unit cell (red) together with the mica (001) plane. The short p6P unit cell axes follow the mica surface groove direction $\langle 110 \rangle_g$ and the long molecule axes (green) align with the mica surface dipole moment. (c) Four possible directions of the p6P molecule layer. The green arrows indicate the long molecular axes. (d) The bulk molecules are tilted 5° with respect to the (1-1-1) face. The four molecule directions are therefore all unique (reprinted with permission from Frank Balzer).

Figure 2.4a shows the closed packed (1-1-1) face of bulk p6P, where the surface unit cell is depicted in red and the molecule direction is given by the green arrow. The different p6P layers are bound solely by Van der Waals forces, whereas the molecules in the herringbone structure within a layer are bound mainly by van der Waals forces, but also a weak C-H covalent bond of adjacent molecules occurs.

The epitaxy assisted growth is schematically shown in Figure 2.4b, where the p6P surface unit cell is depicted on top of the (001) muscovite mica surface. From an epitaxial point of view, the short p6P unit cell axis will align parallel to any of the three mica surface high symmetry directions, resulting in three p6P crystalline orientations separated by an angle of 60° . This is not the case looking at the p6P nanofibers on muscovite mica in Figure 2.1. The nanofibers are mutual parallel and only have one orientation, thus p6P molecules aligning only along one of the high symmetry orientations, namely the grooved $\langle 110 \rangle_g$ direction. This is opposite from nanofibers grown on phlogopite mica where no surface groves occur; here the nanofibers grow along all three symmetry directions [36].

In addition to epitaxy assisted growth, the long molecule axes of the evaporated p6P molecules align parallel to the mica surface electric dipole fields (see Figure 2.3a). Since the mica surface dipole has two orientations, namely $90^\circ \pm 15^\circ$ from the $\langle 110 \rangle_g$ direction, there are four different orientations of the p6P molecule. These four orientations, which occur by mirroring and 180° rotation of the p6P unit cell, are shown by green arrows in Figure 2.4c. Note that the p6P surface unit cell for all four molecule orientations fulfills the epitaxy assisted growth condition. The p6P molecules are tilted 5° with respect to the (1-1-1) plane (see Figure 2.4d), thus a 180° rotation of the p6P unit cell is not equivalent, but gives two unique molecular orientations.

Nanofiber growth on muscovite mica follows the Stranski-Krastnov growth mode [39], [42] which is divided into three different growth stages:

- **First stage:** A wetting layer of strongly bound lying p6P molecules is formed and completed after approximately 0.2nm p6P have been deposited. The wetting layer is believed to act as an intermediate layer, correcting for the small mismatch between the surface unit cell of mica and p6P.
- **Second stage:** 3-dimensional p6P crystallites are formed randomly distributed over the mica surface. Increasing mica surface temperature increases the crystallite size slightly. The formation of 3D crystallites is valid until approximately 0.5nm p6P have been deposited.
- **Third stage:** When a critical density of 3D crystallites is reached, the crystallites spontaneously rearrange into 1-dimensional chains of crystallites, i.e. nanofibers. In this stage nanofibers and crystallites coexist on the mica surface, where a crystallite denuded zone around the nanofiber emerges. Increasing the mica surface temperature results in more separated nucleation centers and longer nanofibers.

During growth the nanofibers strongly increase in length (up to several hundred μm) and less in width (up to 600nm) and height (up to 100nm). The anisotropic nature of the p6P molecule and the attachment of new crystallites results in the anisotropic nanofiber growth; p6P molecules tend to bind rather by π - π interactions along their long molecule axis, than via interactions between their C-H groups, leading to the elongated nanofiber structure.

2.2 Experimental setup

As mention in the beginning of this chapter, the nanofiber growth is highly dependent on the mica surface temperature. Nanofiber samples are typically of the order of $5 \times 5 \text{mm}^2$, which are applicable for growth studies. In the case of implementing nanofibers in devices, it is advantageous to grow large samples of homogeneous nanofibers. Large mica samples especially complicate heating of the mica, mainly due to the poor heat conductivity of mica.

This section describes the growth chamber vacuum system, together with the mica sample heating system.

2.2.1 Vacuum system

Nanofibers are grown under high vacuum (10^{-8} mbar) by Molecular Beam Epitaxy (MBE). The vacuum system (shown in Figure 2.5) consists of two chambers separated by a pneumatic valve, a transfer chamber and a growth chamber, each chamber having its own turbo pump.

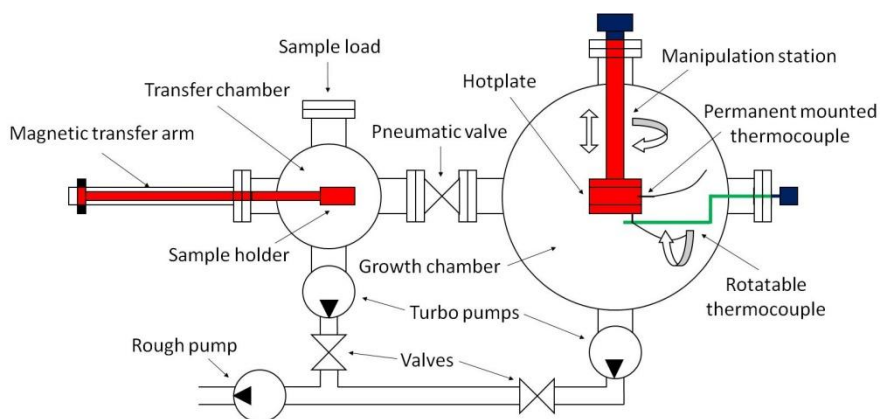


Figure 2.5: Schematic drawing of the vacuum system. The sample is loaded in the transfer chamber. After initial pumping it is moved to the growth chamber by the magnetic transfer arm. There are two temperature sensors mounted in the growth chamber, monitoring the hotplate temperature and the sample temperature, respectively.

The mica sample is loaded in the transfer chamber. After initial evacuation of the transfer chamber, the mica sample is transferred to the growth chamber by a magnetic transfer arm. In the growth chamber the sample holder is glided and clamped on top of a hotplate. Two type K thermocouples are mounted inside the growth chamber, a permanent mounted thermocouple monitoring the hotplate temperature and a rotatable thermocouple monitoring the mica sample surface temperature. The two metal alloys of the rotatable thermocouple is point welded and fixed to a rotatable arm in such a way that the point weld is pointing out with no metal connection to the rotatable arm. The hotplate position is adjustable in the vertical and rotational direction, enabling to adjust the mica sample compared to the rotatable thermocouple.

2.2.2 Heating system

The hotplate (Figure 2.6a) consists of two 1.5mm thick aluminum plates, where the front plate has a 0.7mm deep and wide groove for a coaxial heating cable (0.5mm in diameter). Two guider with springs are mounted at the front side of the front plate, in order to clamp the sample holder onto the hotplate. The purpose of the hotplate/sample holder arrangement is to obtain a homogeneous surface temperature of the hotplate and to ensure a sufficient heat transfer from the hotplate to the sample holder. The bi-metals of the permanent mounted thermocouple are point welded and fixed under a 2mm screw at the front side of the front plate.

The sample holder (Figure 2.6b) consists of a 1mm thick aluminum back plate and a 1.5mm thick stainless steel top frame with forty-eight 5x5mm windows, where the 25x75mm² muscovite mica is mounted in between. The purpose of the window arrangement in the front plate is to ensure thermal contact between the mica sheet and the back plate for the entire mica area. Fixing the mica only at the edge will lead to insufficient thermal contact in the middle of the sample, due to thermal expansion of the mica when heated, thus the mica needs to be fixed in the middle of the sample as well. This is done by the front plate window arrangement.

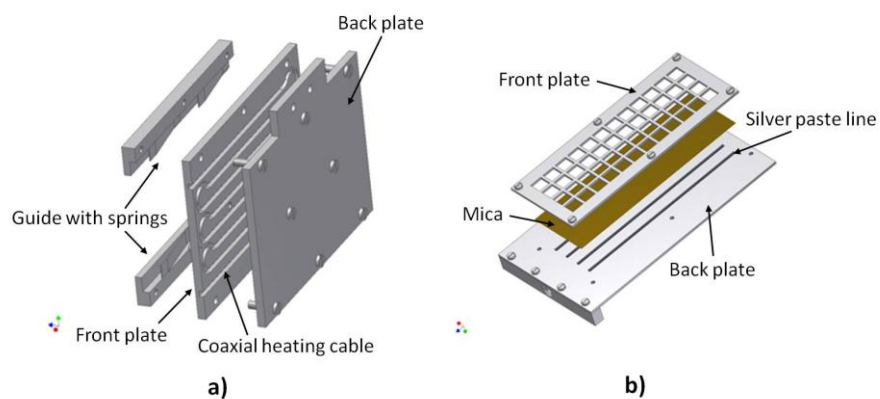


Figure 2.6: (a) The hotplate. Two 3mm thick aluminum plates fixed together by 8 bolts, where the front plate has a 0.8mm deep and wide groove for coaxial heating cable. Two guides with four springs, guides and press the sample holder on top of the hotplate. (b) Sample holder. The mica sheet is mounted in silver paste to ensure equivalent heat transfer and fixed with a 1.5mm stainless steel frame with forty-eight 5x5mm windows.

Since the growth process is done under high vacuum, convective heat transfer is neglected and only irradiant and conductive heat transfer exist. This complicates heating of the sample, since a small gap between mica and holder will reduce the heat transfer considerably (going from conductive to irradiant heat transfer). Together with the poor heat conductivity of mica, this will lead to a drop in the mica surface temperature. To overcome this problem, four lines of silver paste⁽¹⁾ (approximately 0.5mm wide) are placed on the back plate directly below the windows of the top frame. When mounting the top frame, the silver paste expands on the back side of the mica, ensuring good thermal contact between the back plate and the mica.

⁽¹⁾ SPI# 05062-AB Silver Paste Plus™.

Use of silver paste as adhesive layer is not without drawbacks. Even though the silver paste is made for vacuum use, heating the sample results in a rapid pressure increase inside the growth chamber from 4×10^{-9} mbar to 1×10^{-4} mbar, followed by a pressure decrease to 4×10^{-8} mbar within 45 minutes of heating. The silver paste consists of small silver pellets in solvent to keep it liquified. It is the evaporation of the solvent that causes the pressure increase. This evaporation of the solvent has the potential of contaminating the cleaved mica surface, but since no contamination effect on the grown nanofibers is detected⁽¹⁾ [40], contamination is deduced to be minimal.

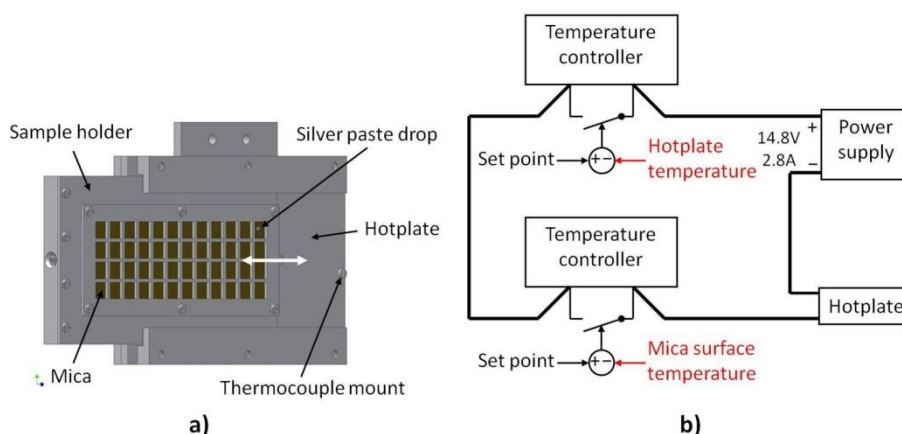


Figure 2.7: (a) Hotplate and sample holder arrangement. (b) Schematic drawing of the heating circuit for the hotplate.

The sample holder and hotplate arrangement are imaged in Figure 2.7a. Before loading the mica holder in the transfer chamber a drop of silver paste is placed on top of the mica in the upper right window of the top frame, with no thermal connection to the aluminum frame. The reason for this is to obtain good thermal connection between the rotatable thermocouple and the mica surface. Thus, after loading the sample, the rotatable thermocouple is placed in the silver paste drop, enabling to monitor the mica surface temperature.

Mica surface and hotplate temperature are monitored by two temperature controllers, which also on/off control the current applied to the coaxial heating cables in the hotplate (Figure 2.7b). The two temperature readouts provide a unique control of the mica surface temperature. The desired mica surface temperature is set on the mica surface temperature controller, followed by 2 hours of heating before evaporating p6P molecules. The desired mica surface temperature is actually reached after approximately 45 minutes, where the prolonged heating time is to ensure a stable and homogeneously mica surface temperature.

⁽¹⁾ Contamination usually shows as green nanofibers (contaminated nanofibers) or disordered nanofibers (contaminated mica surface).

2.2.3 p6P oven

The p6P oven is a custom-build Knudsen cell made from a 40mm long $\frac{1}{4}$ inch stainless steel tube with two end nuts mounted, one of these having a 0.5mm hole for the p6P molecules to escape. Coaxial heating cable is wrapped around the tube and everything is screened by a thin stainless steel box. A thermocouple is mounted at the oven monitoring the oven temperature.

Evaporation rate and the nominal p6P thickness are monitored by a water cooled Inficon XTC/2 quartz crystal microbalance mounted below the hotplate in the growth chamber. A shutter is mounted between the sample and the oven, screening the sample but not the microbalance from the molecular beam evaporated from the p6P oven, enabling to ensure a stable deposition rate before exposing the mica surface to the molecular beam.

2.2.4 Nanofiber growth procedure

To be able to compare different nanofiber samples, it is crucial to use the same nanofiber growth procedure each time, especially when examining nanofibers grown in a very narrow temperature window around the critical nanofiber growth temperature. Since the used growth method is valid for all the presented nanofiber samples, it will be outlined here.

- Four lines of silver paste are placed on the sample holder back plate directly below the windows in the top frame
- To avoid contamination from the backside, the muscovite mica sheet is cleaved on both sides by tape, leaving cm^2 areas of equivalent domain.
- The cleaved mica is placed on top of the silver paste and the top frame is mounted causing the silver paste to expand below the mica.
- A small silver paste drop is placed in the upper right window, followed by mounting the sample holder on the magnetic transfer arm in the transfer chamber.
- The transfer chamber is evacuated for 30 minutes before loading the sample holder in the growth chamber.
- The rotatable thermocouple is placed in the silver paste drop and the mica sample is heated for 2 hours to the desired sample temperature. Simultaneously the p6P oven is heated to 580K to avoid any out-gassed silver paste solvent sticking to the oven.
- The p6P oven temperature is raised to 650K where evaporation of p6P molecules begins. After stabilization of the deposition rate, the shutter is opened and nanofiber growth takes place.
- When the desired nominal nanofiber thickness is reached, the sample is either annealed or moved directly to the transfer chamber.

- The transfer chamber is vented with nitrogen and the nanofiber sample is removed.
- The backside of the mica is cleaved with tape to remove residual silver paste from the mica.

2.3 Experimental results

In the last decade, tremendous work has been done in characterizing organic para-hexaphenyl nanofiber growth on muscovite mica. This includes the influence of the mica surface temperature on the nanofiber morphology i.e. the nanofiber width, height, length and separation, the nominal nanofiber thickness dependence and the p6P cluster formation leading to nanofibers [39].

Mica surface temperature dependence studies have been performed going from room temperature up to the reported critical temperature of 480K where nanofiber formation no longer is energetic favorable. Longer and more separated nanofibers will occur, the higher the mica surface temperature is. This is due to increased crystallite dimensions for increased mica surface temperatures, leading to more separated nanofiber nucleation centers.

The aim of the work presented here is not a detailed investigation of the different nanofiber dependences, but to grow long and separated nanofibers homogeneously on a 25x75mm² mica substrate.

2.3.1 Homogeneity and critical temperature

The first interesting result is the critical temperature for nanofiber growth deduced here, while it differs from previous reports. Figure 2.8 shows four 2x2mm² images of nanofiber on the same mica sample. The four images depict nanofibers from four different positions (windows) on the 25x75mm² mica sample. The mica surface temperature during nanofiber growth was 453K, whereas the hotplate temperature was 469K and the deposition rate 0.045±0.015Å/s.

Even though the nanofiber sample does not appear homogeneous, please note that the images have size 2x2mm² and the densest nanofibers in Figure 2.8a are still separated by 20-40µm (see the 200x200µm² insert in Figure 2.8a). Thus, even the densest nanofiber areas comprise larger and more separated nanofibers, than a normal large nanofiber sample e.g. the nanofiber sample shown in Figure 2.1. Thus, first three images in Figure 2.8 depicts how very sensitive nanofiber growth is upon the mica surface temperature near the critical temperature for nanofiber growth. Other samples made at 455K and 458K show no nanofiber growth on mica surface, thus the temperature in these two cases is above the critical temperature for nanofiber growth. The critical temperature is therefore deduced to be 453K with a estimated uncertainty of ±2K. The estimated uncertainty is deduced from nanofiber samples grown at the same temperature readout, showing slightly deviating results. The critical temperature reported here (453K±2K) is different than the

critical temperature of 480K reported elsewhere [39]. A possible explanation for that is, that the mica temperature is normally measured by fixing a thermocouple in between two mica sheets. This method leads to a possible measurement error, since the mica surface temperature changes for different mica thickness as previously reported in [41].

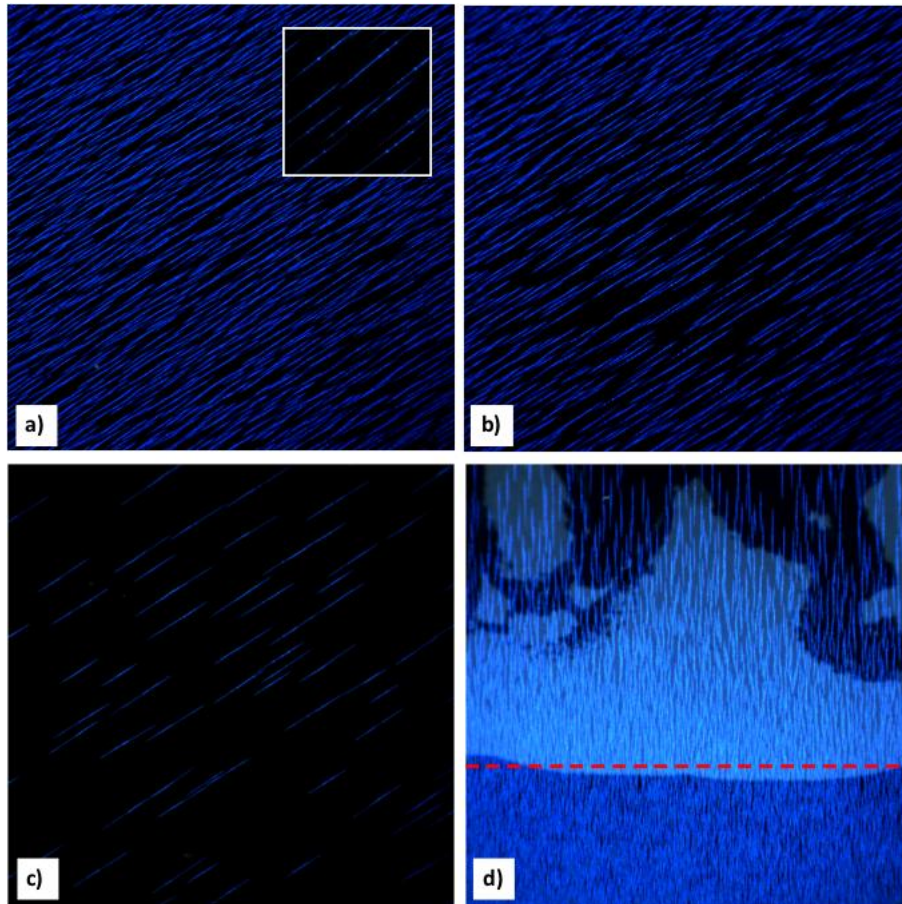


Figure 2.8: Four $2 \times 2 \text{ mm}^2$ fluorescence images from four different windows on the same $25 \times 75 \text{ mm}^2$ nanofiber sample grown at mica surface temperature 453K. The general changes in nanofiber density are depicted in (a), (b) and (c). The insert in (a) is a $200 \times 200 \mu\text{m}^2$ zoom of the nanofibers in (a). (d) Shows the difference in nanofiber density for good thermal contact (above the red line) and poor thermal contact (below the red line) to the sample holder.

Another critical aspect is the thermal connection between the sample holder and the hotplate. Without any thermal conductive layer below the mica, the mica surface temperature near the frame (good thermal connection) will deviate from the mica surface temperature in the middle of the window (poor thermal connection). This effect is depicted in Figure 2.8d where a $2 \times 2 \text{ mm}^2$ luminescence image of another nanofiber window of the same sample is shown. The light blue shadow is residual silver paste on the backside of the mica. Below the dashed red line no silver paste is present, thus the thermal connection to the mica is poor and

the nanofibers are dense. Above the dashed red line silver paste is present leading to good thermal connection and very separated individual nanofibers similar to the nanofibers shown in Figure 2.8c. The effect of a thermal layer below the mica has previously been reported in [41].

The absolute value of the critical nanofiber growth temperature is of interest from a basic research point of view, but not that interesting from a large scale production point of view. What is important on the other hand is the sample homogeneity, the sample size and the ability to reproduce the sample overall morphology for nanofibers grown at the critical temperature, i.e. grow long and very separated nanofibers. This has to a large extent been achieved here.

2.3.2 Wetting layer, crystallites and nanofiber clustering

An open question is how the very long and separated nanofibers in Figure 2.8 are created. The large nanofibers cannot originate solely from crystallites coming from the narrow denude crystallite area around the nanofibers. In [42] it is suggested that linear defects in the wetting layer acts as nucleation centers for the crystallite chain formation. This will result in several nucleation centers along the same linear defect, thus the nanofibers have a tendency to grow along the same line. As the nanofibers grow larger, they grow in to each other and form the long and separated nanofibers in Figure 2.8.

Figure 2.9a shows a $20 \times 90 \mu\text{m}^2$ fluorescence image from the same nanofiber sample as in Figure 2.8. The image could be interpreted as two nanofibers originating from two different nucleation centres growing into each other. A $6 \mu\text{m}$ long nanofiber parts is missing⁽¹⁾ in the middle of the image (outlined by the $8 \times 8 \mu\text{m}^2$ red square), revealing the surface below the removed nanofiber. Thus, revealing the underlying wetting layer if present. The bright blue spots in the image represent emitted light escaping from breaks in the nanofibers [31].

An $8 \times 8 \mu\text{m}^2$ AFM image of the area outlined by the red square in Figure 2.9a is depicted in Figure 2.9b, where the image height scale is 80nm. The underlying wetting layer of missing nanofiber part is not directly resolved in the AFM images, but revealed by the absence of p6P crystallites. The $2 \times 2 \mu\text{m}^2$ high contrast AFM image in Figure 2.9c depicts the underlying wetting layer, where the image height scale is 5nm. The crystallites around the missing nanofiber part are clearly visible, but no line defect in the wetting layer is detected. This either means that the wetting layer line defect is not present, the resolution of the AFM image is not good enough to image the line defect or no wetting layer is present. It at least opens the possibility for another explanation regarding the growth of large and separated nanofibers.

⁽¹⁾ The missing nanofiber parts have been removed by a condensing water technique which will be further discussed in Chapter 3

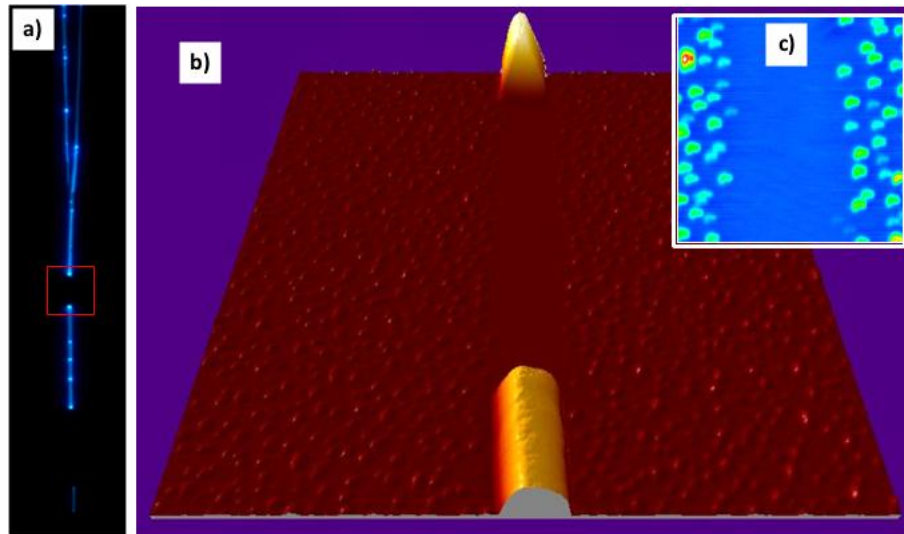


Figure 2.9: (a) A $20 \times 90 \mu\text{m}^2$ fluorescence image of an individual nanofiber. Two parts of the nanofiber are missing, one of them outlined by the red square. (b) A $8 \times 8 \mu\text{m}^2$ AFM image of the missing nanofiber part outlined by the red square in (a). The height scale is 80nm. (c) A $2 \times 2 \mu\text{m}^2$ high contrast AFM image of the wetting layer below the missing nanofiber part. The height scale is 5nm.

Figure 2.10 shows three different images of a nanofiber sample grown at 452K with deposition rate $0.085 \text{ \AA}/\text{s}$ and 4nm nominal thickness, thus this sample is grown at a slightly lower temperature (-1K) and a slightly higher deposition rate ($+0.04 \text{ \AA}/\text{s}$) than the sample depicted in Figure 2.8. In the $1 \times 1 \text{ mm}^2$ fluorescence image (Figure 2.10a), the four nanofibers marked with red arrows resemble large and separated nanofibers. Around the four nanofibers denude zone occurs. A zoom on one of these nanofibers is depicted in the $50 \times 50 \mu\text{m}^2$ fluorescence image in Figure 2.10b. The nanofiber does not appear to be a single nanofiber, but appears to be a cluster of individual large nanofibers. A $20 \times 20 \mu\text{m}^2$ high contrast AFM image of the nanofiber is shown in Figure 2.10c (height scale 60nm). The nanofiber is clearly not a single nanofiber, but three nanofibers lying close together. Around and in between the three nanofibers denude 3-D crystallite zones are present (similar to what previously have been reported in [42]). Beside that a denude 1-D crystallite chain zone appears approximately $4 \mu\text{m}$ on both sides of the three nanofibers. This denude 1-D crystallite chain zone has not previously been report and it opens for a hypothesis for the growth of large and separated nanofibers; large and separated nanofibers do not only originate from small 3-D crystallites from the denuded crystallite zone, but also from larger 1-D crystallite chains outside the denuded 3-D crystallite zone.

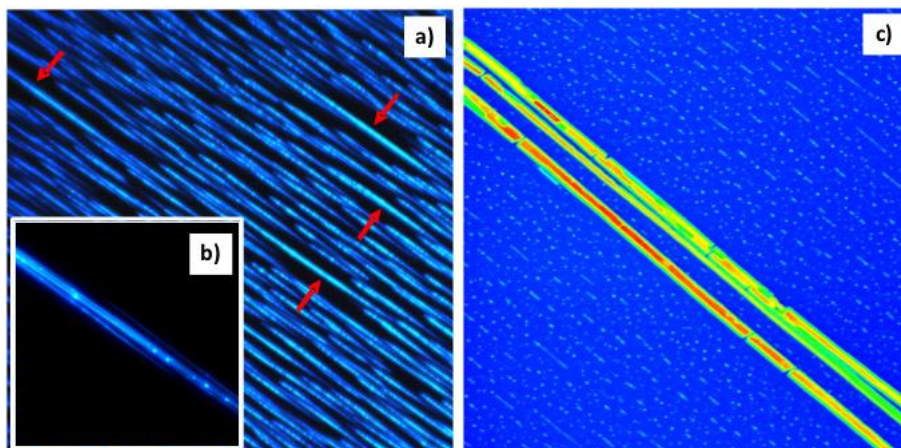


Figure 2.10: Nanofiber sample with 4nm nominal thickness grown at mica surface temperature 452K and deposition rate $0.085\pm 0.015\text{\AA}/\text{s}$. (a) A $1\times 1\text{mm}^2$ fluorescence image. Denuded nanofiber zones occur around the large nanofibers marked with red arrows. (b) A $50\times 50\mu\text{m}^2$ zoom of one of the nanofibers marked with red arrows. The nanofiber is not a single chain, but seems to originate from multiple nanofibers clustering together. (c) A $20\times 20\mu\text{m}^2$ (height scale 60nm) high contrast AFM image of one of large nanofibers.

This also opens for a possible explanation for inhomogeneities within the nanofiber, i.e. kinks and multiple fiber structure. If the large nanofiber in addition to crystallite also originates from larger crystallite chains, the unit cell of the crystallite chain might not match the unit cell of the existing fiber, remembering the four possible molecular orientations within the p6P unit cell. This gives rise to a new crystallite nucleation center close to the existing nanofiber.

2.3.3 Annealing and breaks

Previous annealing studies have shown that 3-D crystallites surrounding an existing nanofiber are incorporated into the nanofiber, when keeping the nanofiber sample at its growth temperature for e.g. one hour after nanofiber growth [42]. Instead of keeping the nanofiber sample at its growth temperature and then removing it from the growth chamber, it might be more appropriate to slowly cool down the nanofiber sample, giving the p6P molecules time to relax to the energetic preferable crystal structure.

The nanofiber sample represented in the $2\times 2\text{mm}^2$ fluorescence image in Figure 2.11a is grown at $454\text{K}\pm 2\text{K}$ with deposition rate $0.055\pm 0.015\text{\AA}/\text{s}$ and nominal thickness 5nm. The widely distant single nanofibers are comparable to the nanofibers in Figure 2.8 grown under similar conditions. The major difference between the two nanofiber samples being, that the nanofiber sample in Figure 2.11a has been annealed from its growth temperature $454\text{K}\pm 2\text{K}$ to room temperature by $1^\circ\text{C}/\text{min}$ before it was removed from the vacuum chamber. The bright spots marked with white arrows in the $200\times 200\mu\text{m}^2$ insert represent emitted

light escaping from breaks in the nanofiber, thus the nanofiber breaks are not avoided by annealing the nanofiber sample.

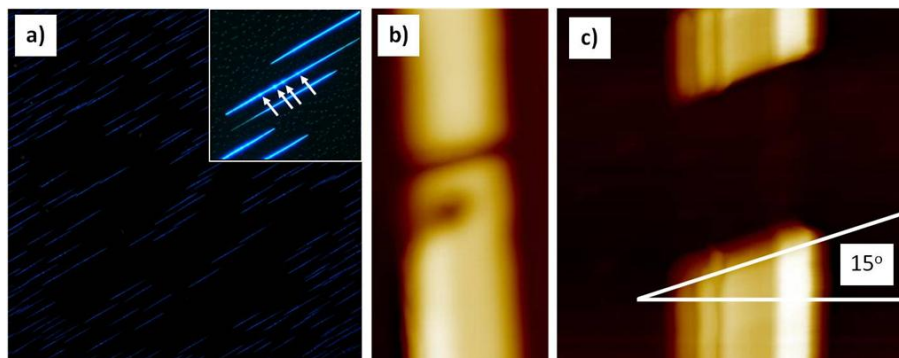


Figure 2.11: (a) A $2 \times 2 \text{ mm}^2$ fluorescence image of a nanofiber sample annealed from its growth temperature (454K) to room temperature by $1^\circ\text{C}/\text{min}$. Nominal thickness 5nm and deposition rate $0.055 \pm 0.015 \text{ \AA}/\text{s}$. The insert shows a $200 \times 200 \mu\text{m}^2$ zoom of the sample, where the bright spots (marked with white arrows) represents breaks in the nanofiber. (b) A $1 \times 2 \mu\text{m}^2$ AFM image of a nanofiber break in one of the single nanofibers in Figure 2.8c. The nanofiber width and height is 730nm and 66nm respectively. The break distance is 200nm. (c) A $2 \times 2 \mu\text{m}^2$ AFM image of one of the single nanofibers in a). The nanofiber width and height is 940nm and 115nm, respectively and the break gap is $1 \mu\text{m}$.

Figure 2.11b depicts a $1 \times 2 \mu\text{m}^2$ AFM image of a typical single nanofiber break from the non annealed nanofiber sample (Figure 2.8c). The nanofiber width and height being 730nm and 66nm respectively and the break distance is 200nm. This picture changes (at least for some of the breaks) for the annealed nanofiber sample. Figure 2.11c shows a $2 \times 2 \mu\text{m}^2$ AFM image of the annealed nanofiber sample in Figure 2.11a, the imaged nanofiber being 115nm high and 940nm wide. The break distance in this nanofiber is $1 \mu\text{m}$, thus a factor 5 larger than the break distance found for the non annealed nanofiber sample where no large break distances are found. A possible explanation of this is the difference in thermal expansion coefficient for the muscovite mica substrate ($10 \mu\text{m} \cdot \text{m}^{-1} \cdot \text{K}^{-1}$ [43]) and the aluminum sample holder ($23 \mu\text{m} \cdot \text{m}^{-1} \cdot \text{K}^{-1}$ [44]). Since the mica is fixed to the aluminum sample holder, the lower thermal expansion coefficient of mica will cause the mica to be stretched during heating and squeezed during cooling, resulting in deformation of the mica after ended nanofiber growth. The hypothesis is that annealing gives the p6P molecules more time to relax resulting in fewer but larger breaks.

Another interesting aspect in Figure 2.11b and c) is that in both cases the nanofiber is broken at an angle 75° to the nanofiber direction, thus the cut direction exactly matches the predicted p6P molecular orientation within the nanofiber. Since the p6P molecule direction appears to be similar on each side of the break, this also indicates that these breaks are originating from stress in the muscovite mica substrate and not from the nanofiber growth process.

2.4 Summary and outlook

Growth of large nanofiber mica samples ($25 \times 75 \text{ mm}^2$) with homogeneous nanofibers morphology was achieved. The on surface temperature measurement technique provides an accurate control over the mica surface temperature, which (together with homogeneous thermal connection between mica and sample holder) is necessary to control the very temperature dependent nanofiber morphology. The critical temperature regarding nanofiber growth was found to be 353K with an estimated uncertainty of $\pm 2\text{K}$.

Nanofibers grow via spontaneous re-arrangement of 3D crystallites forming a crystallite chain followed by 3-D crystallites adding to the already existing crystallite chain, thereby forming nanofibers with a denuded crystallite zone surrounding them [39], [42]. Regarding large and separated nanofibers grown at the critical temperature a not previous reported crystallite chain denuded zone also appears around the nanofibers, indicating that crystallite chains also adds to already existing nanofibers. This effect might explain the kinks and multi nanofiber morphology of these large nanofibers. In addition to that annealing experiments indicate that at least some of the nanofiber breaks originate from stress introduced in the mica substrate when heating and cooling the mica substrate.

Future improvement of the nanofiber growth process can be done by avoiding any clamping of the mica substrate, thus heating of the mica substrate should be done solely by radiant heating. This has several advantages compared to the technique described above:

- The thermal conducting layer below the mica can be avoided, thereby minimizing the risk of contamination.
- Heating of the mica should be faster since no metal parts but only the mica needs to be heated. This is important regarding mass production.
- No stress from clamping is introduced in the mica.
- Cleaving of the mica can be done in either an inert atmosphere or in vacuum.

An exact temperature control of the mica surface temperature is crucial in controlling the very temperature sensitive nanofiber morphology. Instead of measuring the mica surface temperature by means of thermocouple that needs good thermal connection to the mica, it would be superior to measure the mica surface temperature by means of an infrared temperature sensor that do not need any thermal connection to the mica surface.

Together with a better control of the deposition rate, these improvements are necessary for a more intensive investigation of the nanofiber growth mechanism at the critical nanofiber growth temperature, but also necessary in up-scaling the production of organic p6P nanofibers.

3 Transfer and Integration of p6P Nanofibers

In the past decade there has been a tremendous progress in implementing inorganic one-dimensional nanostructures as the active part in electrical components, such as OFETs, sensors and flexible displays. These nanostructures are typically grown via different “bottom-up” techniques, resulting in single or quasi-single crystalline material. Several techniques have been demonstrated for transfer of inorganic nanostructures, such as Ge, Si and InAs nanowires. These techniques include stamping [45], printing [46] and molding [47]. Fewer attempts have apparently been made on transferring organic one-dimensional nanostructures from their growth substrate. I have not been able to find any reference literature describing transfer of organic one-dimensional structures, such as nanofibers. Most transferring techniques involves printing of organic thin films [48],[49] and not transfer of organic nanofibers. The reason for this is probably that the main organic research lies in the field of organic thin films in various devices, but also the complexness in transferring organic nanofibers versus inorganic nanowires might play an important role. Due to their weak Van der Waals bonding, organic nanofibers are more fragile compared to inorganic nanowires, thus increasing the risk for damaging the organic nanofibers during the transfer process.

To transfer nanostructures without alternating either the nanostructure or the desired receiver substrate, must be the key point in transferring any nanostructure from the growth substrate. Especially regarding basic research it is important that the physical properties of the nanostructures are not altered by the transfer technique. For that reason, adhesive layers on the receiver substrate are avoided, and only DI-water is used for the presented transferring process.

3.1 Introduction to nanofiber stamping

It has previously been reported that p6P nanofibers can be removed from their growth substrate muscovite mica by placing a drop of water on top of the mica, followed by drop-casting of the nanofiber/water solution [50].. There are however several drawbacks of this technique. Due to the weak Van der Waals bonds, the nanofibers are breaking up in smaller pieces when, and more importantly the desired mutual parallel orientation of the nanofibers on the growth substrate is not preserved. Integration of nanofibers in devices is also possible by the drop-casting the water/nanofiber solution on a device platform and afterwards choosing one nicely placed nanofiber and build up the device around this particular nanofiber [51]. This solution however does not bare the possibility for large scale production. In order to implement nanofibers in large scale devices and benefit from their

unique properties, it is crucial for most applications to preserve the parallel nanofiber orientation.

A first attempt in preserving the nanofiber orientation after transfer was to place a water drop on a receiver substrate and then gently press the receiver substrate against a nanofiber mica sample. For this, the receiver substrate in Figure 3.1a was fabricated as a test stamp. The test substrate is a $5 \times 5 \text{ mm}^2$ silicon wafer with nine $1 \mu\text{m}$ high and $200 \times 200 \mu\text{m}^2$ elevated square platforms. The nine platforms are defined by photolithography⁽¹⁾ and etched out by Inductive Coupled Plasma Reactive Ion Etching (ICPRIE).

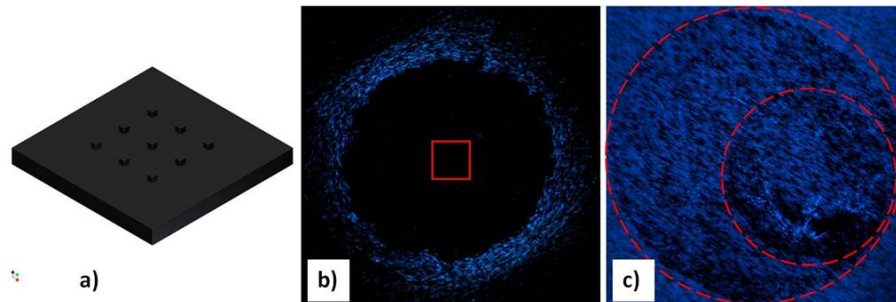


Figure 3.1: (a) Nanofiber transfer test substrate. A $5 \times 5 \text{ mm}^2$ and $500 \mu\text{m}$ thick Si substrate with nine $200 \times 200 \mu\text{m}^2$ elevated squares. The height of the nine elevated squares is $1 \mu\text{m}$ and they are separated by 1 mm . (b) $1.6 \times 1.6 \text{ mm}^2$ fluorescent image of nanofibers transferred to the test substrate by DI-water drop and stamping. The red square outlines the middle $200 \times 200 \mu\text{m}^2$ elevated platform. (c) A $2 \times 2 \text{ mm}^2$ fluorescent image of two dried out water drops (outlined with red circles) on a nanofiber muscovite mica sample.

A small drop of DI-water was placed on the middle platform and the test substrate was gently pressed against the nanofiber mica sample. The idea is that the water should release the nanofibers and nanofibers should stick to the flat silicon platform keeping their original orientation. The result is shown in the $1.6 \times 1.6 \text{ mm}^2$ fluorescent image in Figure 3.1b. The red square outlines the $200 \times 200 \mu\text{m}^2$ platform, and as it is seen no nanofibers are lying on this. In a circle around the platform, on the other hand, nanofibers are lying with random orientation. The reason for this can be deduced from the $2 \times 2 \text{ mm}^2$ fluorescent image in Figure 3.1c. Here a drop of DI-water (outlined by the large dotted red circle) is placed on a nanofiber mica sample and left to dry out. As seen, the nanofibers are mainly released at the edge of the water drop and not in the middle of the water drop. Observing the water drop under a UV-microscope as it dries out, it is seen that the nanofibers are actually only released at the edge of the water drop. The nanofibers released inside the large dotted red circle in Figure 3.1c are released as the water drop is drying out, thereby moving with the water front inwards. It is also observed, that the released nanofibers are floating on top of the water drop. This indicates (but not excluding that other forces can be involved) that the nanofibers are

⁽¹⁾ Recipe for making the transfer test substrate is given in Appendix B

released from the mica substrate mainly by capillary forces of the water droplet, neutralizing the forces binding the nanofiber to the mica surface. When released, the capillary forces of the water droplet moves the nanofiber to the surface of the water droplet. This explains the transferred fibers in Figure 3.1b lying around the elevated platform. Since the water drop is larger than the $200 \times 200 \mu\text{m}^2$ platform, no capillary force is releasing the nanofibers at the platform position, but only around the platform.

From experience it is noticed, that it is getting harder to release the nanofibers from the mica substrate over time (several months). This is at least valid for nanofiber mica samples stored in ambient air, where water from the air is absorbed on the mica surface [52], [53]. This fosters the idea, that it might be water from the air absorbed on the mica sample, which made the nanofibers stick more to the mica surface over time. The consequence of this could be that nanofibers would not be released from a mica sample, which already had been exposed to water once. The smaller dashed red circle in Figure 3.1c outlines a second water drop, placed inside the area of the dried out larger water drop. As seen, the nanofibers are also released by the second water drop, thus it is possible to transfer nanofibers from a nanofiber mica sample that already has been exposed to water. This is good news regarding stamping of nanofibers, since the stamping will take place in an atmosphere with high humidity. The fact that nanofibers stick more to the mica over time, might be due to other processes than water absorbed on the mica surface, such as other chemical reactions of the wetting layer.

Another problem is that even if the transfer substrate and the nanofiber mica sample is pressed against each other at the edge of the water drop, the nanofibers will be transferred but not keep their mutual orientation, due to the water fluid movement when the two substrates are pressed against each other. As a consequence a nanofiber stamping machine had to be designed, where the droplet size is minimized.

3.2 Nanofiber stamping machine

Instead of placing a small water drop on the nanofiber receiver substrate, the idea is to let water condense on the receiver substrate from a controlled atmosphere [54], thereby minimizing the water droplet size. At the same time it would be preferable to be able to orient the nanofibers on the receiver substrate in any desired direction. The nanofiber stamping machine in Figure 3.2 fulfills these demands.

All the components of the nanofiber stamping machine are made of aluminum, to ensure high heat conduction, and the box dimension⁽¹⁾ is approximately $180 \times 100 \times 100 \text{mm}^3$. The purpose of the nanofiber stamping machine is to keep the

⁽¹⁾ Mechanical drawings shown in Appendix B

nanofiber mica sample in a controlled atmosphere of defined air temperature and humidity. A receiver substrate kept at a lower temperature is inserted in this atmosphere, resulting in small water droplets condensing at the receiver substrate surface. The receiver substrate is then gently pressed towards the nanofiber mica sample, thus transferring nanofibers from the nanofiber sample to the receiver substrate.

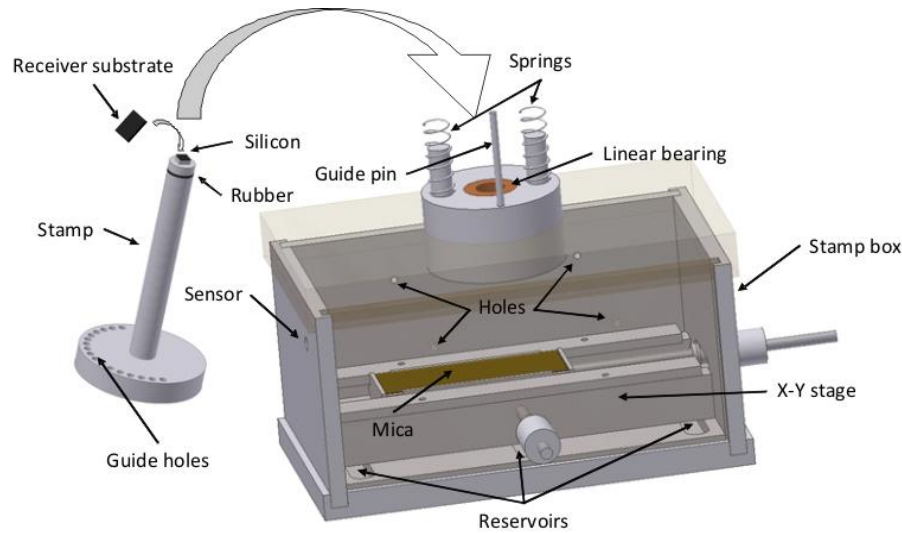


Figure 3.2: Nanofiber stamping machine. The stamp box (without the stamp) is heated, causing DI-water in the reservoirs to evaporate, thereby increasing the temperature and the relative humidity inside the box. The stamp, which is kept at a lower temperature (21°C), is inserted in the stamp box, causing small water droplets to condense at the receiver substrate. When the stamp is pressed against the nanofiber mica sample, nanofibers are transferred to the receiver substrate.

In the bottom plate the three reservoirs are each filled with 2ml of de-ionized (DI) water. The $25 \times 75 \text{mm}^2$ nanofiber mica sample is placed on a $25 \times 75 \text{mm}^2$ silicon wafer support, to ensure that the atomically flat mica is lying on a flat surface. The mica sheet is not clamped to the silicon support, but only fixed by a water film between the silicon support and the backside of the nanofiber mica sample. The nanofiber sample plus silicon support is placed on the x-y stage, thus enabling one to stamp from any desired area of the nanofiber sample. A linear bearing is mounted in the top plate for guiding the stamp rod, and two springs are mounted to retract the stamp after stamping. The stamp box is placed on a hotplate, heating up the entire box and thereby increasing the air temperature inside the box. The increased temperature causes the DI-water in the three reservoirs to evaporate, thereby increasing the relative humidity inside the box also. The two side plates each have two 3mm holes, stabilizing the relative humidity at $73 \pm 5\%$ for any given temperature inside the box. A handheld temperature and humidity sensor is mounted through the hole in the left side of the stamp box, enabling one to monitor the temperature and humidity inside the stamp box.

The rod of the stamp part (shown to the left in Figure 3.2) fits the linear bearing at the top of the stamp box. The stamp is designed for transferring nanofibers onto a $5 \times 5 \text{ mm}^2$ receiver substrate. A cylindrical disk with seventeen 3mm guide holes at the edge of the disk is mounted at the top of the stamp rod. The seventeen holes have mutual distances of 11.25° and fit the guide pin mounted in the stamp box top plate. This enables to rotate the stamp 180° in steps of 11.25° compared to the nanofiber mica sample. Between the stamp rod and the stamp head a 1mm thick soft rubber material is inserted to minimize the force applied to the stamp head. A $5 \times 5 \text{ mm}^2$ Si wafer piece is glued at the end of the aluminum stamp head in order to flatten the stamp head surface, enabling one to mount a $5 \times 5 \text{ mm}^2$ silicon receiver substrate only by a water film between the stamp head and the receiver substrate, making it easy to mount and dismount the receiver substrate.

The general stamping procedure is as follows:

1. All of the forty-eight $5 \times 5 \text{ mm}^2$ windows of the nanofiber mica sample are examined in an UV-microscope, mainly regarding the nanofiber orientation, but also regarding density, length and domain shifts of the nanofibers. These nanofiber properties are noted before stamping.
2. The nanofiber mica sample is placed on the x-y stage inside the stamp box and the mica sample is aligned so the stamp hits the lower left nanofiber window. This is the start coordinate and the x-y stage can now be moved to stamp from any desired nanofiber window, without opening the stamp box.
3. The three reservoirs are each filled with 2ml DI-water and the stamp box is closed and placed on a pre-heated hotplate for 30min to stabilize the atmosphere inside the stamp box.
4. The stamp with the mounted receiver substrate is oriented in the desired direction compared to the nanofiber orientation and inserted in the defined atmosphere inside the stamp box. Within a time frame of five seconds, the receiver substrate is manually pressed against the nanofiber mica sample applying as little force as possible.
5. The stamp is retracted by the springs and manually removed from the stamp box.

A nanofiber mica sample with nine transferred nanofiber areas is shown in Figure 3.3a and the corresponding stamped nanofibers on the nine elevated silicon squares are shown in Figure 3.3b. Since the nanofibers are stamped, the stamping direction corresponds to fold the two images around the vertical axis between the two images. Figure 3.3 clearly shows that it is possible to define transferred nanofiber areas with the condensing water technique.

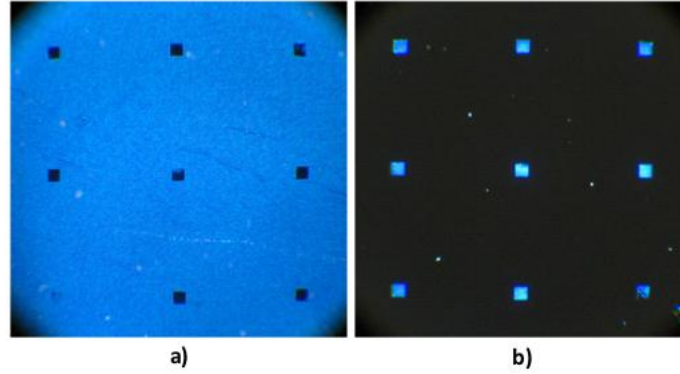


Figure 3.3: Two 2.7x2.7mm² fluorescent images. (a) Nanofiber mica sample with nine transferred areas. (b) Nine 200x200µm² elevated Si squares with nanofibers stamped from the sample in a).

3.3 Experimental results

The stamping procedure is to keep the stamp temperature below the dew point temperature of the defined atmosphere in the stamp box. In this case the temperature of the stamp is kept at 22°C, thus the dew point temperature inside the stamp box should be 22°C or above. A rough estimation of the air temperature inside the stamp box is given by [55]:

Equation 3.1

$$T_{dew\ point} \approx T_{box} - \frac{100 - RH}{5}$$

↓

$$T_{box} \geq T_{stamp} + \frac{100 - RH}{5} = 22^\circ\text{C} + \frac{100\% - 73\%}{5} = \underline{27.4^\circ\text{C}}$$

where T_{box} and T_{stamp} are the temperature inside the stamp box and the stamp itself, respectively, and RH is the relative humidity inside the box. Thus, the stamp box temperature should according to this be 27.4°C or above, for water to condense on the stamp substrate.

3.3.1 Temperature and humidity dependence

The first issue to be tested is how well the nanofibers are transferred at different temperatures inside the stamp box. For this experiment nanofibers are stamped on the test substrate (Figure 3.1a) for four different temperatures inside the stamp box, namely 23°C, 28°C, 33°C and 38°C. In all four cases the relative humidity is 73±5%. The result of this experiment is shown in Figure 3.4, where (a) to (d) shows 200x200µm² areas of missing nanofibers on the original mica sample and (e) to (h)

shows the correspondent transferred nanofibers on one of the elevated platforms of the stamp test substrate i.e. the eight images represent four individual nanofiber transfers made at different temperature and humidity. Since the nanofibers are stamped, the stamping direction corresponds to fold the upper four images with the lower four images around the horizontal axis between the upper and lower images.

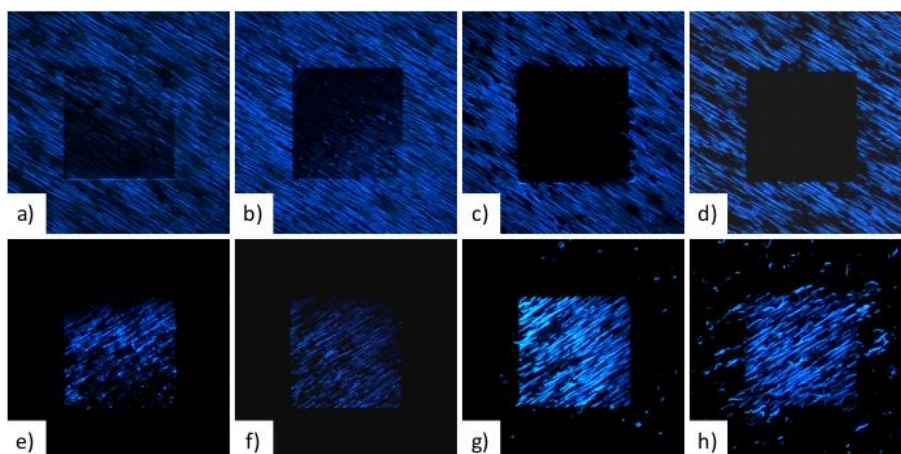


Figure 3.4: Eight $400 \times 400 \mu\text{m}^2$ fluorescent images. (a), (b), (c) and (d) shows transferred nanofiber areas from a nanofiber mica sample with stamp box air temperatures of 23°C , 28°C , 33°C and 38°C respectively. (e), (f), (g) and (h) shows the stamp fibers on $200 \times 200 \mu\text{m}^2$ Si squares corresponding to (a), (b), (c) and (d) respectively. For all four transfers the relative humidity was $73 \pm 5\%$.

Inspection of Figure 3.4a plus (e) and Figure 3.4b plus (f) reveals that for transfers made at stamp box temperatures below (23°C) and near (28°C) the temperature given in Equation 3.1, only part of the nanofiber material is removed from the mica surface. The nanofibers are not transferred as a whole; it more looks like the nanofibers are ripped apart. In Figure 3.4c plus (g) and Figure 3.4d plus (h) all of the nanofibers are transferred from the mica to the receiver substrate, thus the optimum transfer temperature lies between 28°C and 38°C . Both in Figure 3.4g and mainly Figure 3.4h it is seen that nanofiber material is present outside the elevated platform area. Since the nanofibers need water to be released from the mica surface, this means that the heights of the condensed water droplets on the receiver substrate are larger than the heights of the elevated platforms, i.e. the condensed water droplets have a height of more than $1 \mu\text{m}$ for temperatures above 33°C inside the stamp box.

A closer look at the nanofibers transferred at 33°C and 38°C (Figure 3.4g and h) is shown in Figure 3.5a and (b), respectively. The nanofibers in Figure 3.5b, which are transferred at 38°C , are clearly more misaligned than the nanofibers in Figure 3.5a, which are transferred at 33°C . Inspecting the round shape of the misaligned nanofiber areas in Figure 3.5b, it is evident that the misalignment originates from the water droplet shape, i.e. the condensed water droplets on the receiver

substrate are too large. The optimum stamp box temperature is a compromise between enough water to release the nanofibers and too large water droplets causing disorder of the nanofibers. Several other stamping experiments were performed and the optimum temperature inside the stamp box was found to be 31°C. Figure 3.5c shows nanofibers from a different nanofiber mica sample transferred at this temperature.

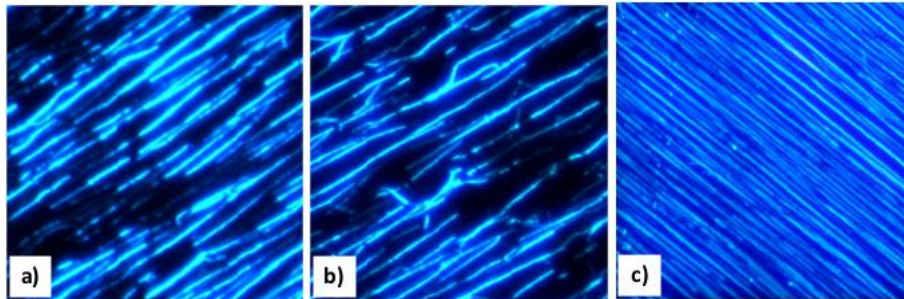


Figure 3.5: Three $100 \times 100 \mu\text{m}^2$ fluorescence images of transferred nanofibers on the receiver substrate shown in Figure 3.1a. (a) A zoom of Figure 3.4g of nanofibers stamped at 33°C. (b) A zoom of Figure 3.4h showing nanofibers stamped at 38°C. (c) Nanofibers stamped from a different nanofiber mica sample at 31°C inside the stamp box.

Keeping the temperature inside the stamp box at 31°C, i.e. 4.6°C above the theoretical critical temperature in Equation 3.1, is no guarantee for transferring the nanofibers as nicely as in Figure 3.5c. Many other issues are critical regarding a nice transfer e.g. the mica substrate and the receiver substrate has to contact equally on all of the transfer area. This is in fact the main reason for making receiver substrates with reduced contact area as the test substrate in Figure 3.1a. If one tries to transfer to a flat $5 \times 5 \text{mm}^2$ surface, there will only be transferred nanofibers around the edge of the substrate. Any dirt on the contact area or a cleaving step in the nanofiber mica sample will also result in incomplete nanofiber transfer.

A closer look at the transferred area on the nanofiber mica sample is given in Figure 3.6. The $160 \times 100 \mu\text{m}^2$ fluorescence image in Figure 3.6a is a zoom of the upper left transfer area of Figure 3.4c, i.e. the original mica sample with nanofibers transferred at $33 \pm 0.5^\circ\text{C}$ and $73 \pm 5\% \text{RH}$. The $20 \times 20 \mu\text{m}^2$ white square marked “1” corresponds to the *Atomic Force Microscope* (AFM) image in Figure 3.6b. As seen from the AFM image, the transferred nanofiber area is very well defined and all the nanofibers inside the area are transferred. Some of the nanofibers in the AFM image do not appear in the fluorescence image (Figure 3.6a) e.g. the three nanofibers marked with a white dashed circle, even though their height is 30-50nm and they should be visible in a UV-microscope image. This effect is most likely due to contamination during the nanofiber growth, but it might also evolve from water absorbed on the surface during the transfer process.

The $20 \times 12.5 \mu\text{m}^2$ AFM image in Figure 3.6c shows the same transferred area as Figure 3.6b, but at higher resolution. Here, the p6P clusters in between the individual nanofibers are clearly visible. The clusters, that have heights around 5nm, are like the nanofibers removed or at least released from the mica substrate inside the transferred area. The piece of material indicated by the white arrow in Figure 3.6b might be the p6P clusters sticking together after release from the mica, ending up at the mica surface again after the water evaporates. At the fluorescence image in Figure 3.6a a small blue spot is visible in the position of the material piece in Figure 3.6b. This supports the assumption that the piece of material is actually p6P cluster sticking together.

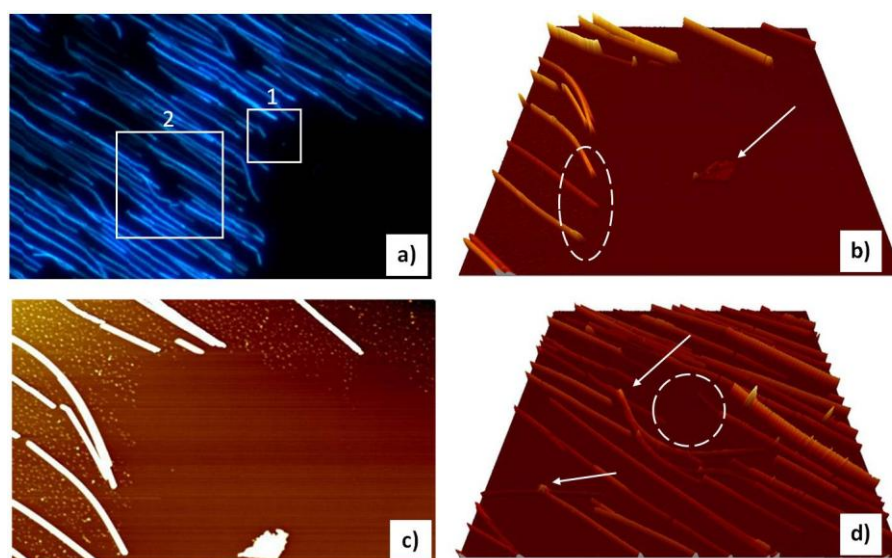


Figure 3.6: (a) A $160 \times 100 \mu\text{m}^2$ fluorescence image of the upper left transferred nanofiber area in Figure 3.4c. (b) A $20 \times 20 \mu\text{m}^2$ atomic force microscope (AFM) image of the area outlined by square 1 in a). The nanofiber heights are between 30-90nm. (c) A $20 \times 12.5 \mu\text{m}^2$ cut of image b), but at higher resolution. (d) A $40 \times 40 \mu\text{m}^2$ AFM image of the area outlined by square 2 in a). The nanofiber heights are between 30-90nm.

The last image (Figure 3.6d) is a $40 \times 40 \mu\text{m}^2$ AFM image of area “2” in Figure 3.6a, which is outside the receiver substrate contact area. It shows nanofibers released and pushed to the side (indicated by the white dashed circle). The reason for this is that the condensed DI-water droplets on the receiver substrate are larger than the $1 \mu\text{m}$ high elevated platform, i.e. the water droplets are in contact with the nanofiber mica sample even though the receiver substrate is not in contact with the nanofiber mica sample in this area. Thus, the nanofibers are released and moved to the border of the water droplet, in agreement with the hypothesis that the nanofibers are released from the mica by capillary forces of the water droplet. Figure 3.6d also shows how critical the transfer process is. The nanofibers have to be in contact with the receiver substrate immediately after they are released by the water droplets, otherwise the nanofibers will start moving, causing disordered

transfer. The two white arrows in Figure 3.6d mark nanofibers lying on top of each other. These nanofibers have been moved by the water droplet without breaking. Thus, despite the weak Van der Waals bonding the nanofibers can be moved and bent without breaking up into smaller pieces.

3.3.2 Distortion of transferred nanofibers

The next to investigate is the distortion of the nanofibers due to the transfer process. Even though the force applied to the stamp during the transfer is minimized, the hard mica and receiver surface will cause some distortion of the soft organic nanofiber. Note that the force is manually applied to the stamp and therefore hard to control. To investigate the distortion of the nanofibers, large and separated nanofibers are stamped from their growth substrate muscovite mica onto a $1074 \times 875 \mu\text{m}^2$ square platform defined by photolithography. The large separation of the nanofibers makes it easier to detect and investigate one individual nanofiber, both with fluorescence microscope and with atomic force microscope.

Two $1.2 \times 1 \text{mm}^2$ fluorescence microscope images are shown in Figure 3.7a and (b), where Figure 3.7a shows nanofibers stamped onto the $1074 \times 875 \mu\text{m}^2$ elevated square (outlined with a white square) and Figure 3.7b shows the corresponding sample with removed nanofibers (outlined with a white square). The stamp is rotated 33.75° from its zero position in order to orient the transferred nanofibers perpendicular to the receiver substrate edge. The stamping direction corresponds to fold the two images around the vertical axis between the them. The transfer is done at $31 \pm 0.5^\circ\text{C}$ and $73\% \pm 5\text{RH}$ inside the stamp box. As seen, the nanofibers are long and separated and all of the nanofibers inside the contact area are removed from the nanofiber mica sample and transferred to the receiver substrate. A $10 \times 6 \mu\text{m}^2$ high resolution atomic force microscope image of the nanofiber marked with the white circle in Figure 3.7b is shown in Figure 3.7d. The nanofiber is 90nm high and 600nm wide. The p6P cluster formation is clearly visible around the nanofiber. At the area where the nanofiber has been transferred, clusters are missing.

A $10 \times 10 \mu\text{m}^2$ AFM image of the corresponding transferred nanofiber part on the $1 \mu\text{m}$ high elevated receiver substrate, marked with the white circle in Figure 3.7a, is shown in Figure 3.7c. The transferred nanofiber is 45nm high and $1.1 \mu\text{m}$ wide, thus approximately half the height and twice the width of the original nanofiber in Figure 3.7d. Even though the nanofiber is clearly distorted by the transfer process, all the p6P material have been transferred, no breaks appear in the nanofiber and the photoluminescence from the transferred nanofiber is still polarized, i.e. the p6P molecular orientation of the nanofiber appears to be maintained. The fact, that the p6P clusters in Figure 3.7d are not removed by the transfer process is completely opposite to the case in Figure 3.6c, where all the clusters are removed by the transfer process. The reason for this could be that the receiver substrate is closer to

the mica substrate during the transfer in Figure 3.6c, i.e. the capillary force is larger in this case, thereby removing the p6P clusters. A line scan of the nanofiber end in Figure 3.7d is depicted in Figure 3.7e, showing an 80nm steep nanofiber end. Such a steep nanofiber end is more likely to be due to the nanofiber crystal structure, than due to the edge roughness of the receiver substrate.

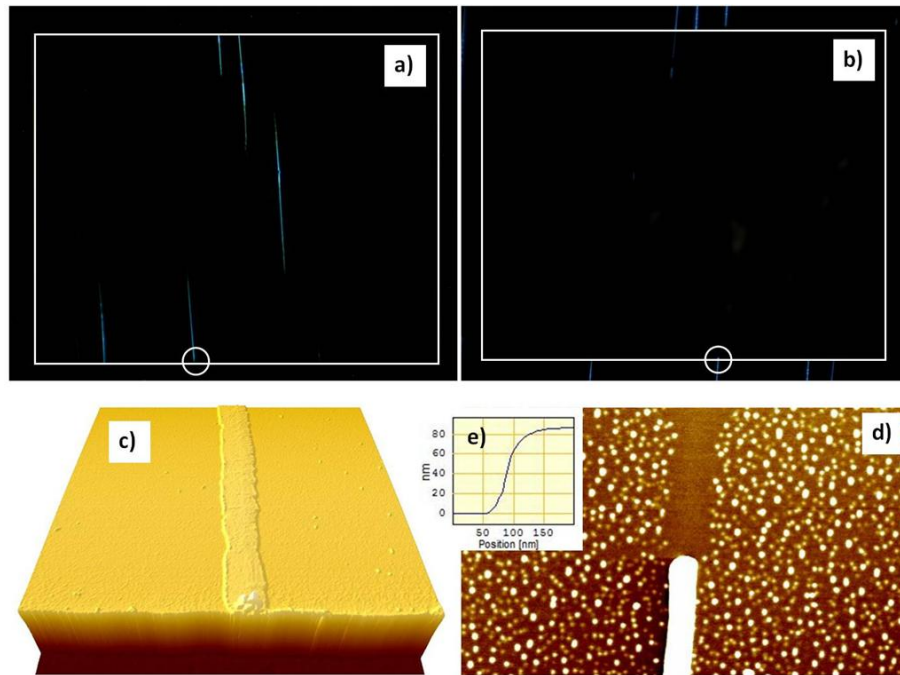


Figure 3.7: (a) A $1.2 \times 1 \text{ mm}^2$ fluorescence image of stamped nanofibers on a $1074 \times 875 \mu\text{m}^2$ elevated platform marked by the white square. (b) A $1.2 \times 1 \text{ mm}^2$ fluorescence image of the remaining nanofibers on mica. The white square outlines the receiver substrate contact area. (c) A $10 \times 10 \mu\text{m}^2$ AFM image of the stamped nanofiber marked with a white circle in (a). The nanofiber is 45nm high and $1.1 \mu\text{m}$ wide. (d) A $10 \times 6 \mu\text{m}^2$ AFM image of the nanofiber on mica marked with a white circle in (b). The nanofiber is 90nm high and 600nm wide. (e) A line scan of the nanofiber end in d), showing an 80nm steep end.

3.4 Large scale transfer of nanofibers to foil

In addition to stamping nanofibers directly onto desired device substrates as described above, attempts on transferring an entire 25x75mm² nanofiber sample from mica to a flexible PET-foil were made.

There are numerous benefits in transferring large-area nanofiber samples from their growth substrate to flexible foil, regarding later large scale implementation of nanofibers in devices.

- Due to its fragile nature muscovite mica is not a very ideal storage media, regarding handling and implementing nanofibers in devices. Having nanofibers on foil is preferable both regarding storage [56] and handling.
- Having nanofibers on foil opens up the possibility to use roll printing of nanofibers as the active element in devices.
- Nanofibers on foil also bare the possibility of producing large scale optoelectronic devices, such as *Organic Light Emitting Field Effect Transistors* (OLEFETs), on flexible substrates.

3.4.1 Transferring nanofibers to foil

The principle in transferring nanofibers from mica to foil is the same as described above - water droplets are applied on a PET-foil surface; followed by pressing the foil onto the nanofiber mica substrate.

The transfer of an entire 25x75mm² nanofiber sample from mica to flexible foil compared to the transfer of nanofiber areas of the order 200x200μm² to a hard device substrate both complicates and eases the transferring process. The fact, that the nanofibers have to be in contact with the foil over the entire sample area complicates the transfer. Fortunately, the foil is flexible and therefore able to adapt to e.g. mica cleavage steps. The softness of the PET-foil on the other hand leads to less distortion of the transferred nanofibers.

Nanofibers are transferred to foil by the transferring machine shown in Figure 3.8. The machine is fully computer controlled via LabView programming and is a first attempt to scale up the transfer process. The transferring sequence is as follows:

- A nanofiber mica sample is placed on the rotatable stamp head and fixed by vacuum applied to the backside of the mica.
- Flexible PET-foil is placed between the two aluminum frames.
- The upper aluminum frame is pulled towards the lower aluminum frame by two electromagnets, where a rubber ring mounted in the lower aluminum frame seals the room below the foil.
- The stamp head is turned 180° by the rotating motor and moved towards the foil by the two linear motors, until a 1mm distance between the foil and the nanofiber mica sample remains.

- An ultrasonic transducer produces water vapor, which is added in the space between the mica and foil through the nozzle holes in the upper aluminum frame
- Pressurized air is applied in the cavity below the foil, forcing the foil in contact with the nanofiber mica sample.
- The pressurized air is released, the stamp head moves up and the electromagnets fixing the foil are released.
- The PET-foil with transferred nanofibers can be removed and everything can start over again.

The computer controlled process provides precise control over duration of vapor inlet, duration between vapor inlet and contact of foil and mica and duration of applied pressurized air.

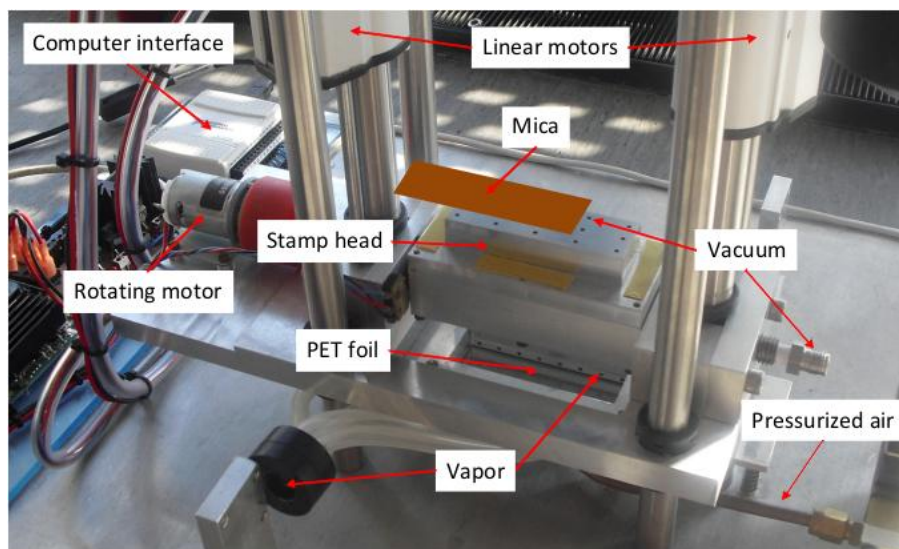


Figure 3.8: Computer controlled machine for transferring an entire $25 \times 75 \text{mm}^2$ nanofiber sample from mica to flexible foil. The nanofiber mica sample is positioned with 1mm distance to the foil. Ultrasonic produced vapor is blown in between the mica and the foil, followed by pressurized air applied to the backside of the foil, forcing the foil in contact with the nanofiber mica sample.

Numerous large scale transfers to foil with different transfer parameters were performed. The results of these experiments were promising, but also clearly revealed the limitation in the transfer process described above. Figure 3.9a shows an image of PET-foil with transferred nanofibers. The blue spot corresponds to nanofibers emitting blue light when excited with UV-light. Basically the entire $25 \times 75 \text{mm}^2$ nanofiber sample was transferred from the mica substrate to the foil. Thus, the foil is able to adapt to the mica surface by applying pressurized air to the backside of the foil.

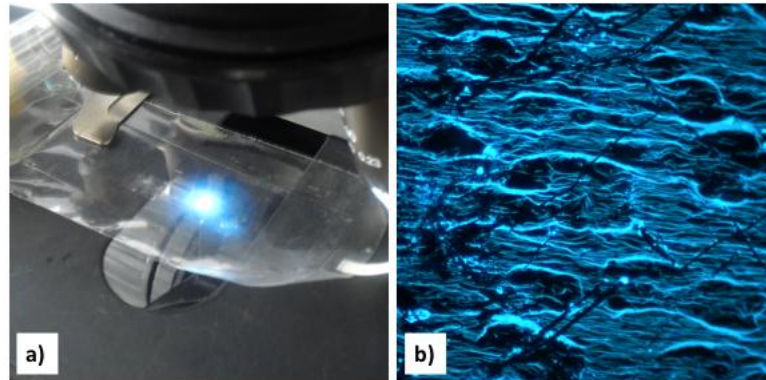


Figure 3.9: (a) An entire $25 \times 75 \text{ mm}^2$ nanofiber sample transferred from mica to PET-foil. The transferred nanofibers emits blue light under UV excitation. (b) A $200 \times 200 \mu\text{m}^2$ luminescence image of nanofibers transferred to foil. The nanofibers are somewhat disordered by the transfer process.

A closer inspection of the transferred nanofibers reveals other drawbacks in the transferring process though. Figure 3.9b depicts a $200 \times 200 \mu\text{m}^2$ luminescence image of the transferred nanofibers, which shows that the nanofibers are misaligned around condensed water droplet circles. There are two reasons for this. First of all the condensed water droplets are too large, i.e. the vapor control is inadequate and secondly the condensed water cannot escape, resulting in water pockets in between the mica and the foil, when the foil is pressed towards the mica. A possible way to avoid this trapping of water droplets between mica and foil is to roll the foil in contact with the nanofiber mica sample, thereby reducing the contact area and making it possible for the condensed water droplets to escape.

3.5 Summary and outlook

This chapter contains a description of nanofibers transferred from mica to prefabricated silicon receiver substrates by a special stamping technique, where small droplets of DI-water are condensing on the receiver substrate in a controlled atmosphere. During the transfer the mutual parallel nature of the nanofibers is maintained, whereas the nanofiber orientation on the receiver substrate can be defined within $\pm 6^\circ$. The nanofibers are transferred without any use of chemicals or sticking layer on the receiver substrate, where the nanofibers and the receiver substrate are only exposed to DI-water during the transfer process, thereby minimizing chemical alternation of the interface between the transferred nanofibers and the receiver substrate. The physical alternation of the nanofibers is on the other hand considerable during the transfer process. Due to the direct stamping of the soft nanofibers onto a hard silicon receiver substrate, the nanofibers are in the worst case “squeezed” to half their original height and twice their original width. Even though the nanofibers are squeezed the polarized photoluminescence from the nanofibers is retained, i.e. the molecular orientation inside the nanofibers are largely retained. Since the nanofiber height is in the order

of 30-150nm the roughness of the receiver substrate has to be low and transfer area has to press equally on the nanofiber mica substrate. Any tilt between the two surfaces will lead to incomplete transfer of the nanofibers. The release process of nanofibers from the muscovite mica substrate is deduced to be mainly capillary forces of the water droplets, neutralizing the forces binding the nanofibers to the mica surface, not excluding that other forces can be play a role in the transfer process.

The major problems with the above described stamping technique are the lack of control over the force applied to the stamp (leading to squeezing of the nanofibers) and unequal pressure between the receiver substrate transfer area and the nanofiber mica sample (leading to incomplete transfer of the nanofibers). These two issues can be solved by making a stepper motor driven, computer controlled and mechanically stable stamping machine, where the applied force is measured and controlled by e.g. a strain gauge. Another problem is that the droplet shape of condensed DI-water on the receiver substrate leads to interruption of the mutual parallel alignment of the nanofibers. Especially when one tries to transfer larger areas (e.g. mm^2) of nanofibers, the condensed water has difficulties escaping the contact area without moving the nanofibers in the lateral direction i.e. the nanofibers are moved by the moving waterfront of the condensed water droplet. It might be beneficial to make the receiver substrate more hydrophilic by adding some adhesive layer, thereby reducing the condensed DI-water droplet height or even better the DI-water condense as a thin film on the receiver substrate.

It has been shown that it is possible to transfer large nanofiber areas ($25 \times 75 \text{mm}^2$) from muscovite mica to polyethylene terephthalat (PET) foil. Even though the overall nanofiber orientation is maintained, the shown technique causes local misalignment of the transferred nanofibers. This is mainly due to the condensed waters inability to escape the contact area of the PET-foil and the nanofiber mica substrate. This does not mean that it is impossible to make this large scale transfer in a controlled way. Instead of pressing all of the PET-foil onto the nanofiber mica substrate at the same time, it might be better to role the PET-foil onto the nanofiber mica substrate, thereby reducing the contact area and making it possible for the condensed water to escape the contact area.

There are several interesting future applications of nanofibers transferred to a flexible foil. One is to use the foil as a more advantageous storage medium than muscovite mica. This requires however that the nanofibers can be transferred from the storage foil to the desired device substrate. Another is to make an *Organic Light Emitting Field Effect Transistor (OLEFET)* device directly on the foil, thereby obtaining a flexible optoelectronic device that is cheap and easy to manufacture.

4 Electrical Properties of p6P Nanofibers

The field of semiconductor nanowires is growing rapidly with more than 5000 nanowire related articles published in 2009 [57]. A main driving factor is the expected application potential, and a range of nanowire-based devices have been demonstrated such as an electrically pumped nanowire laser [58], sensitive chemical and bio-chemical sensors [59], and an electrical nanowire detector for optical plasmons [60]. One of the remaining challenges is the step from proof-of-concept of some device functionality requiring weeks or months of man-power to fabricate a small number of samples to large-scale integration enabling commercialization of such nanowire-based devices.

Much focus has been given to the integration of *inorganic* semiconductor nanowires. However, for a number of applications especially within optics and optoelectronics, organic materials have a range advantages over their inorganic counterparts – most notably the ability to tailor their properties by chemical synthesis of appropriate molecular building blocks [28]. Despite much less attention gives to these organic nanostructures, many of the same device functionalities must be expected with better tunability than for the inorganic systems.

The focus here will be on integrating p6P nanofibers in a prefabricated *Field effect transistor* (FET) device platform, by the stamping technique described in the previous chapter. This work has been done in collaboration with Jakob Kjelstrup-Hansen and Luciana Tavares⁽¹⁾

4.1 Principle of Organic Field Effect Transistors

Organic semiconductors can similar to inorganic semiconductors be used as the active element in a FET device. There are some distinct differences though. In contrast to inorganic semiconductors which typically are either p- or n-doped, organic semiconductors typically are used as intrinsic semiconductors in Organic Field Effect Transistors (OFETs). Several different OFET designs exist today, these includes top and bottom source/drain contacts, top and bottom gate contact and multilayer organic semiconductor material.

Here the focus will be on the two different designs shown in Figure 4.1. In the bottom contact configuration (Figure 4.1a) the organic semiconductor is lying on top of the source and drain contacts, where semiconductor, source and drain are

⁽¹⁾ Assistant Professor Jakob Kjelstrup-Hansen and Ph.D. student Luciana Tavares, MCI, University of Southern Denmark.

isolated from the bottom gate contact by a thin silicon dioxide layer. The other configuration shown in Figure 4.1b is a top contact configuration where the source and drain contact are placed on top of the semiconductor. The top contact configuration is known to reduce the contact/semiconductor interface [61].

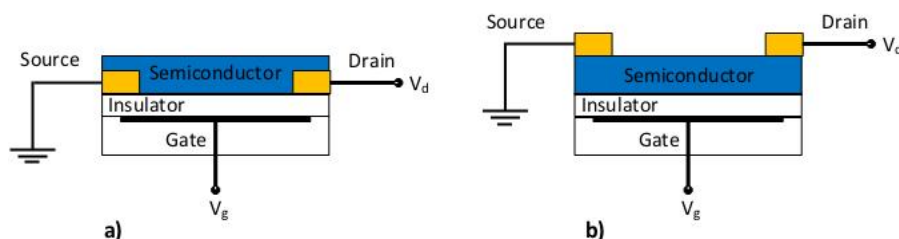


Figure 4.1: Two different OFET designs. The bottom gate is used in both cases. (a) Bottom source/drain contact configuration. (b) Top source/drain contact configuration

Since organic semiconductors are intrinsic semiconductors the working principle differs from the usual doped inorganic semiconductor, where either a p- or n-type conducting channel is introduced in the semiconductor by doping. The working principle of an OFET can be understood from the energy schemes in Figure 4.2. The energy scheme resembles an OFET device with gold source and drain contacts and p6P as the semiconductor. Gold has a work function of 5.1-5.47eV [62] and the HOMO and LUMO level for p6P is 6.0eV and 2.9eV, respectively [63]. The device is ambipolar meaning that both hole transport in the HOMO level and electron transport the LUMO level is possible through the p6P semiconductor. In the unbiased case in Figure 4.2a the hole and electron injection barrier is 0.8eV and 2.3eV respectively, making the unbiased OFET device a p-channel type i.e. the device will begin to conduct at a lower voltage if a positive voltage is applied to the drain than if a negative voltage is applied to the drain. Figure 4.2b depicts the energy scheme when the device is negative biased. The negative gate voltage will “push” the HOMO and LUMO levels up, reducing the hole injecting barrier to the HOMO level, resulting in a more p-channel type device i.e. the device will begin conducting at a lower positive drain voltage than in the unbiased case. The opposite is valid in the negative biased case in Figure 4.2c. The negative gate voltage will “pull” the HOMO and LUMO levels down, reducing the electron injection barrier to the LUMO level, theoretically resulting in a more n-channel type device. Other physical aspects, such as high injection barriers and electron traps, make it difficult to realize n-type transport in p6P [61].

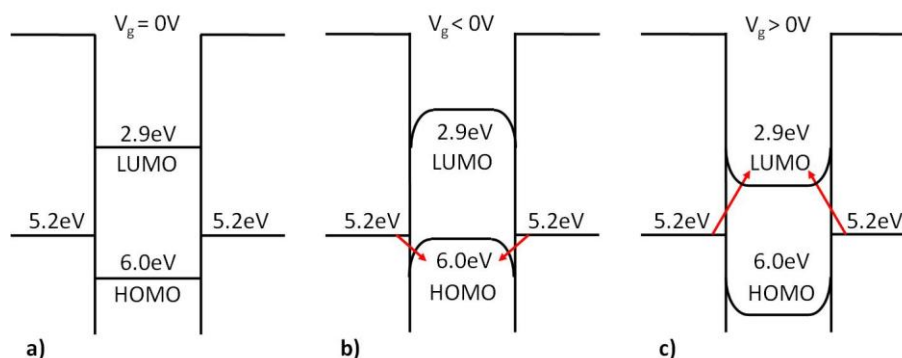


Figure 4.2: Schematic energy scheme for an ambipolar OFET, consisting of gold contacts (work function 5.2eV) and p6P semiconductor (HOMO 6.0eV and LUMO 2.9eV). (a) Unbiased device. The OFET is slightly p-channel type (b) Negative biased device “push” the energy bands up resulting in more p-channel type device. (c) Positive biased device “pulls” the energy bands down resulting in n-channel type device.

4.1.1 Organic Light Emitting Field Effect Transistors

A more promising route, than a nanofiber OFET device, is to implement the nanofibers in an *Organic Light Emitting Field Effect Transistor* (OLEFET) device. Thus having the nanofibers work as single nanowire light sources. The device structure of an OLEFET can be similar to the FET devices shown in Figure 4.1. In order for the semiconductor to emit light, both holes and electrons have to be simultaneously injected in the HOMO and LUMO band respectively. After that electron-hole exciton bonding and relaxation can occur, causing emission of light. Recently a novel operation mode regarding light emitting OFETs was proposed by T. Yamao et al. [64]. Here an enhanced luminescence was observed in 2,5-bis(4-biphenyl)thiophene by applying an alternating gate voltage. This operation mode is believed to be beneficial, when trying to obtain electroluminescence from single p6P nanofibers.

4.2 Field effect transistor device design

The challenge is now to design a FET device where it is possible to implement stamped p6P nanofibers as the active organic semiconductor element. The choice fell on the FET design shown in Figure 4.3.

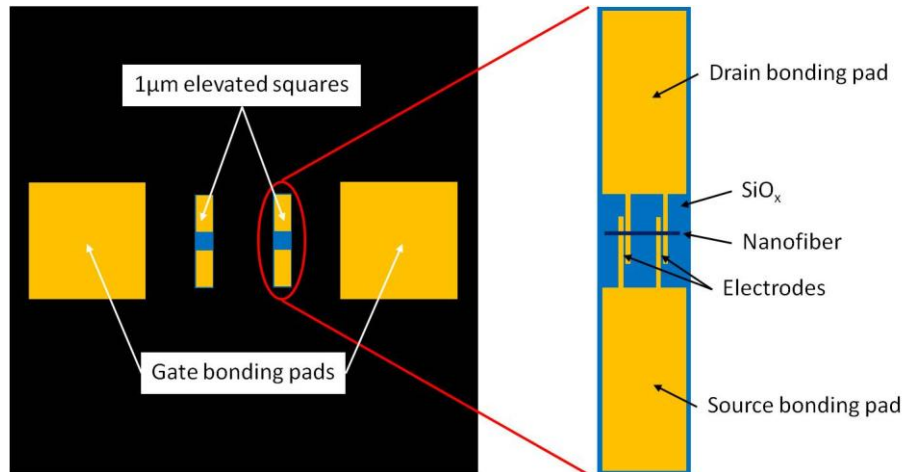


Figure 4.3: Field Effect Transistor (FET) device design. Two $200 \times 1000 \mu\text{m}^2$ elevated silicon rectangles with 200nm silicon dioxide on top. Two source/drain bonding pads (gold) are deposited on each of the two elevated squares. Two gate bonding pads (gold) makes connection to the underlying highly doped silicon. Bottom contact configuration: the four electrodes are deposited, follow by stamping of nanofibers. Top contact configuration: nanofibers are stamped follow by deposition of gold electrodes through a stencil mask.

The two $200 \times 1000 \mu\text{m}^2$ rectangles in the middle of the $5 \times 5 \text{mm}^2$ substrate are etched out in a highly n-doped (phosphorus) wafer with 200nm silicon dioxide on top. The 200nm silicon dioxide is etched by Hydrofluoric acid (HF), followed by an additional $1 \mu\text{m}$ ICPRIE etch in the revealed silicon. A second photolithography step defines the two gate bonding pads and the four source/drain bonding pads, followed by Physical Vapor Deposition (PVD) of 2nm titanium and 30nm gold. The following step depends on whether top contact or bottom contact configuration is desired.

- For the bottom contact configuration, the electrodes are defined by photolithography, followed by PVD of 2nm titanium and 28nm gold⁽¹⁾. Nanofibers are then stamped on top of the gold electrodes in the direction given in Figure 4.3.

⁽¹⁾ Complete recipe for the FET device substrate is given in appendix B

- For top contact configuration nanofibers are stamped onto the elevated squares in the direction given in Figure 4.3, follow by PVD of 30nm gold electrodes through a manually aligned silicon nitride stencil mask⁽¹⁾.

4.2.1 Nanofiber field effect transistor

Numerous nanofiber FET samples have been made with different electrode gap distances (from 2 μm to 12 μm) in both bottom and top contact configuration. The focus here will be on two samples showing some transistor characteristics in the experimental part of this chapter.

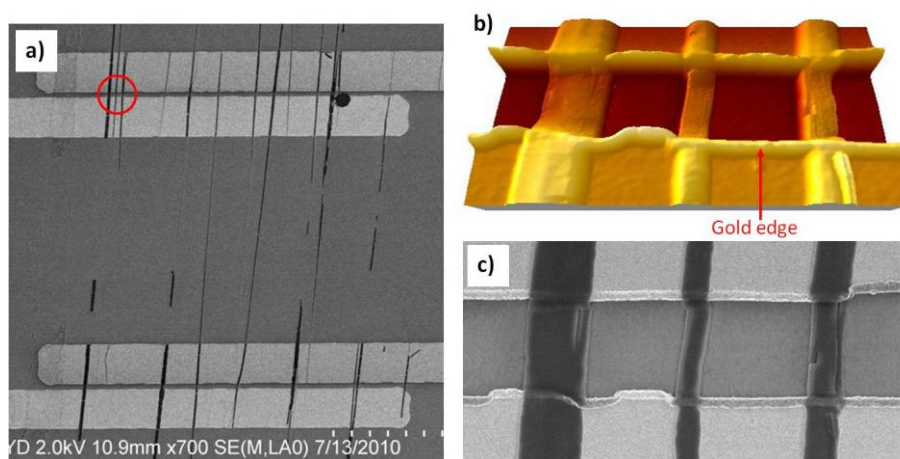


Figure 4.4: Bottom contact FET configuration. (a) 120x120 μm^2 SEM image of nanofibers stamped onto bottom electrodes. (b) 6x3 μm^2 AFM image of the three nanofibers marked with a red circle in a). The nanofibers are 40-50nm high and 400-1000nm in width. The gold electrode gap and height are 1.4 μm and 40nm respectively. The marked gold edge is 40nm high. (c) 6x3 μm^2 SEM image of the same three nanofibers as in b).

Figure 4.4a shows a 120x120 μm^2 SEM image of nanofibers stamped on top of a bottom contact FET substrate. Ten and seven individual nanofibers seams to be crossing the upper and lower electrode gap, respectively. A closer look at the transferred nanofibers reveals some problematic issues in stamping nanofibers onto bottom contacts. Figure 4.4b depicts a 6x3 μm^2 AFM image of the three nanofibers marked with a red circle in Figure 4.4a. The height of the deposit gold electrodes is 30nm and this surface height difference makes it difficult to stamp the 30-40nm high nanofibers, i.e. the nanofibers have a tendency to break at the edge of the gold electrodes. The AFM image also reveals a sharp 40nm high gold step at the edge of the gold electrodes. This sharp gold step originates from the photoresist lift-off procedure when making the FET substrate and can probably be avoided by optimization of the manufacturing method. The sharp gold edge cuts the nanofibers, resulting in a reduced gold/nanofiber contact area and thereby a

⁽¹⁾ Development of the silicon nitride stencil mask is a part of Luciana Tavares Ph.D. project and will be presented there.

reduced electron/hole injection area. Inspecting the AFM image and the $6 \times 3 \mu\text{m}^2$ SEM image in Figure 4.4c of the same three nanofibers, the nanofibers appear to make contact with the two gold electrodes though, thus current transport should be possible to obtain at least in some of the nanofibers.

Figure 4.5a shows a $120 \times 120 \mu\text{m}^2$ SEM image of nanofibers stamped onto the silicon dioxide gate between the source and drain bonding pad, followed by PVD of 30nm gold top electrodes through a nitride stencil mask. Eight nanofibers contact the upper electrode gap and two nanofibers contact the lower electrode gap. Figure 4.5b depicts a $1.6 \times 3 \mu\text{m}^2$ SEM image of the nanofiber marked with a red circle in a). The nanofiber shows rectangular morphology (from the stamping process) with the nanofiber width being 800nm. The deposited gold electrodes make sharp electrode edges over a $1.75 \mu\text{m}$ electrode gap.

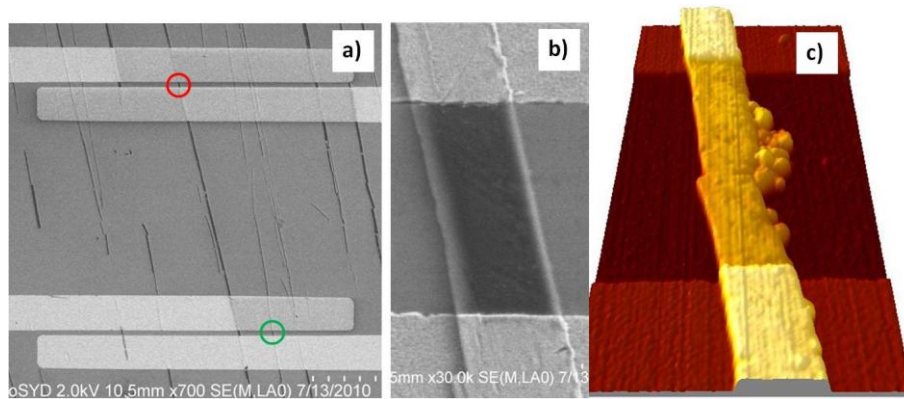


Figure 4.5: Top contact FET configuration. (a) A $120 \times 120 \mu\text{m}^2$ SEM image of nanofibers stamped onto the FET gate oxide followed by PVD of top electrodes through a nitride stencil mask. (b) A $1.6 \times 3 \mu\text{m}^2$ SEM image of the nanofiber marked with the upper red circle in a). The electrode gap is $1.75 \mu\text{m}$ and the nanofiber width is 800nm. (c) A $1.6 \times 3 \mu\text{m}^2$ AFM image of the nanofiber marked with the lower green circle in a). The gold electrode height is 30nm and the nanofiber height and width is 80nm and 400nm, respectively.

Figure 4.5c depicts a $1.6 \times 3 \mu\text{m}^2$ AFM image of the nanofiber marked with a green circle in a). As in Figure 4.5b the nanofiber shows rectangular morphology with width and height being 400nm and 80nm, respectively. The gold electrode gap is $1.75 \mu\text{m}$ and the gold electrode height is 30nm. Comparing Figure 4.4 and Figure 4.5 the top contact configuration seems to be superior both regarding nanofiber morphology and nanofiber/electrode contact area. The nanofiber/electrode contact area could be further improved in the top contact configuration by angling the PVD of the gold electrodes, thereby providing improved gold side coverage of the nanofiber.

4.3 Electrical characterization setup

The electrical characterization is made using the custom-built⁽¹⁾, LabView-controlled measurement setup shown in Figure 4.6, where the drain and gate voltages are controlled by a 16-bit National Instruments DAQ card (PCI-6221) through two Falco Systems high voltage amplifiers (WMA-280 and WMA-02, respectively), and the current is measured by a Stanford Research SR 570 current amplifier. The measurement instruments are connected to the device using a probe station equipped with three 3-axis translation stages. The setup provides the ability to record the source-drain current when sweeping the drain voltage and keeping the gate voltage constant, or when sweeping the gate voltage and keeping the drain voltage constant.

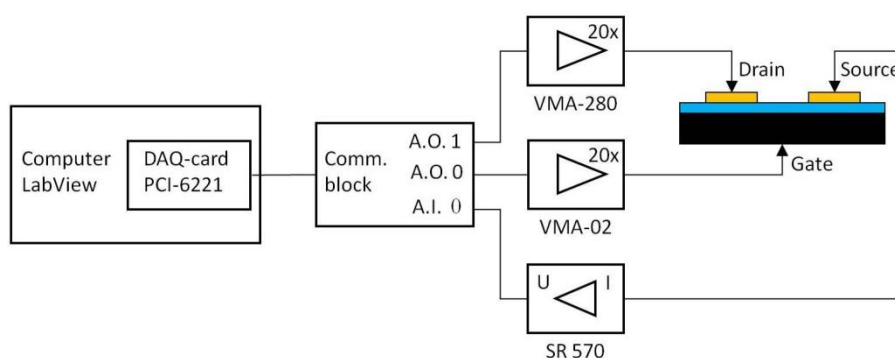


Figure 4.6: Electrical characterization setup. Custom-build LabView controlled drain and gate voltage, together with LabView monitored source-drain current.

4.4 Experimental results

The probe station with the three 3-axis translation stages caused some problems when obtaining transistor characteristics of the FET device. The probes tend to loose electrical contact to the source, drain and gate during the measurements, and more seriously they tend to damage the gate oxide. The gate oxide problem resulted in limited experimental data making quantitative transistor analysis impossible, e.g. it was not possible to make any gate voltage dependence measurement. Nevertheless a few I-V curves for both bottom and top contact configuration will be presented.

⁽¹⁾ The LabView controlled measurement setup is custom-build by Assistant Prof. Jakob Kjelstrup-Hansen, (MCI) SDU and Ph.D. Henrik Hartmann Henrichsen, (MIC) DTU.

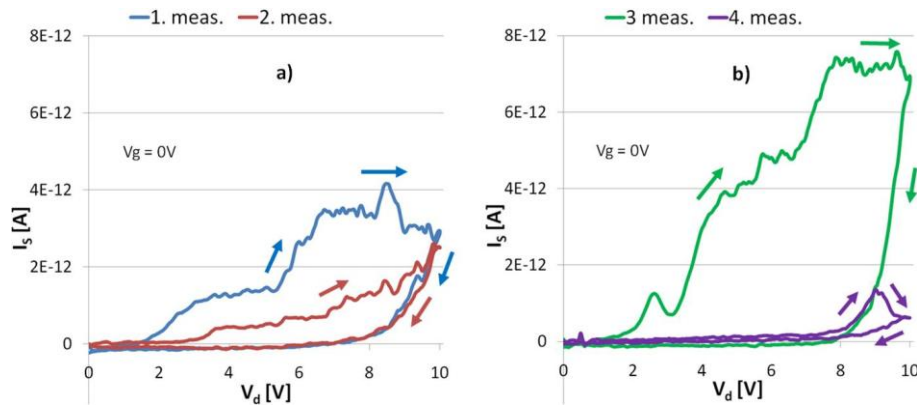


Figure 4.7: Output characteristics for the bottom contact configuration in Figure 4.4. (a) Two measurements made immediately after each other (first blue, second red). (b) Two new measurements made immediately after each other one hour after the measurements in (a) (third green, fourth purple).

Figure 4.7 depicts four different looking output characteristics obtained from the bottom contact configuration in Figure 4.4. The first measurement (blue curve in Figure 4.7a) depicts a low turn-on voltage around 1V, followed by a non exponential source current (I_s) rise when sweeping the drain voltage (V_d) from 0V to 10V with 0.5V/s (forward sweep). Sweeping V_d back from 10V to 0V (backward sweep) results in a more exponential decrease of I_s with I_s equal to 0A when V_d is equal around 7V, thus the I_s - V_d curve shows hysteresis between forward and backward sweep of V_d . The red curve in Figure 4.7a depicts the same measurement obtained immediately after the first the I_s - V_d curve. Here, the turn-on voltage is around 3V and I_s increases more slowly when sweeping V_d to 10V. Also here the curve shows hysteresis, where the backward sweep follows the backward sweep of the first measurement. A possible explanation of hysteresis nature could be charges building up at the gold/nanofiber contact interface and/or at the nanofiber/gate oxide interface. These charges create electron/hole traps that limit the current. This also gives a possible explanation of the non exponential nature of the first I_s - V_d curve (green curve). Since the current flows in individual nanofibers the created electron/hole traps will not limit the current homogeneously, i.e. the current is limited more in some nanofibers compared to other nanofibers resulting in the interrupted I_s - V_d curve in forward sweep. This is somewhat substantiated by the I_s - V_d curve in Figure 4.7b, showing the same two measurements as in Figure 4.7a made one hour later, thus giving the buildup charges time to relax. The two I_s - V_d curves show same tendency as in Figure 4.7a. The first measurement (green curve) shows interrupted current in forward sweep and the second measurement (purple curve) shows suppressed current compared to the green curve.

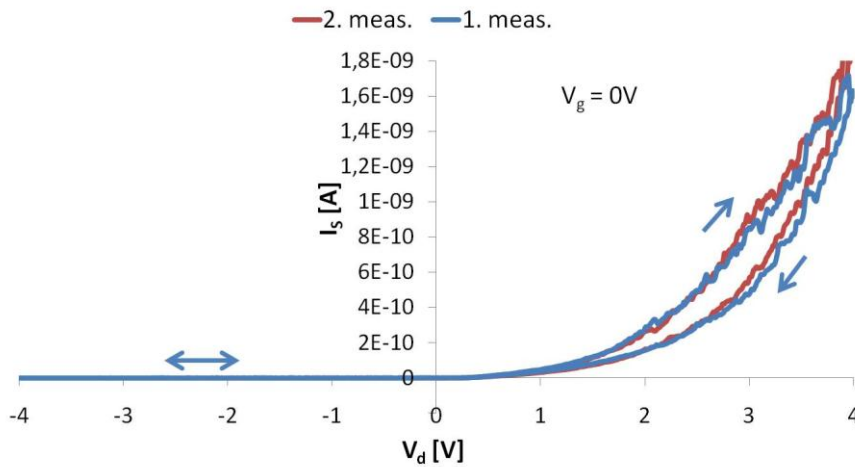


Figure 4.8: Two output characteristics for the top contact configuration in Figure 4.5. The OFET shows low turn on voltage (1V) and p-channel behavior.

Figure 4.8 depicts two similar output characteristics for the top contact OFET configuration in Figure 4.5. The two I_s - V_d curves are obtained immediately after each other, thus no indication of the charging/trapping interruption proposed regarding the bottom contact configuration. The OFET experience a lower turn on voltage (less than 1V) and a two order of magnitude higher current than in the bottom contact configuration. This supports the hypothesis that top contact configuration reduces the contact/nanofiber resistance compared to the bottom contact configuration. The I_s - V_d curve also shows experience hysteresis in forward/backward sweep and p-channel behavior as expected.

The measurement is somewhat questionable since the source/drain short-circuited shortly after this measurement was made and it might therefore be a gate oxide effect, which is shown and not current transport through the nanofibers. Recently, electrical measurements⁽¹⁾ on transferred nanofibers have shown more reliable results of current transport through the nanofiber. These measurements also reveal a gate effect of the current transport, which will be further investigated in the near future.

⁽¹⁾ Made by Luciana Tavares.

4.5 Summary and outlook

It is shown that it is possible to implement organic p6P nanofibers as the active element in a prefabricated FET device by stamping the nanofibers directly from the growth substrate onto the FET device. Both bottom and top source/drain configuration have been achieved and output characteristics shows that the top contact configuration reduces the gold/nanofiber injection barrier. The morphology of nanofibers stamped to bottom contacts configuration supports this, since the nanofibers tends to be cut by the edge of the gold electrode, thereby reducing the gold/nanofiber hole injection area.

The obtained output characteristics are both limited and questionable, thus further investigation is necessary to identify the electrical properties of stamped nanofibers and to achieve the main goal; single nanofibers as light emitting sources. As mentioned earlier numerous nanofiber FET samples were made, but only a few of these samples showed electric conductivity. The reason for this could either relate to the measurement setup, nanofiber stamping process or the nanofiber growth process. It is important to clarify these issues in the future work on nanofibers as single nanostructured light emitting sources.

5 Plasmon coupling to p6P Nanofibers

Photonic circuits are known to be much faster than their electronic counter parts. A drawback regarding photonic circuits is, that they are difficult to miniaturize below the optical wavelength scale. *Surface Plasmon Polaritons* (SPPs) based nanoscaled photonic circuits might be the solution to this problem, since they can localize light below the diffraction limit. Another problem arises though regarding detection of the SPPs, since there is a general trade-off between the localization of an SPP and the efficiency with which it can be detected by conventional far-field optics.

Here, an attempt is made on guiding SPPs excited in a gold-nanofiber interface and detect the SPPs with Photo Emission Electron Microscopy (PEEM). The presented PEEM measurements are made in collaboration with Till Leissner and Michael Bauer⁽¹⁾ at the PEEM setup at Technische Universität Kaiserslautern.

5.1 Surface plasmon polariton theory

The field of plasmonics has been intensely investigated over the last decade, nevertheless are all aspects of SPPs not fully understood. The plasmonic theory presented here is not in any way complete, but should more be seen as a short description of what is presented in the experimental data.

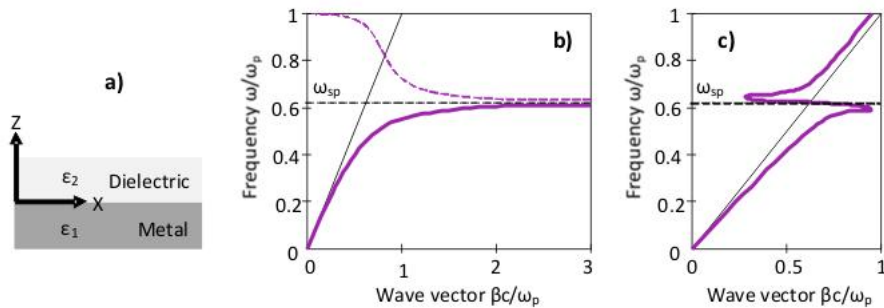


Figure 5.1: (a) A metal-dielectric interface. (b) Dispersion relation of SPPs at the interface between a perfect metal and air. (c) Dispersion relation of SPPs at a real metal-air interface. Due to the damping, the wave vector of the bound SPPs approaches a finite limit at the surface plasmon frequency.

Surface plasmon polaritons are electromagnetic waves bound in a metal/dielectric interface as shown in Figure 5.1a. Solving Maxwell's equations at the metal/dielectric interface reveals that SPPs only exists for *transverse magnetic polarization* (TM-mode) i.e. the magnetic field vector (\mathbf{B}) is oriented parallel to the metal/dielectric interface and perpendicular to the wave vector [65].

⁽¹⁾ Ph.D. stud. Till Leissner and Prof. Michael Bauer, IEAP, Christian-Albrechts-Universität zu Kiel.

The dispersion relation of SPPs propagating at the metal-dielectric interface is given by [65]:

Equation 5.1

$$\beta = k_0 \sqrt{\frac{\varepsilon_1(\omega)\varepsilon_2(\omega)}{\varepsilon_1(\omega) + \varepsilon_2(\omega)}}$$

Where β is the SPP wave vector, $k_0 = \omega/c$ is the wave vector of the propagating wave in vacuum, $\varepsilon_1(\omega)$ is the dielectric function of the metal and $\varepsilon_2(\omega)$ is the dielectric function of the dielectric. The dielectric function of a metal is a complex value, where the real part is negative i.e. $\text{Re}[\varepsilon_1(\omega)] < 0$. The imaginary part of $\varepsilon_2(\omega)$ can usually be neglected, thus the dielectric function of a dielectric is a real positive value i.e. $\text{Re}[\varepsilon_2(\omega)] > 0$ and $\text{Im}[\varepsilon_2(\omega)] = 0$. Taking this into account and neglecting any imaginary part of $\varepsilon_1(\omega)$, it is seen from Equation 5.1, that the SPP wave vector is going towards infinity when $\varepsilon_1(\omega) = -\varepsilon_2(\omega)$. This situation is depicted in Figure 5.1b, where the SPP dispersion curve (purple line) for a metal/air interface and the air dispersion curve (black line), is shown. For low frequencies, the SPP dispersion curve is slightly shifted to the right of the air dispersion curve, but as the frequency approaches a critical frequency (called the *surface plasmon frequency* ω_p) the SPP wave vector goes to infinity, giving rise to a large field enhancement in the metal/air interface. The surface plasmon frequency (ω_{sp}) is given by [65]:

Equation 5.2

$$\omega_{sp} = \frac{\omega_p}{\sqrt{1 + \varepsilon_2}}$$

Where ω_p is metal plasma frequency. Above the surface plasmon frequency the SPP wave vector is purely imaginary showed by the dashed purple line in Figure 5.1b. Note that the SPP dispersion is lying to the right of the dispersion curve for light traveling in vacuum. This momentum mismatch, equivalent to the horizontal distance between the two dispersions curves, prevents SPPs to be excited by an incident electromagnetic field. The SPP dispersion curve changes to the picture shown in Figure 5.1c, when taking the imaginary part of the metal dielectric function into account. Due to the damping i.e. energy loss in the metal, the wave vector of the bound SPPs approaches a finite limit at the surface plasmon frequency.

There are different possibilities to overcome the momentum mismatch between the incident light and the SPP e.g. excitation of plasmons via grating or total internal reflection, but also steps or defects in the metal surface will cause excitation of SPP. Figure 5.2b shows how a SPP wave is excited at a silver edge. Surface plasmon polaritons are excited in a silver/vacuum interface by a tunable

pulsed laser beam at impact angle $\theta = 65^\circ$. The laser light polarization is as mentioned above TM-mode in order to excite plasmons. When the incoming laser light experience a step in the silver film, the momentum mismatch Δk (represented by the green arrow in Figure 5.2a) is overcome and an exponential decaying SPP traveling wave is introduced in the silver/vacuum interface, with wavefronts parallel to the silver edge. The shadowed grey area represents in Figure 5.2a represents the frequency and bandwidth of the incoming laser beam.

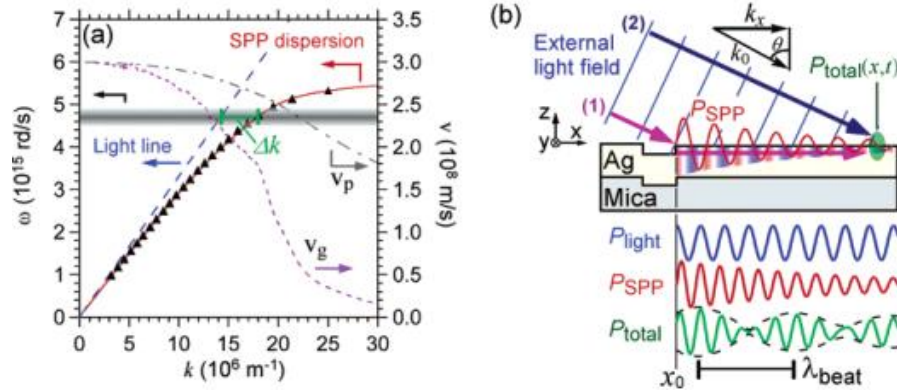


Figure 5.2: (a) Dispersion curve for silver (red curve) and light in vacuum (dashed blue line). The shaded gray area represents the laser pulse wavelength and bandwidth. Δk represents the momentum mismatch between the laser light and the SPP, which has to be overcome in order to excite SPPs. (Reprinted from [66]). (b) An edge in the silver will excite an exponential decaying SPP wave in the silver/vacuum interface. The exponential decaying SPP wave (red curve) will interfere with the incoming laser light (blue curve), resulting in a beating pattern of the total electromagnetic field in the silver/vacuum interface (green curve). (Reprinted from [66]).

The total electromagnetic field observed in the silver/vacuum interface (green curve in Figure 5.2b) is a superposition of the incoming laser beam (blue curve in Figure 5.2b) and the SPP wave (red curve in Figure 5.2b):

Equation 5.3

$$P_{total} \propto \cos\left(\frac{\Delta k}{2}x\right) \sin\left(\frac{k_{x,light} + k_{SPP}}{2}x\right) e^{-\kappa x}$$

Where κ denotes the damping and the relation between momentum mismatch Δk and beat wavelength (λ_{beat}) is given by:

Equation 5.4

$$\Delta k = k_{SPP} - k_{x,light} = \frac{2\pi}{\lambda_{beat}}$$

In the work presented here, the sample is not silver on mica, but gold on silicon. This will change the dispersion curve in Figure 5.2a, but the basic principle is the same.

5.2 Experimental setup

A schematic drawing of the experimental setup is shown in Figure 5.3. The sample is loaded in a UHV chamber, where a PEEM, a mercury lamp and a sputter gun is mounted. The commercial PEEM (Focus IS-PEEM) used here is described in detail in [67]. After the gold sample is loaded in the UHV chamber a submonolayer of cesium (Cs) is sputtered onto the sample. This is done to lower the sample work function from gold ($\sim 5.2\text{eV}$) to cesium (2.14eV) making it possible for the PEEM to extract electrons from the sample. Surface plasmon polaritons are excited by a tunable (740-860nm) pulsed Ti:Sapphire laser system with repetition rate 80MHz and pulse length 120fs. The polarization of the pulsed laser beam is controlled by a zero-order half-wave plate in combination with a Glen-Thompson polarizer, making it possible to excite the sample with both p-polarized and s-polarized light. The pulsed laser beam is focus on the sample to a beam diameter of approximately $100\mu\text{m}$ and the laser beam impact angle is $65^\circ \pm 2^\circ$ to the sample surface normal. The sample can in addition to the pulsed laser be excited by a mercury lamp. The mercury lamp is usually used to locate the sample area of interest.

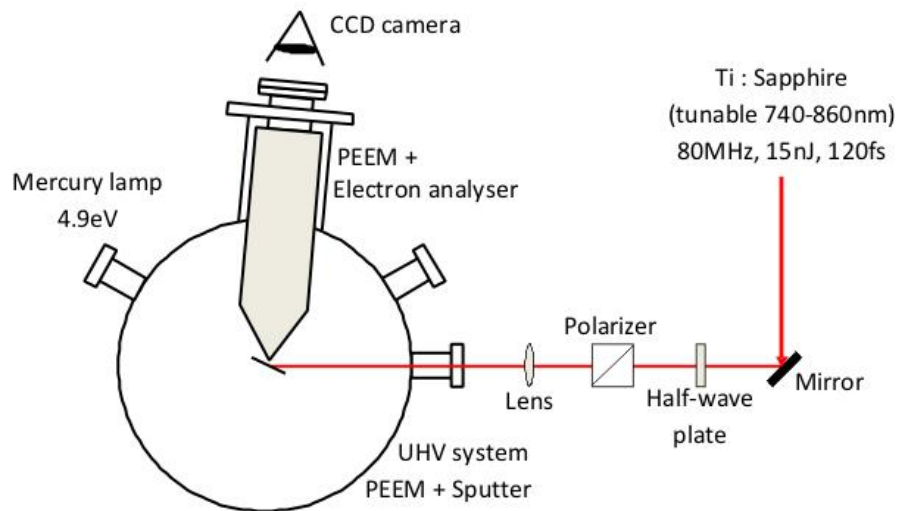


Figure 5.3: Experimental setup. Beside the PEEM a sputter gun and a mercury lamp is also mounted in the UHV system. The sample is excited by a tunable (740-860nm) pulsed Ti:Sapphire laser at an impact angle of $65^\circ \pm 2^\circ$ to the sample surface normal.

5.3 Sample preparation

A PEEM sample with various gold structures on a silicon substrate was made by means of both photolithography and *Electron Beam Lithography* (EBL). First the silicon substrate in Figure 3.1a was defined by photolithography and ICPRIE, secondly the structures in Figure 5.4a were defined by EBL (writing field $100 \times 100 \mu\text{m}^2$) followed by 60nm gold deposited by *physical vapor deposition* (PVD)⁽¹⁾.

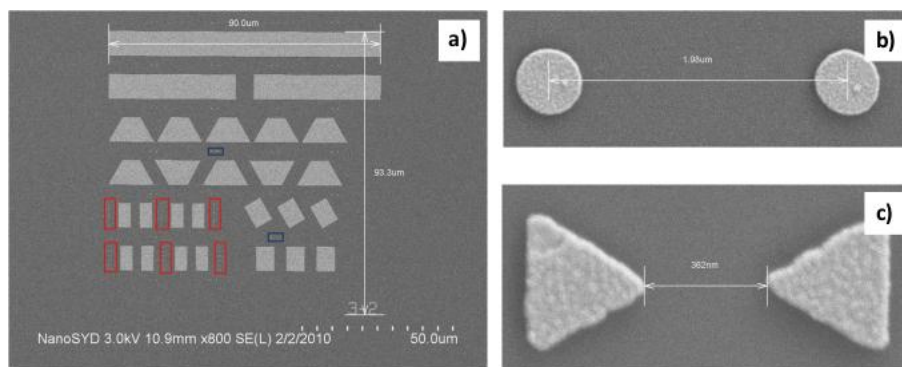


Figure 5.4: SEM images of the fabricated 60nm gold on silicon PEEM sample. (a) All the large elements have a height of $8 \mu\text{m}$. The red and blue squares outline areas with nano antennas and PEEM drift correction spots, respectively. (b) PEEM drift correction spots. The spots are distant by $2 \mu\text{m}$ and are 430nm in diameter. Twenty-eight drift correction spot pairs are position different places on the PEEM sample. (c) The nano antennas consist of two triangles with side length 400nm and distant by 360nm .

The gold structures in Figure 5.4a are positioned on each of the nine elevated squares of the test substrate in Figure 3.1a. The gold circle pair in Figure 5.4b, placed twenty-eight different places in the PEEM structure, works as PEEM drift correction spots, with diameter 430nm and distant by $2 \mu\text{m}$. Figure 5.4c depicts a gold triangle pair attended to work as Bowtie antennas i.e. giving rise to a large field enhancement between the triangles. The triangle pairs are placed in the outlined red areas in Figure 5.4a, where the two triangles are distant by 360nm and have side lengths 400nm . The idea of the PEEM sample design is to have transferred nanofibers of different length, defined by the isosceles trapezoid and rectangular gold structures, thereby providing the possibility to investigate any nanofiber length dependence in the obtained PEEM images. Figure 5.5a depicts the PEEM substrate in Figure 5.4a with p6P nanofibers transferred to the surface, showing both nanofibers cut at the edge of the gold structures and nanofibers bridging the gold structures, providing the possibility for the mentioned investigations.

⁽¹⁾ The complete PEEM sample recipe is shown in Appendix B

It will become clear however from the next title, that the obtained PEEM images are difficult to interpret. Therefore the main focus will be on a nanofiber marked with a white arrow in Figure 5.5b, positioned on the isosceles trapezoid outlined by the red square in Figure 5.5a. The red arrow in Figure 5.5b indicates the direction of the incoming laser beam.

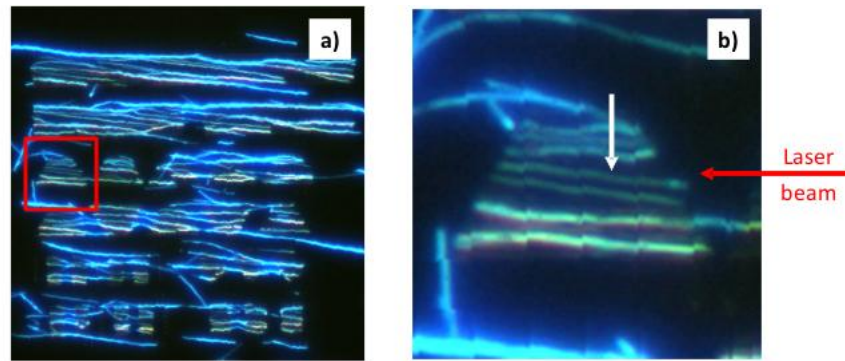


Figure 5.5: (a) A $100 \times 100 \mu\text{m}^2$ fluorescence image of nanofibers stamped onto the PEEM structures. (b) A $20 \times 20 \mu\text{m}^2$ zoom in on the outlined red square in (a). The nanofiber marked with a white arrow will be analyzed in the experimental results. The red arrow depicts the direction of the incoming laser beam.

5.4 Experimental results

Figure 5.6 shows six different PEEM images of the gold isosceles trapezoid in Figure 5.5b. In Figure 5.6a, b) and c) the gold/nanofiber sample is excited by p-polarized light with wavelengths of 745nm, 810nm and 860nm, respectively. And in Figure 5.6d, e) and f) the gold/nanofiber sample is excited by s-polarized light with wavelengths of 745nm, 810nm and 860nm, respectively. The intensity of the PEEM images cannot be compared directly, but in general the intensity from *Transverse Magnetic field mode* (TM-mode) PEEM images (sample excited with p-polarized light) are higher than the intensity from *Transverse Electric field mode* (TE-mode) images (sample excited with s-polarized light). Also, the images obtained from short excitation wavelength (745nm) are more intense than the images obtained from long excitation wavelength (860nm). The nanofibers are more or less visible in all of the images except from image c), especially in image d) all of the nanofibers shown in Figure 5.5b are clearly visible. The bright-dark-bright field running parallel to the right side of the gold trapezoid in image a), b) and c) resembles the SPP-laser light beating pattern of the SPP wave excited at the gold edge (the right side of the trapezoid). This beating pattern is not affected by the nanofibers, but is solely due to the excited SPP wave in the gold/vacuum interface. The bright-dark-bright field is absent in image d), e) and f) where the excitation light beam is s-polarized and SPPs are therefore not excited.

Since the nanofibers are visible in both the TM- and TE-mode PEEM images, there must be an enhanced field at the nanofiber position in both cases. There are two most likely explanations to the enhanced field in the TE-mode case, where no SPPs are excited.

1. The nanofibers are excited by two photon absorption from the incoming pulsed laser beam.
2. The incoming light is coupled inside the waveguiding nanofibers.

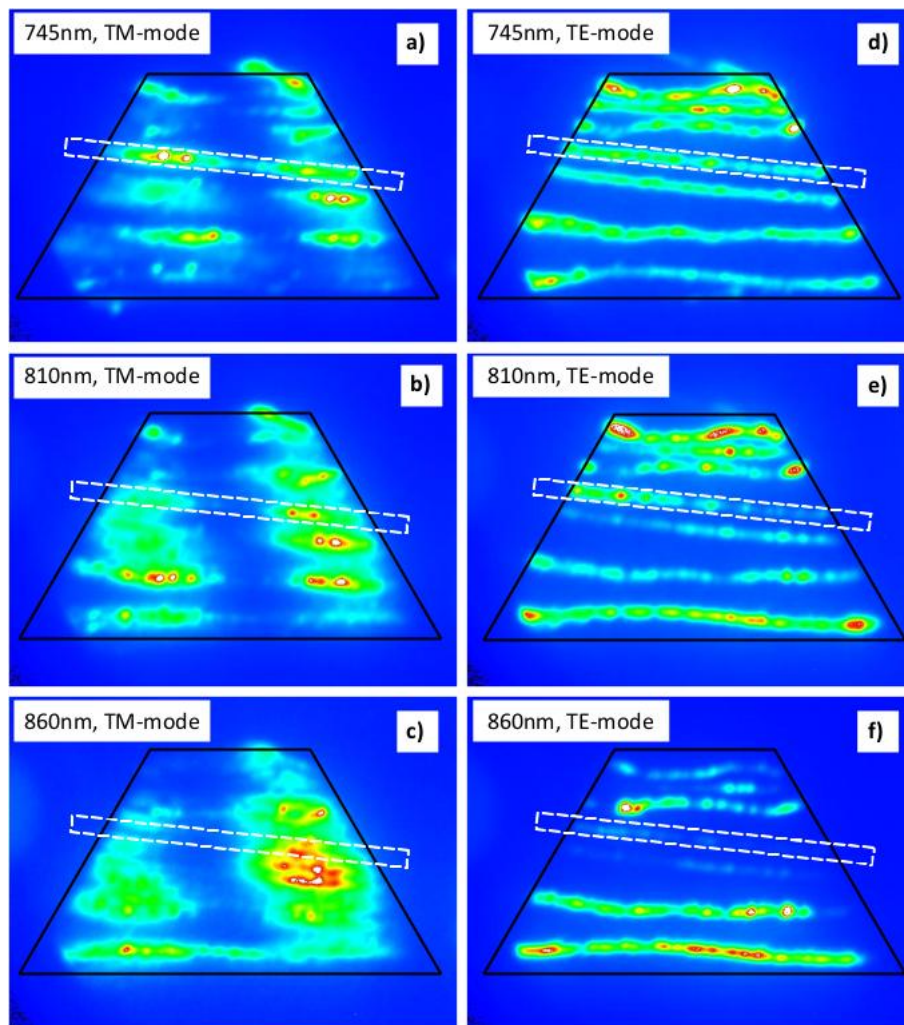


Figure 5.6: Six images obtained by PEEM. In (a), (b) and (c) the sample is excited by p-polarized light with wavelength 745nm, 810nm and 860nm, respectively. In (d), (e) and (f) the sample is excited by s-polarized light with wavelength 745nm, 810nm and 860nm, respectively. The black isosceles trapezoids outline the gold structure in Figure 5.5b and the white squares outline the nanofiber marked with a white arrow in Figure 5.5b.

Looking at TE-mode in image d), e) and f) the upper nanofibers are losing intensity for increasing excitation wavelength. This is valid for both suggested explanations.

Ad 1) At excitation wavelengths above 800nm, two photon excitation of the nanofibers are no longer possible causing a drop in intensity

Ad 2) The nanofiber morphology limits waveguiding of longer wavelengths, i.e. the nanofibers are too small to guide light at higher wavelengths [31].

The fact that the intensity from the two lowest nanofibers in images d), e) and f) seems more or less constant compared to the intensity from the upper most nanofibers, implies that waveguiding of the incoming light is the most likely explanation for the enhanced field in the nanofibers, since the relative nanofiber intensity should not change due to two photon excitation. Thus, the two lowest nanofibers have larger width compared to the upper nanofibers, thereby provide waveguiding at longer wavelengths. Unfortunately the PEEM sample was not recovered from the UHV chamber; it is therefore not possible to obtain nanofiber morphology by AFM.

Bright spots (or varying intensity pattern) are observed in all of the imaged nanofibers in Figure 5.6. These intensity patterns look more or less periodic and could therefore originate from standing electromagnetic waves inside the nanofibers or at the nanofiber/gold interface. A more thorough examination of the intensity pattern will therefore be made in the next title.

5.4.1 Intensity pattern analysis

Figure 5.7 shows the integrated intensity (blue curve) of the area outlined by the white square in Figure 5.6a. The figure shows some clear intensity peaks lying above the light/SPP beating pattern depicted by the dashed black curve. From the beating pattern fit, the beat wavelength (λ_{beat}) is found to be $5.28\mu m$, giving the following momentum mismatch Δk , SPP wave vector k_{SPP} and SPP wavelength:

Equation 5.5

$$\Delta k = \frac{2\pi}{\lambda_{beat}} = \frac{2\pi}{5.28\mu m} = \underline{1.19\mu m^{-1}}$$

$$k_{SPP} = k_{x,light} + \Delta k = \frac{2\pi}{745nm} \sin 65 + 1.19\mu m^{-1} = \underline{8.83\mu m^{-1}}$$

$$\lambda_{SPP} = \frac{2\pi}{k_{SPP}} = \frac{2\pi}{8.83\mu m^{-1}} = \underline{711nm}$$

From literature the optical constants n_1 and κ_1 for gold at 745nm are found to be 0.138 and 4.453, respectively [68]. Thus, the dielectric function for gold at this wavelength is:

Equation 5.6

$$\varepsilon_1 = n_1^2 - \kappa_1^2 = 0.138^2 - 4.453^2 = \underline{-19.81}$$

The SPP wavevector β can be calculated from Equation 5.1, where the dielectric function $\varepsilon_2(\omega)$ for vacuum is 1:

Equation 5.7

$$\beta = \frac{2\pi}{\lambda} \sqrt{\frac{\varepsilon_1(\omega)\varepsilon_2(\omega)}{\varepsilon_1(\omega) + \varepsilon_2(\omega)}} = \frac{2\pi}{745nm} \sqrt{\frac{-19.81 \cdot 1}{-19.81 + 1}} = \underline{8.66\mu m^{-1}}$$

This result matches the experimentally found SPP wavevector (k_{SPP}) in Equation 5.5 within a reasonable error.

Especially, the left side of Figure 5.7 (between 3 μ m and 5 μ m) shows strong intensity peaks, with intensities way above the beating pattern. If the intensity peaks originate from either SPP coupling or waveguiding in the nanofiber, one would expect some periodicity in the peak positions even if not all of the intensity peaks are resolved in the image.

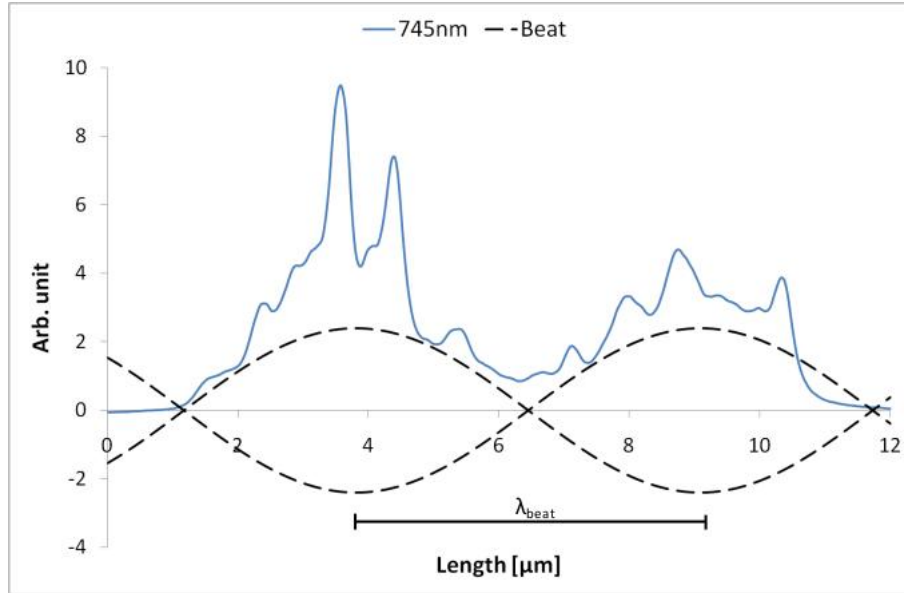


Figure 5.7: Integrated intensity (red curve) from the area outlined by the white square in Figure 5.6a. The light/SPP beating pattern is depicted by the dashed black curve with beat wavelength $\lambda_{beat} = 5.28\mu m$.

As seen in the picture, it is difficult to determine the exact peak positions due to insufficient resolution, but any intensity peak periodicity should appear in the Fourier Transform.

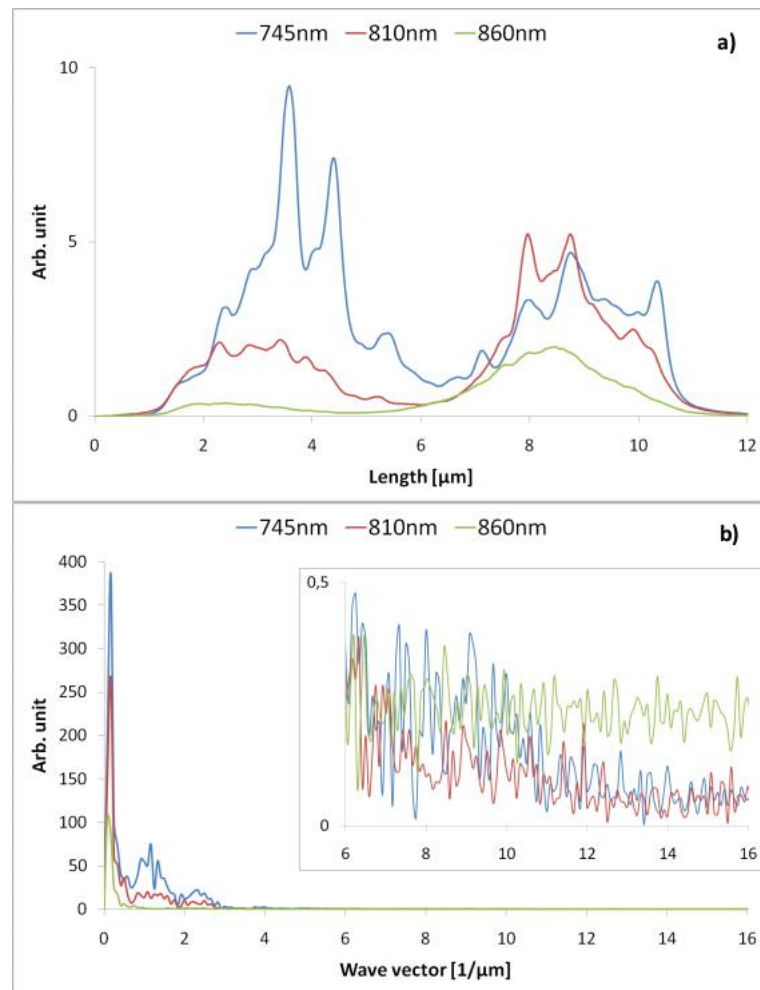


Figure 5.8: (a) Integrated intensity for the outlined areas in Figure 5.6a blue curve, Figure 5.6b red curve and Figure 5.6c green curve. The incident light is in all three cases p-polarized. (b) Discrete Fourier Transform of the three intensity curves in a)

Figure 5.8a shows integrated intensity from the outlined area in Figure 5.6a (blue curve), Figure 5.6b (red curve) and Figure 5.6c (green curve), where the incoming light in three cases is p-polarized, and the wavelength of the incoming light is 745nm, 810nm and 860nm respectively. No intensity peaks are observed for excitation wavelength 860nm (inspecting Figure 5.6c the nanofiber actually appears dark), thus no electromagnetic field is coupling to the nanofiber in this case. Intensity peaks are observed both for excitation wavelength 745nm and for excitation wavelength 810nm. Some (but not all) of the intensity peaks coincide in the two cases, but maximum intensity shifts from the left side of the image for 745nm to the right side of the images for 810nm. Only taking the gold/vacuum SPP wave into account, the highest intensity should be in the right side of the image, since the SPP wave is excited at the gold edge to the right i.e. the beating pattern is exponentially decaying going to the left. Thus, the intensity peaks of the blue curve in the left side of the image are pronounced. Figure 5.8b shows the *Discrete Fourier Transform* (DFT) of the three integrated intensities in Figure 5.8a for excitation wavelength 745nm (blue curve), 810nm (red curve) and 860nm (green curve). The only resonance peaks observed is for short wave vectors e.g. the peak at $1.19\mu\text{m}^{-1}$ for the blue curve corresponding to the momentum mismatch Δk . The inset in Figure 5.8b shows a zoom on wave vectors from $6\mu\text{m}^{-1}$ to $16\mu\text{m}^{-1}$. Any periodicity in the peak intensity should be in this region, but as the insert shows no pronounced wave vectors are observed.

The same peak intensity analysis is done for the s-polarized, excited pictures in Figure 5.6d, e) and f). Figure 5.9a depicts the TE-mode integrated intensities for the three excitation wavelengths 745nm (blue curve), 810nm (red curve) and 860nm (green curve). Again some of the peak intensities coincide, but as for the TM-mode no periodicity of the intensity peaks are shown in the DFT in Figure 5.9b.

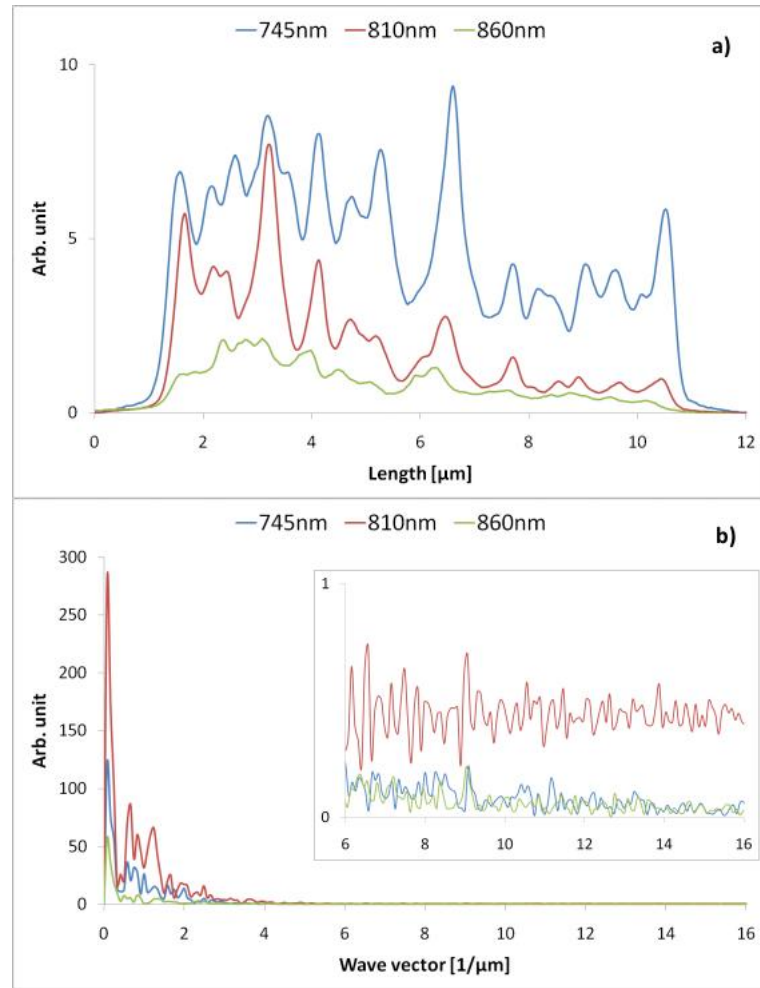


Figure 5.9: (a) Integrated intensity for the outlined areas in Figure 5.6d blue curve, Figure 5.6e red curve and Figure 5.6f green curve. The incident light is in all three cases s-polarized. (b) Discrete Fourier Transform of the three intensity curves in a)

5.5 Summary and outlook

It is difficult to conclude on the above presented PEEM images. The PEEM images in Figure 5.6 imply some electromagnetic field coupling to the nanofiber, but from where this electromagnetic field originates is difficult to determine. Three different scenarios are proposed:

1. Two photon excitation of the nanofiber.
2. The incoming laser light is coupled into the nanofiber.
3. Surface Plasmon Polariton wave is excited in the gold/nanofiber interface.

Ad 1) The two photon excitation of the nanofiber can be ruled out for the TM-mode. Here, the electric field vector of the incoming light is polarized (nearly) perpendicular to the long molecular axis of nanofiber p6P molecules, resulting in reduced absorption of the incoming light.

Ad 2) Calculation made in [31] on waveguiding in a single nanofiber concludes that *Transverse Electric* (TE) waves cannot exist in such a nanofiber. This implies that the increased nanofiber intensity in Figure 5.6d to e) originates from two photon absorption. More recent calculation of Fabry-Pérot modes in a single nanowire states on the other hand, that TE- and TM-modes can coexist inside such a system [69]. Thus, the increased nanofiber intensity can also originate from incoming laser light coupled into the nanofiber.

Ad 3) It is a possibility that the TM-mode intensity peaks in Figure 5.6a and b) originates from a SPP wave induced in the gold/nanofiber interface, but due to the missing periodicity in the intensity peak positions it cannot be concluded. Another possibility is that roughness in the gold/nanofiber interface creates local SPPs which would explain the missing periodicity.

The last thing that has to be taken into consideration is the sputtered submonolayer cesium (Cs) on top of the sample in order to lower the work function. The sputtered cesium might not be a continuous film covering the nanofibers, but clusters of cesium on top of the nanofibers. This could explain the intensity peaks, but it does not explain the change in the intensity peak pattern for different excitation wavelength.

In order to clarify what the increased electromagnetic field in the nanofibers originates from, a new sample of nanofibers on gold has been made (Figure 5.10). Here, large and separated nanofibers have been transferred to two $1074 \times 875 \mu\text{m}^2$ elevated silicon platforms with 80nm gold on top. The larger nanofibers should be easier to detect and focus in the PEEM, thereby increasing the resolution of the PEEM images, thus increasing the resolution of the intensity peaks. Another interesting thing is, that on this sample both nanofibers starting at the gold edge and nanofibers starting on the continuous gold film are present. This provides the ability to see whether a nanofiber end can act as defect and excite SPPs in the gold/nanofiber interface. Unfortunately was the next available measuring period at the PEEM setup in Kaiserslautern after the deadline for handing in this thesis.

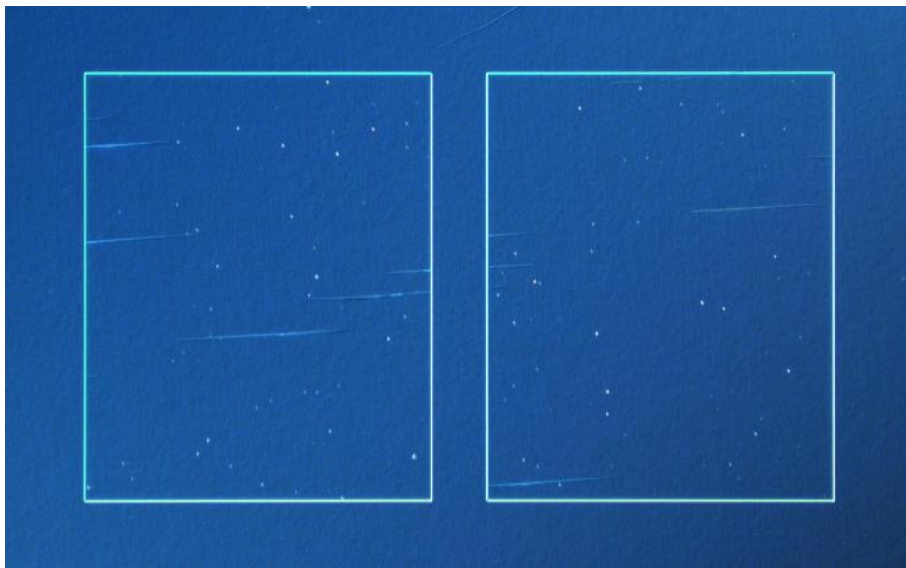


Figure 5.10: A $2.4 \times 1 \text{mm}^2$ contrast microscope image of stamped nanofibers on two $1074 \times 875 \mu\text{m}^2$ elevated silicon platforms ($1 \mu\text{m}$ high) with 80nm gold on top. The large and separated nanofibers should be ideal, regarding investigation of any SPP/nanofiber coupling

6 Another application

As mentioned earlier p6P nanofibers possess quite unique intrinsic properties, such as bright blue luminescence with well defined vibronic peaks, highly polarized luminescence, waveguiding and elongated nanoscopic morphology. These intrinsic properties led to the idea of using the nanofibers as security markers in the field of anti-counterfeiting. Counterfeiting is a rapidly growing and cost consuming problem for product producing companies, thus the field of anti-counterfeiting is also rapidly growing. The main technology used in anti-counterfeiting today is hologram based security markers made in thin plastic films. Depending on the technology used for making these holograms, the holograms contain feature sizes going from a few nanometers and up, providing several levels of security. The main problem with this technology is that it is a well known technology also by the counterfeiters. Implementing nanofibers in the already existing holography technology will add a new and to the counterfeiters unknown security level to the security markers.

6.1 Organic nanofibers as security markers

Figure 6.1 depicts three different examples of nanofibers implemented in already existing holograms. Figure 6.1a and b) shows two images of the same 100,- DDK banknote, where the banknote in b) is illuminated with a standard UV money checker (wavelength 380nm). In the middle of the illuminated spot in b) a small blue spot is visible. This blue spot originates from transferred light emitting p6P nanofibers and is not visible in a) where the banknote is not illuminated with UV light. The nanofibers are transferred from a nanofiber mica sample to the banknote, by placing a stamp below the banknote and gently press the nanofiber mica sample on top of the banknote in an atmosphere of high humidity. Figure 6.1c shows a zoom of the transferred light emitting nanofibers, revealing a triangular shape of nanofiber transfer area, thus it is possible to define the shape of the light emitting nanofiber area by the shape of the stamp. The nanofibers are transferred directly from the mica sample to the banknote, which results in considerable distortion of the nanofibers, due to the surface roughness of the banknote paper.

A more promising technique is to transfer the nanofibers to plastic foil, which has a lower surface roughness and is a widely used material in hologram based security markers. An example of p6P nanofibers implemented in a hologram on PET foil is shown in Figure 6.1d and e) where the holograms are illuminated with white light and white light plus UV-light, respectively. Again it is seen, that the transferred nanofiber areas (here shaped as a 3mm long arrows) are only visible when illuminated by UV-light. The nanofiber area is transferred to the PET foil in the same way as described above; a stamp below the PET foil defines the arrow shaped stamping area, water is condensing on the PET foil surface and a nanofiber mica

sample is pressed against the PET foil, resulting in nanofibers stamped onto the PET foil.

The ability to tune the luminescence from organic nanofibers by functionalizing the *para*-phenylene in its *para* positions [70], [71] makes it possible to use bicolor nanofiber based security markers. An example of this is shown in Figure 6.1f, where two blue vertical bars based on p6P nanofibers and one yellow horizontal bar based on thiol-functionalized nanofibers makes the bicolor security marker. The bars are approximately 2mm long. The blue background color originates from some chemical treatment of the underlying PET-foil.

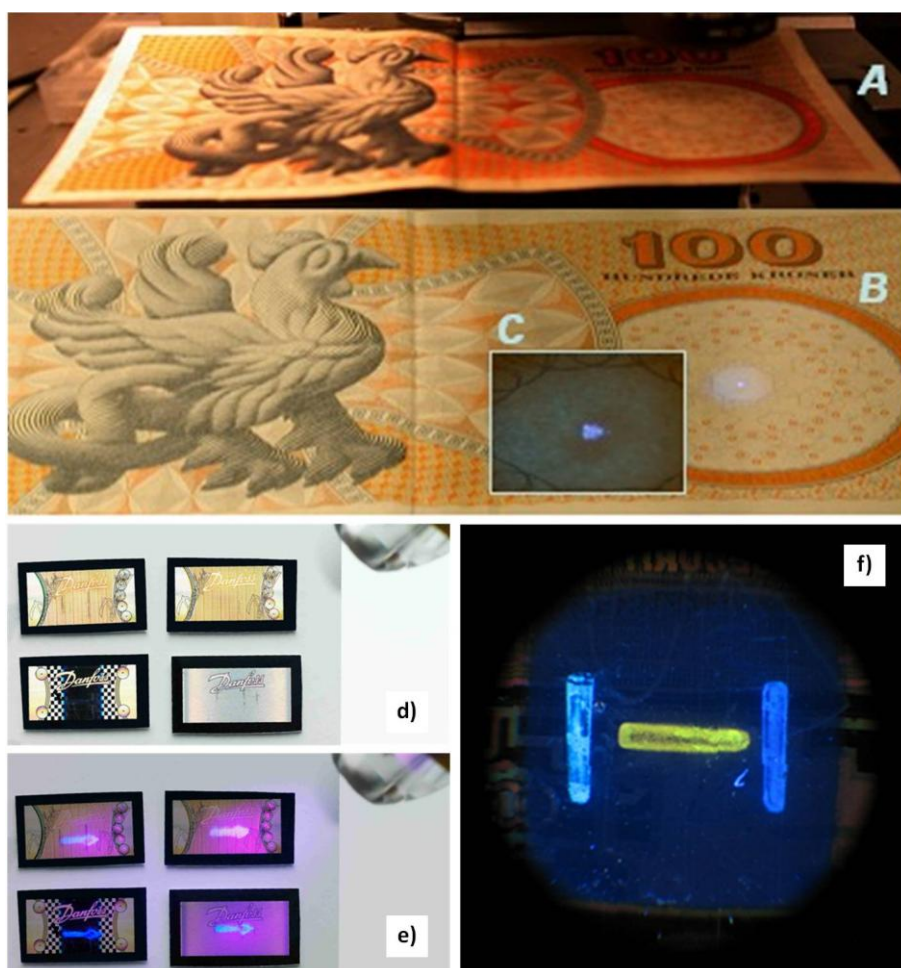


Figure 6.1: (a) A 100,-DDK Danish banknote. (b) The same banknote illuminated with a standard UV money checker. Nanofibers emit blue light in the middle of the illuminated spot. (c) A zoom on the illuminated spot. The blue nanofiber luminescence has a triangular shape. (d) Four $10 \times 5 \text{ mm}^2$ security holograms illuminated by white light. (e) Same four holograms as in d) illuminated by both white light and UV-light. (f) Bicolor security marker based on p6P nanofibers (blue color) and on thiol-functionalized nanofibers (yellow color).

6.1.1 Levels of security

The promising aspect of using organic nanofibers as security markers is that they without any further processing possess numerous security features. These security features are below categorized in three different levels of security, where security level 3 upholds the highest level of security.

Security level 1 (visual inspection):

- The nanofiber security markers are only seen when illuminated by UV-light, e.g. illuminated with a standard UV money checker which is already widely used in the security marked today (depict in Figure 6.1a to e)).
- Due to the waveguiding nature of the nanofibers, the luminescence from nanofiber security markers appears brighter when inspecting them from a shallow angle.
- The possibility of bicolor nanofiber security markers adds an additional visual feature in the security marker (depict in Figure 6.1f).

Security level 2 (polarization and spectrum):

- The polarized luminescence from p6P nanofibers can be used as yet another security feature. Inspecting the nanofiber security markers through a polarizer, the luminescence from the nanofibers can be turned “on” and “off” by rotating the polarizer (depict in Figure 6.2a and b)).
- The luminescence spectrum from p6P nanofibers contain four distinct vibronic peaks (depict in Figure 6.2c) with distinct ratios between the peak intensities. Analyzing the peak positions and intensity ratios in a spectrum analyzer provides yet another security feature to the nanofiber security markers.

Security level 3 (morphology):

- The unique elongated and mutual parallel nanostructure of the p6P nanofibers can be revealed by inspecting the nanofiber security markers in a UV-microscope (depict in Figure 6.2d)
- A more thorough inspection of the individual p6P nanofiber morphology of the nanofiber security markers can be revealed e.g. by obtaining an *Atomic force microscope* (AFM) image (depict in Figure 6.2e).

These seven security features makes it difficult to counterfeit the nanofiber security markers without actually producing identical nanofiber security markers e.g. the distinct luminescence spectrum from p6P nanofibers is defined by the individual p6P molecules and is hard, if not impossible, to counterfeit without using the same p6P material. Especially security level 2 contains security features with a high and easy detectable level of security. It is fairly cheap and easy to implement both a polarizer and a spectrum analyzer in a small apparatus indicating e.g. with

green and red lights, whether the security marker is a valid p6P nanofiber security marker. Such an apparatus has already been developed by the startup company Nanofiber A/S⁽¹⁾. The nanofiber security markers also have design-related advantages. Since they can be produced in various shapes, it is implement them in a visual nice way an already existing company logo.

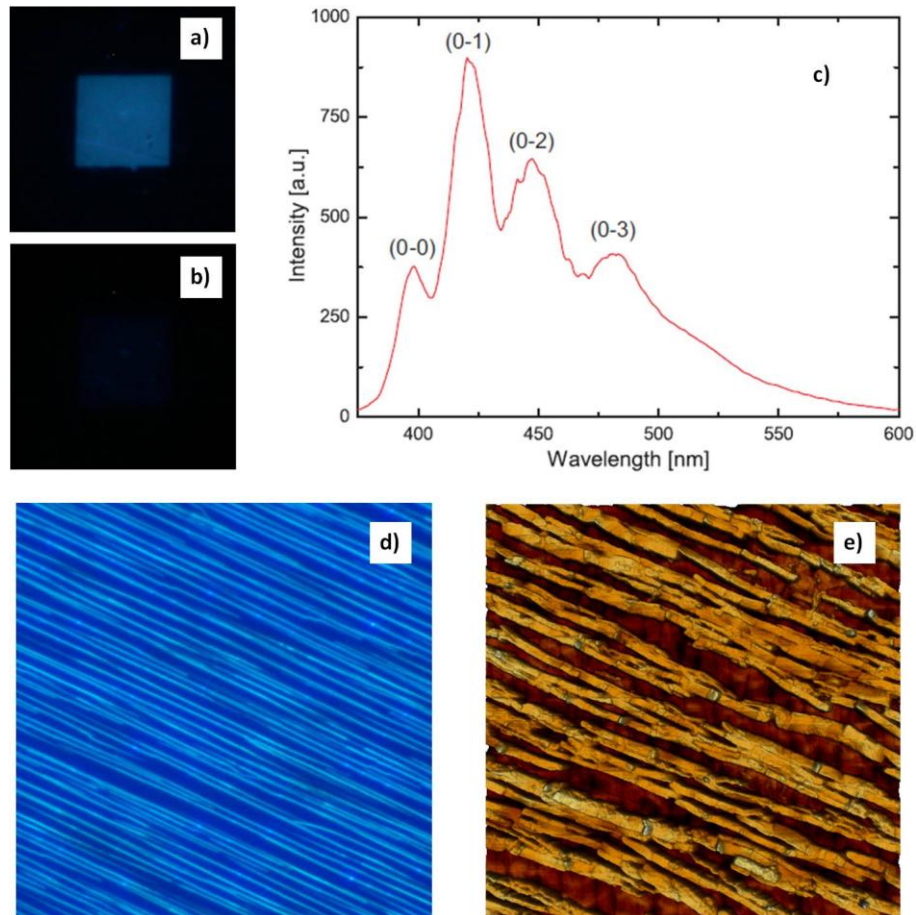


Figure 6.2: Different security levels in nanofiber security markers. (a) and (b) Two fluorescence images of the same $100 \times 100 \mu\text{m}^2$ area of dense nanofiber on PET foil representing p- and s-polarized luminescence, respectively. The dense nanofiber area has been stamped from a nanofiber mica sample. (c) Luminescence spectrum for a p6P nanofiber sample showing four distinct vibronic peaks (reprinted with permission of Morten Madsen). (d) $50 \times 50 \mu\text{m}^2$ fluorescence image of p6P nanofibers on mica. (e) $5 \times 5 \text{mm}^2$ AFM image of the stamped p6P nanofibers on PET foil depict in a) and b).

⁽¹⁾The startup company Nanofiber A/S was founded in July 2005 by the University of Southern Denmark and Novi Innovation A/S based on the presented nanofiber security marker technology.

6.2 Summary and outlook

As presented above, the nanofiber security markers bear substantial potential in the field of anti-counterfeiting. The crux of anti-counterfeiting is to a large extent, to be able to constantly implement new security features in the already existing security markers, there by being one step ahead of the counterfeiters. Nanofiber security marker technology is a new, unknown and completely different technology than what is used in the security marker business today, thus this aspect alone makes it an interesting technology for the anti-counterfeiting market.

The biggest challenges in implementing nanofibers in the security marker business are 1) cost per marker and 2) throughput.

Add 1) The marked price for p6P alone (over 1000,-€ per gram) will make the nanofiber security marker more expensive than the existing hologram based security markers on the market today. Thus, the nanofiber security markers are more suitable for high value products.

Add 2) In order to upscale the nanofiber production, one needs to reduce the production time per nanofiber mica sample, which at the moment is determined by the mica substrate heating time. A possible solution to this is to heat the mica substrate by radiant heating as suggested in Chapter 2.4. Security hologram labels are mainly produced in thin plastic foils, such as PET, with a high throughput (up to 60 meters of foil per minute [72]). The most promising way of implementing nanofiber security markers in security hologram labels with a reasonable throughput is a roll-to-roll printing technique. This requires that multiple nanofiber mica samples are transferred to a roll of thin plastic foil (as described in Chapter 3.4.1) and then implemented in security hologram labels by a roll-to-roll printing technique.

7 Conclusion

The main topic of this thesis is transfer of large areas of mutually parallel aligned organic para-hexaphenylene (p6P) nanofibers from their growth substrate muscovite mica onto pre-structured device platforms, which in the future might act as field effect transistors, plasmon polariton couplers and security markers.

Morphology and mutual separation of nanofibers during their growth depends strongly on the growth substrate temperature, which complicates growth on large mica plates due to the poor thermal conductivity of these substrates. A homogeneous muscovite mica temperature has been achieved by adding a thermally conductive layer between mica and hotplate. This, together with an on-surface measurement of the mica temperature, has made possible growth of homogeneous arrays of nanofibers on a 75x25mm² mica substrate. The on-surface temperature measurement, together with a quantitative control of the mica surface temperature, revealed:

- that the critical temperature of nanofiber growth is $453\pm 2\text{K}$, which deviates from what has been published earlier [39].
- that nanofibers grown at the critical temperature originate not only from 3-dimensional p6P crystallites forming a 1-dimensional crystallite chain, but also from 1-dimensional crystallite chains adding to already existing p6P nanofibers.

Subsequent annealing experiments indicate that some of the breaks which are visible in most nanofibers originate from stress introduced in the growth substrate during heating and cooling of muscovite mica.

Transfer of p6P nanofibers from their growth substrate is inevitable in order to implement nanofibers in devices. The nanofibers can be transferred to a desired device substrate by means of a simple drop-cast technique, followed by mechanically manipulation of individual nanofibers to a desired configuration [25]. A more promising route is, though, to print areas of mutually aligned nanofibers from their growth substrate directly to a desired device configuration, maintaining the mutual alignment of the nanofibers. This nanofiber printing technique has been developed in the present thesis by means of a custom-build nanofiber stamping machine. The transfer process takes place in an air atmosphere with defined temperature and humidity, resulting in water droplets condensing on the device substrate. When the device substrate is brought into contact with the nanofiber mica sample, the condensed water droplets release the nanofibers thereby transferring them to the device substrate. The release of nanofibers from their growth substrate is mainly due to capillary and electrostatic forces of the water droplets, screening and neutralizing the forces binding the nanofibers to the

wetting layer. The latter forces are most probably a mixture of electrostatic charging and van der Waals polarization binding forces. By means of this novel stamping technique, controlled transfer of $200 \times 200 \mu\text{m}^2$ nanofiber areas with an orientation control of $\pm 5^\circ$, has been achieved. Atomic force microscopy (AFM) images reveal a distortion of transferred p6P nanofibers in terms of height and width: the nanofiber height is reduced by a factor two and the width is correspondingly increased by a factor two. This distortion is inevitable using the presented mechanical stamping techniques.

Subsequently p6P nanofibers have been implemented as the active elements in a prefabricated field effect transistor (FET) device by stamping the nanofibers directly from the growth substrate onto the FET device. Electrical contact to the stamped nanofibers has been achieved in both bottom and top source/drain configuration of the FET device. Output characteristics reveal p-channel conduction in the nanofibers and a reduced gold/nanofiber injection barrier in top contact configuration. The morphology of nanofibers stamped to the bottom contacts configuration supports this, since the nanofibers tend to be cut by the edge of the gold electrodes, thereby reducing the gold/nanofiber hole injection area. Finally, nanofibers have been integrated on prefabricated and structured gold-on-silicon sample, serving as surface plasmon polariton (SSP) active substrates. Photoemission electron microscopy (PEEM) images of transferred p6P nanofibers on such substrates have been obtained. These include images where surface plasmon polaritons (SPPs) are excited by s-polarized, pulsed laser light at three different wavelengths at the gold/vacuum interface, resulting in nanofiber localized beating patterns in the PEEM images. Additionally, PEEM images have been obtained for p-polarized, pulsed laser light at three different wavelengths (in this case SPPs are not excited), which also shows nanofiber localized beating patterns. Thus, a tempting conclusion is that electromagnetic waves in both cases are coupled to the nanofibers.

Appendix A

List of Publications

Refereed papers

"The luminescence decay of oriented phenylene nanofibers", K. Thilsing-Hansen, M.T. Neves-Petersen, S.B. Petersen, R. Neuendorf, K. Al-Shamery and H.-G. Rubahn, Phys.Rev.B 72 (2005) 115213.

"Nano ink ribbon", K.Thilsing-Hansen and H.-G. Rubahn, PA 2007 00226 (2007).

"Nano ink ribbon", K.Thilsing-Hansen and H.-G. Rubahn, PCT/DK2008/050035; European Patent Application 08706932.4 (2009).

"Conduction and electroluminescence from organic continuous and nanofiber thin films",X.Liu, J. Kjelstrup-Hansen,K. Thilsing-Hansen, H.H.Henrichsen and H.-G. Rubahn, phys.sta.sol., accepted (2010).

Book article

"Nanooptics using organic nanofibers", S.Bozhevolnyi, K.Thilsing-Hansen and H.-G.Rubahn, in "New organic nanostructures for next generation devices", K.Al-Shamery, H.-G.Rubahn, H.Sitter, Eds., Springer Series in Materials Science 101, Berlin (2008)219.

Refereed proceedings

"Fast and ultrafast response of aligned organic nanofibers - towards organic nanolasers", S.B. Petersen, T.N. Petersen, F. Quochi, F.Cordella, K.Thilsing-Hansen, A.Mura, G.Bongiovanni and H.-G. Rubahn, SPIE 5937 (2005)1K.

"Printed second harmonic active organic nanofiber arrays", F. Balzer, J. Brewer, J.Kjelstrup-Hansen, M. Madsen, M. Schiek, K. Thilsing-Hansen, K. Al-Shamery, A. Luetzen and H.-G. Rubahn, SPIE 6779(2007)17.

"Electrical properties of in-situ grown and transferred organic nanofibers",R.M. de Oliveira Hansen,J. Kjelstrup-Hansen, K.Thilsing-Hansen, M. Madsen and H.-G. Rubahn, SPIE 7764-20 (2010).

Conference abstracts

"Ultrafast luminescence decay of organic nanofibers", K. Thilsing-Hansen, M.T. Neves-Petersen, S.B. Petersen and H.-G. Rubahn, Workshop on 2- and 3-D organic nanostructures, Linz (2005).

"UV excitation and polarized light emission from organized nanofibers", K. Thilsing-Hansen and H.-G. Rubahn, BIOMED 05, Risoe, Roskilde (24.11.)(2005).

"UV-laser treatment in the nanodomain: forming of organic nanofibers", F. Balzer, R. Frese, K. Thilsing-Hansen, J. Ihlemann and H.-G. Rubahn, LAMP06, Kyoto (2006).

"Cutting and patterning of organic nanofibers", F. Balzer, R. Frese, M.Madsen, K. Thilsing-Hansen and H.-G. Rubahn, Nanofair, Karlsruhe, 21-22.11. (2006).

"Ultrafast organic nanofiber dynamics", K. Thilsing-Hansen, R. Frese and H.-G. Rubahn, DOPS meeting Risoe, (2007).

"UV-laser induced structure formation for organic materials" , R.Frese, M. Madsen, K. Thilsing-Hansen and H.-G. Rubahn, 2nd German-Danish meeting on Interface Related Phenomena, Alsion, Sonderborg (2008)

"Functional nanomaterials via molecular nanotechnology", F. Balzer, J.Kjelstrup-Hansen, M. Madsen, M.Schiek, K. Thilsing-Hansen and H.-G. Rubahn, Zing Nanomaterials Conference, Cancun (2008).

"Conduction and electroluminescence from organic continuous and nanofiber thin films", X.Liu, J. Kjelstrup-Hansen, K. Thilsing-Hansen, H.H.Henrichsen and H.-G. Rubahn, TNT Barcelona (2009).

"Ambipolar light-emitting field-effect transistors based on organic nanofibers and thin films", J.Kjelstrup-Hansen, X.Liu, K.Thilsing-Hansen, H.H.Henrichsen and H.-G. Rubahn, MRS fall meeting (2009).

"Large-scale transfer of organic nanofibers by soft stamping", K.Thilsing-Hansen, J.Kjelstrup-Hansen and H.-G. Rubahn, MRS fall meeting (2009).

"Electroluminescent Field-Effect Transistors based on organic nanofibers and thin films", J.Kjelstrup-Hansen, X.Liu, K.Thilsing-Hansen, H.H.Henrichsen and H.-G. Rubahn, Smart Materials 3 workshop, Kiel (2009).

"Surface plasmon modulated light guiding in para-hexaphenylene based nanofibers studied by photoemission electron microscopy", Till Leißner, Michael Bauer, Jakob Kjelstrup-Hansen, K.Thilsing-Hansen, R.Oliveira de Melina Hansen and Horst-Guenter Rubahn, DPG Spring meeting (2010).

"Light guiding in para-hexaphenylene based nanofibers in interaction with a gold substrate studied by photoemission electron microscopy", Till Leißner, Michael Bauer, Kasper Thilsing-Hansen, Roana Melina de Oliveira Hansen, Jakob Kjelstrup-Hansen, and Horst-Günther Rubahn, DPG Spring meeting,(2010).

"On surface temperature control for large-scale growth of organic para-hexaphenyl (p6P) nanofibers on muscovite mica substrate", K. Thilsing-Hansen and Horst-Günter Rubahn, 4th spring PhD workshop SDU-OU-JKU, 'Organic materials for flexible devices', Sønderborg (2010).

"Comparison between p6P thin films and nanofibers on transistors platforms", L. Tavares, J. Kjelstrup-Hansen, K. Thilsing-Hansen and H.-G. Rubahn, ICPEPA 7, Copenhagen(2010).

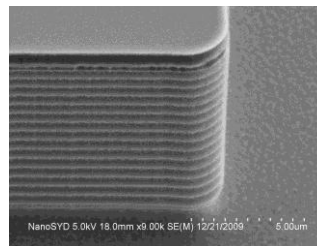
Appendix B

Process Recipe

Nanofiber transfer test substrate

Wafer: Standard Si(100) 4" wafer with a thickness of 500 μ m.

- HMDS:** Hexamethyldisilazane treatment for 30min. at 120°C.
- Photoresist:** AZ 5214E photoresist is deposited by spin coating at 4000rpm for 30s and prebaked at 90°C for 60s.
- Photolithography:** The photoresist is exposed to UV light for 4.0s through a mask defining the 200x200 μ m² platforms. Mask and wafer in soft contact.
- Develop:** The photoresist is developed in a solution of 1 AZ 351B : 4 DI-water at 22°C for 1m20s, followed by 2m rinse in DI-water and 1m30s spin dry.
- Silicon etch:** The platforms are transferred to the silicon wafer by ICPRIE for 30s. The ICPRIE setting is given in the table below, where SF₆ and O₂ act as etching gases and C₄F₈ acts as preservation gas. The etch and preservation gas ratio results in scalloping side walls with high aspect ratio (see SEM image to the right) and in a 2 μ m/min etch rate.



Pulsed gases		Pulsed			Regulation mode		Power		LF generator pulsed			
Prio.	Gas	Inactiv [sccm]	Activ [sccm]	Duration [ms]	Pres. [mbar]	Pos. [%]	Source [W]	Chuck [W]	Chuck h. [W]	Chuck h [ms]	Chuck l. [W]	Chuck l. [ms]
1	C4F8	60	200	0.8	-	100	1200	-	90	10	0	90
	O2	0	25	0.8								
2	SF6	300	0	2.8	-	100	1200	-	90	10	0	90

- Photoresist strip:** The photoresist is striped in acetone together with ultrasonic treatment, followed by 2m rinse in DI-water and 1m30s spin dry.
- Photoresist:** AZ 5214E photoresist is deposited by spin coating at 4000rpm for 30s and prebaked at 90°C for 60s.

The transfer test substrates are cut out by means of a dicing saw in 5x5mm² pieces. The last photoresist step is done in order to protect the surface of the device. The photoresist is striped just before nanofibers are stamped onto the test substrate.

Field Effect Transistor (FET) device for bottom contact configuration

Wafer: Si(100) n-doped (antimony) 4" wafer, thickness 500 μ m, with 100nm SiO₂ on top.

1. **HMDS:** Hexamethyldisilazane treatment for 30min. at 120°C.
2. **Photoresist:** AZ 5214E photoresist is deposited by spin coating at 4000rpm for 30s and prebaked at 90°C for 60s.
3. **Photolithography:** The photoresist is exposed to UV light for 4.2s through a mask defining the platforms. Mask and wafer in soft contact.
4. **Develop:** The photoresist is developed in a solution of 1 AZ 351B : 4 DI-water at 22°C for 1m20s, followed by 2m rinse in DI-water and 1m30s spin dry.
5. **SiO₂ etch:** The platforms are transferred to the SiO₂ layer by etching in BHF for 2m20s (etch rate approximately 50nm/min), followed by 10m rinse in DI-water and 1m30s spin dry.
6. **Silicon etch:** The platforms are transferred to the silicon wafer by ICPRIE for 30s. The ICPRIE setting is given in the table below, resulting high aspect ratio etching and in a 2 μ m/min etch rate.

Pulsed gases		Pulsed			Regulation mode		Power		LF generator pulsed			
Prio.	Gas	Inactiv [sccm]	Activ [sccm]	Duration [ms]	Pres. [mbar]	Pos. [%]	Source [W]	Chuck [W]	Chuck h. [W]	Chuck h [ms]	Chuck l. [W]	Chuck l. [ms]
1	C4F8	60	200	0.8	-	100	1200	-	90	10	0	90
	O2	0	25	0.8								
2	SF6	300	0	2.8	-	100	1200	-	90	10	0	90

7. **Photoresist strip:** The photoresist is striped in acetone together with ultrasonic treatment, followed by 2m rinse in DI-water and 1m30s spin dry.
8. **HMDS:** Hexamethyldisilazane treatment for 30min. at 120°C.
9. **Photoresist:** AZ 5214E photoresist is deposited by spin coating at 4000rpm for 30s and prebaked at 90°C for 60s.
10. **Photolithography:** The photoresist is exposed to UV light for 2.0s through a mask defining the source and drain bonding pads on the elevated platforms and the backgate bonding pads on the silicon. Mask and wafer in soft contact. Inversion baked at 130°C for 1m40s, followed by UV flood exposure for 25s.
11. **Develop:** The photoresist is developed in a solution of 1 AZ 351B : 4 DI-water at 22°C for 1m, followed by 2m rinse in DI-water and 1m30s spin dry.
12. **Metal deposition:** 2nm titanium is deposit by *physical vapor deposition* (PVD) at 1Å/s, followed by the deposition of 30nm gold at 2Å/s.

13. **Lift-off:** The metal is lifted in acetone together with ultrasonic treatment, followed by 2m rinse in DI-water and 1m30s spin dry.
14. **HMDS:** Hexamethyldisilazane treatment for 30min. at 120°C.
15. **Photoresist:** AZ 5214E photoresist is deposited by spin coating at 4000rpm for 30s and prebaked at 90°C for 60s.
16. **Photolithography:** The photoresist is exposed to UV light for 4.2s through a mask defining the electrodes. Mask and wafer in soft contact.
17. **Develop:** The photoresist is developed in a solution of 1 AZ 351B : 4 DI-water at 22°C for 1m20s, followed by 2m rinse in DI-water and 1m30s spin dry.
18. **Metal deposition:** 2nm titanium is deposited by PVD at 1Å/s, followed by the deposition of 30nm gold at 2Å/s.
19. **Lift-off:** The metal is lifted in acetone together with ultrasonic treatment, followed by 2m rinse in DI-water and 1m30s spin dry.
20. **Photoresist:** AZ 5214E photoresist is deposited by spin coating at 4000rpm for 30s and prebaked at 90°C for 60s.

The FET devices are cut out by means of a dicing saw in 5x5mm² pieces. The last photoresist step is done in order to protect the surface of the device. The photoresist is striped just before nanofibers are stamped onto the device.

Field Effect Transistor (FET) device for top contact configuration

Wafer: Si(100) n-doped (antimony) 4" wafer, thickness 500 μ m, with 100nm SiO₂ on top.

Step **1** to step **13** is similar to the steps in the *Field Effect Transistor (FET) device for bottom contact configuration* recipe, creating the elevated platforms and the source, drain and backgate bonding pads.

14. Photoresist: AZ 5214E photoresist is deposited by spin coating at 4000rpm for 30s and prebaked at 90°C for 60s.

The FET devices are cut out by means of a dicing saw in 5x5mm² pieces. The last photoresist step is done in order to protect the surface of the device. The photoresist is striped just before nanofibers are stamped onto the device. After the nanofibers are stamped onto the device, the top electrodes are deposited through a manually aligned custom made silicon-nitride mask by *Physical Vapor Deposition*.

PEEM sample

Wafer: Standard Si(100) 4" wafer with a thickness of 500 μ m.

Step **1** to **7** is similar to the steps in the *Nanofiber transfer test substrate* recipe, creating 5x5mm² silicon substrates with nine 1 μ m elevated 200x200 μ m² squares in the top surface, and the silicon surface is protected by a layer of photoresist

- 8. Photoresist strip:** The photoresist is striped in acetone together with ultrasonic treatment, followed by 2m rinse in DI-water and 1m30s spin dry.
- 9. E-beam resist:** 950 PMMA A4 e-beam resist is deposited by spin coating at 7000rpm for 45s and prebaked at 200°C for 1m60s.
- 10. Patterning:** The PEEM sample pattern is written by use of the focused *Scanning Electron Microscope* e-beam at intensity 300 μ C/cm².
- 11. Develop:** The e-beam resist is developed in a solution of 1 MIBK : 4 IPA at 22°C for 40s, followed by develop stop in IPA for 30s.
- 12. Metal deposition:** 2nm titanium is deposit by PVD at 1Å/s, followed by the deposition of 60nm gold at 2Å/s.
- 13. Lift-off:** The metal is lifted in acetone together with ultrasonic treatment, followed by rinse in DI-water and dried by compressed nitrogen.

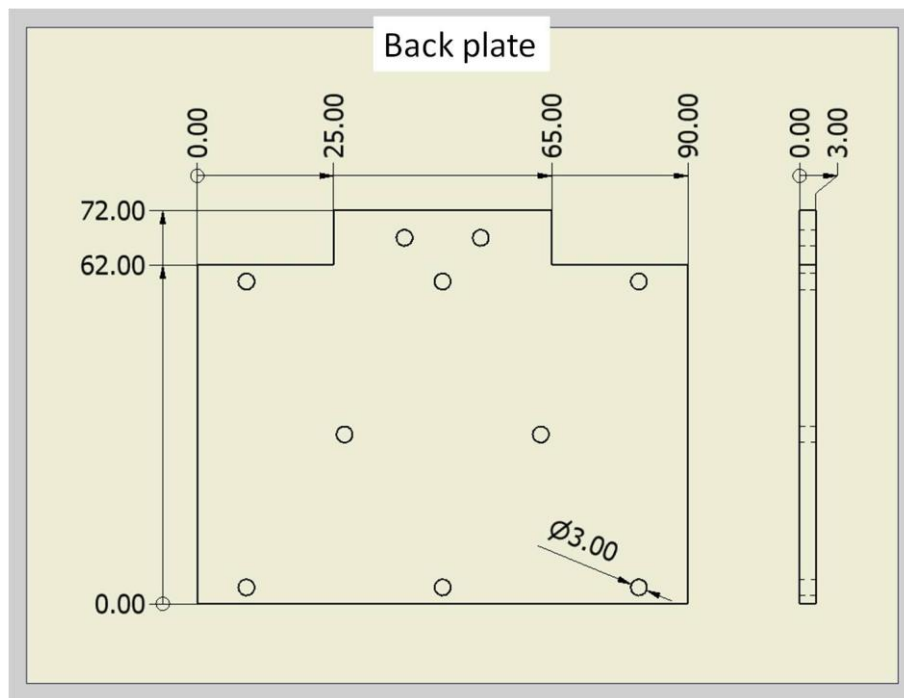
Immediately after p6P nanofibers are stamped onto the PEEM substrate.

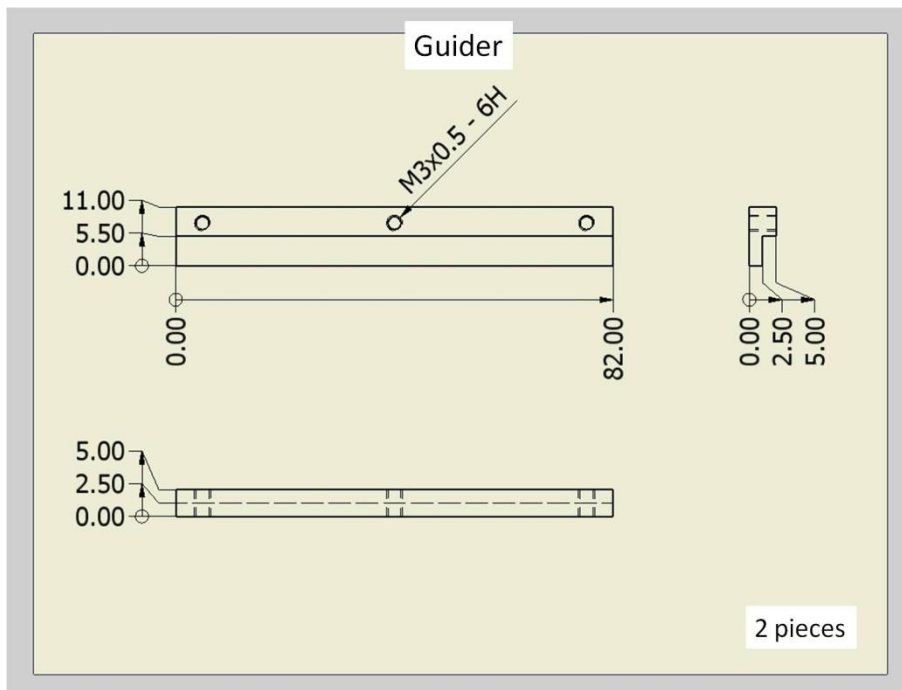
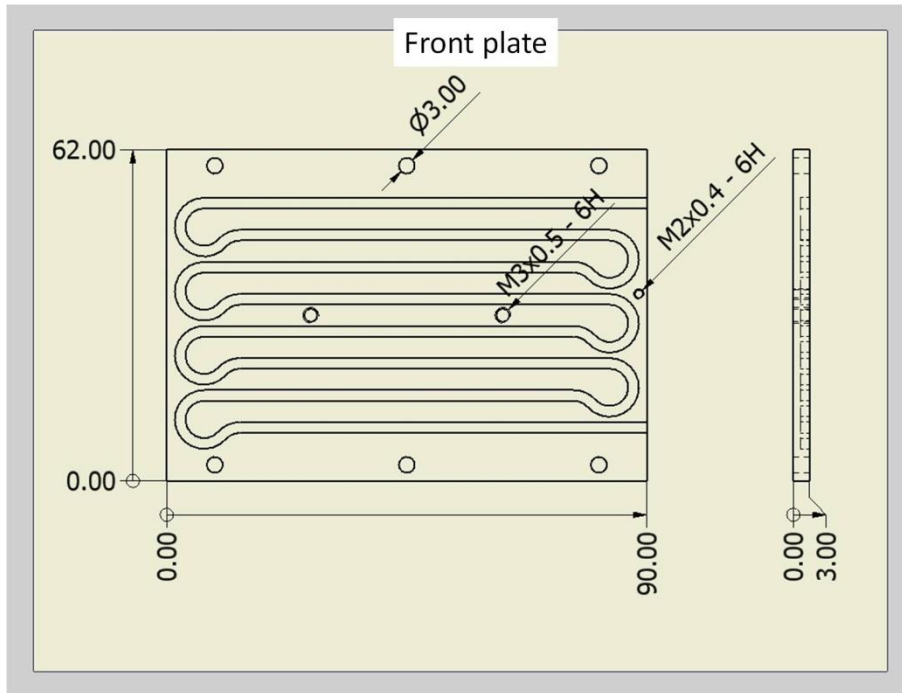
Appendix C

Mechanical drawings

Hotplate

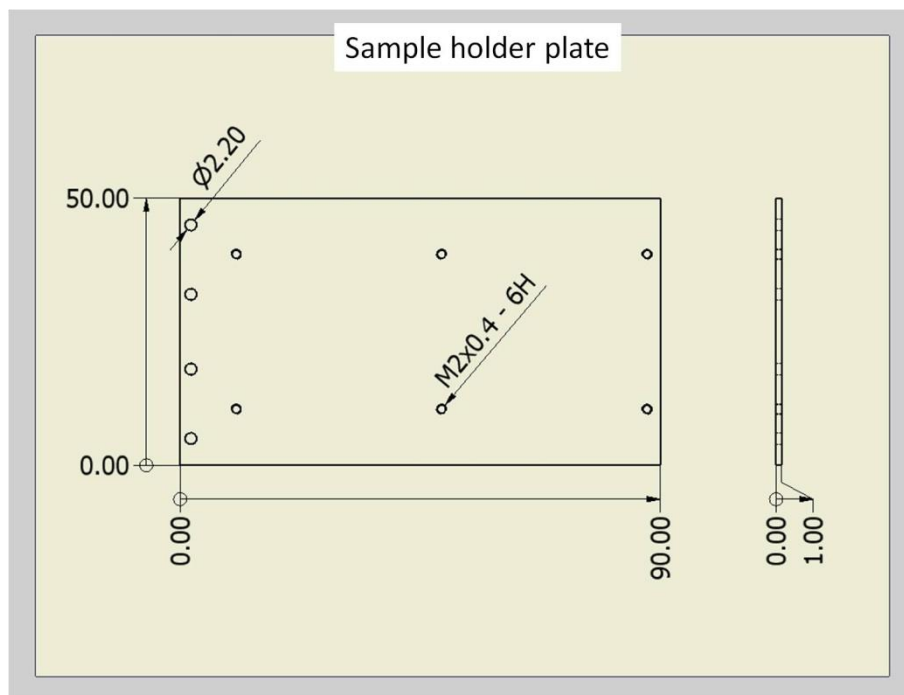
All measurements in the presented drawings are in millimeters.

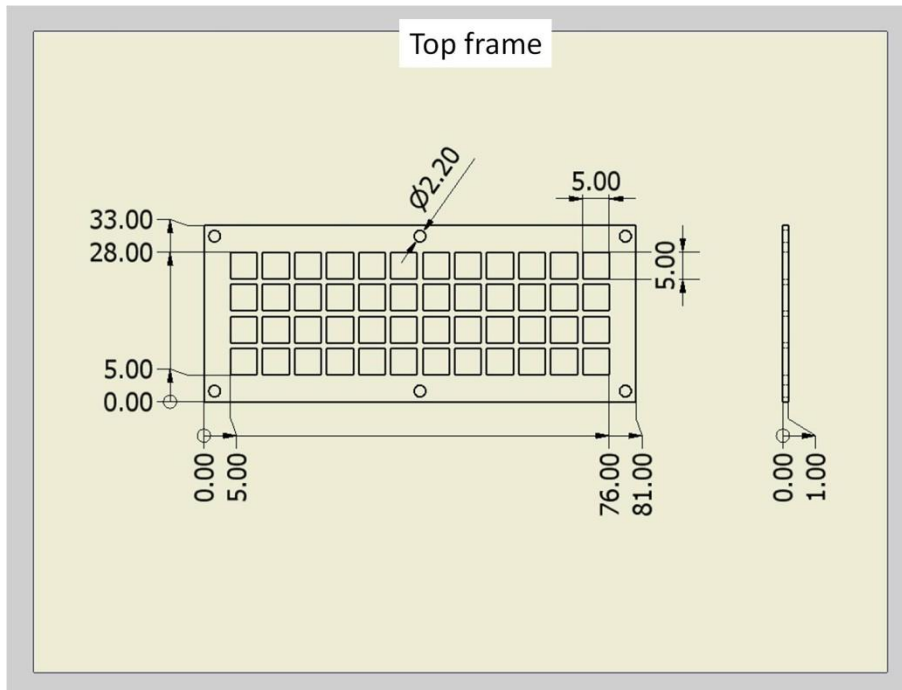
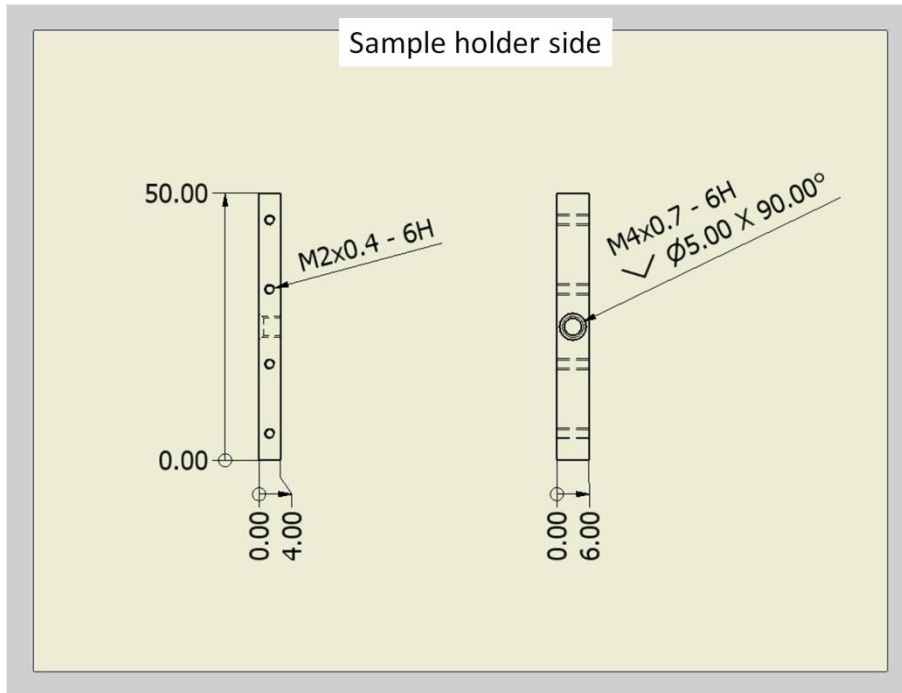




Sample holder

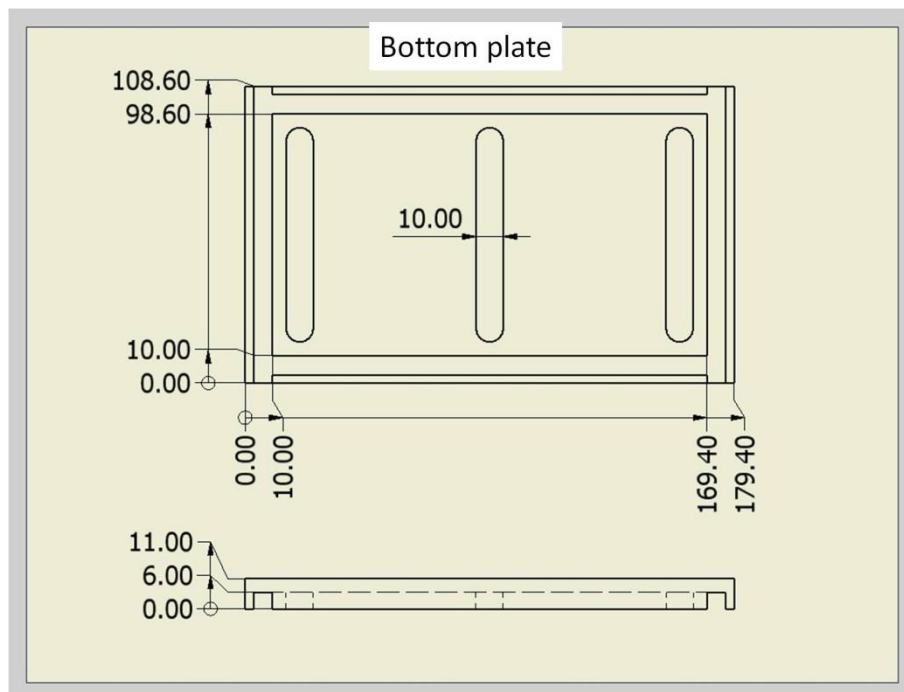
All measurements in the presented drawings are in millimeters.

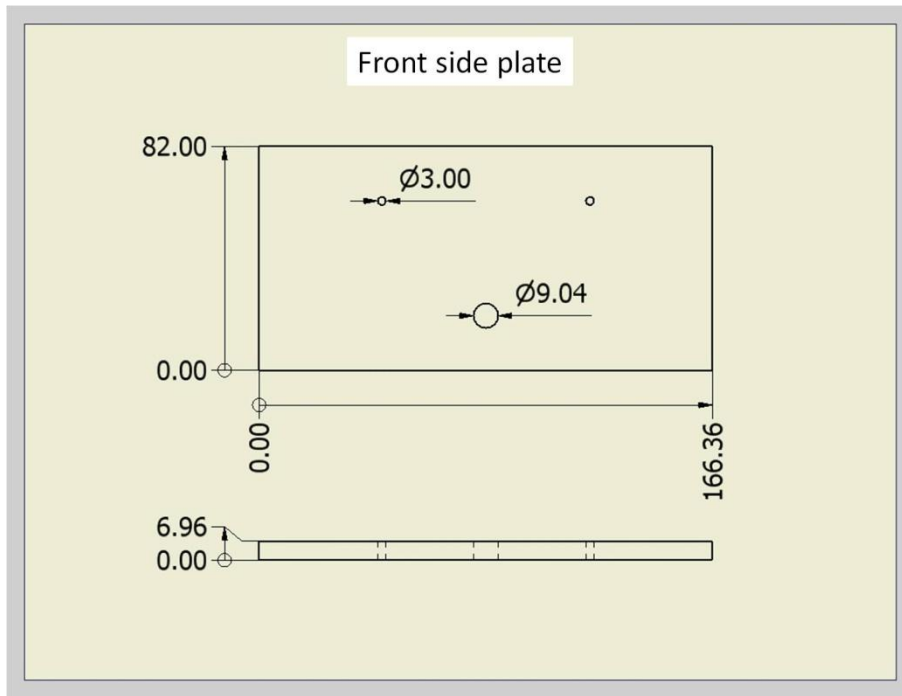
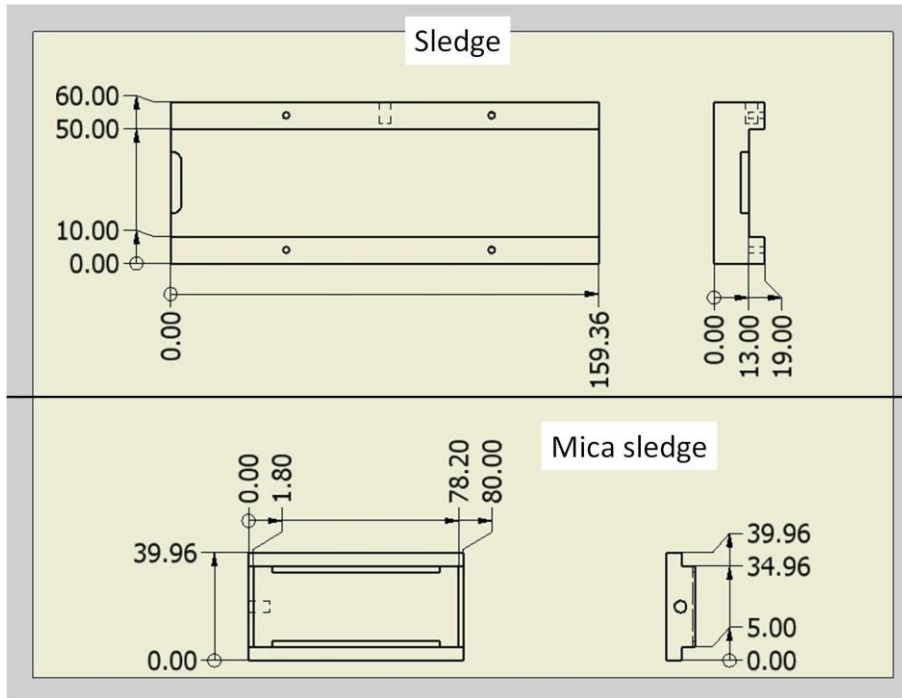


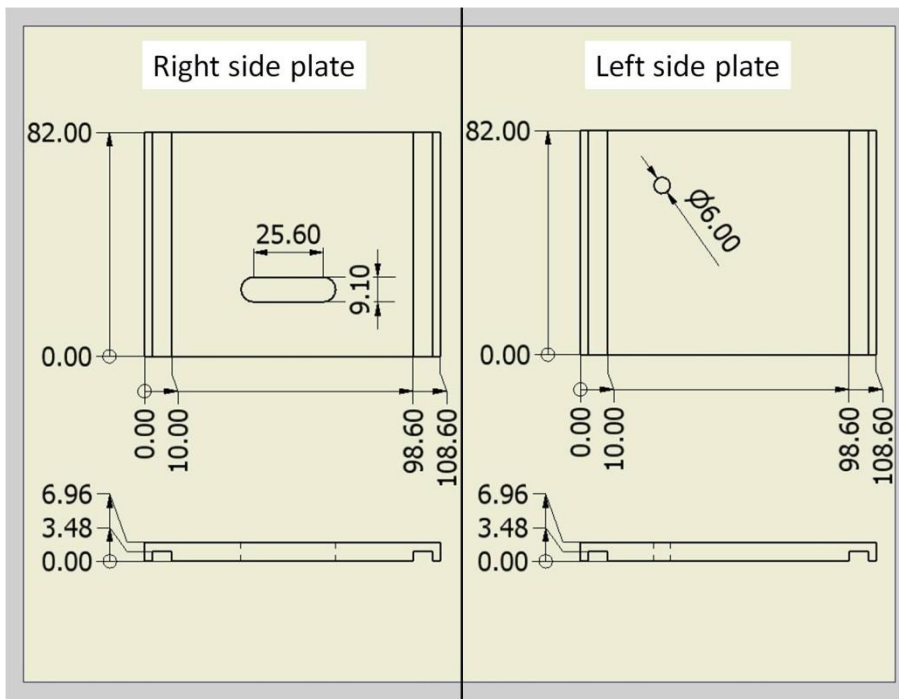
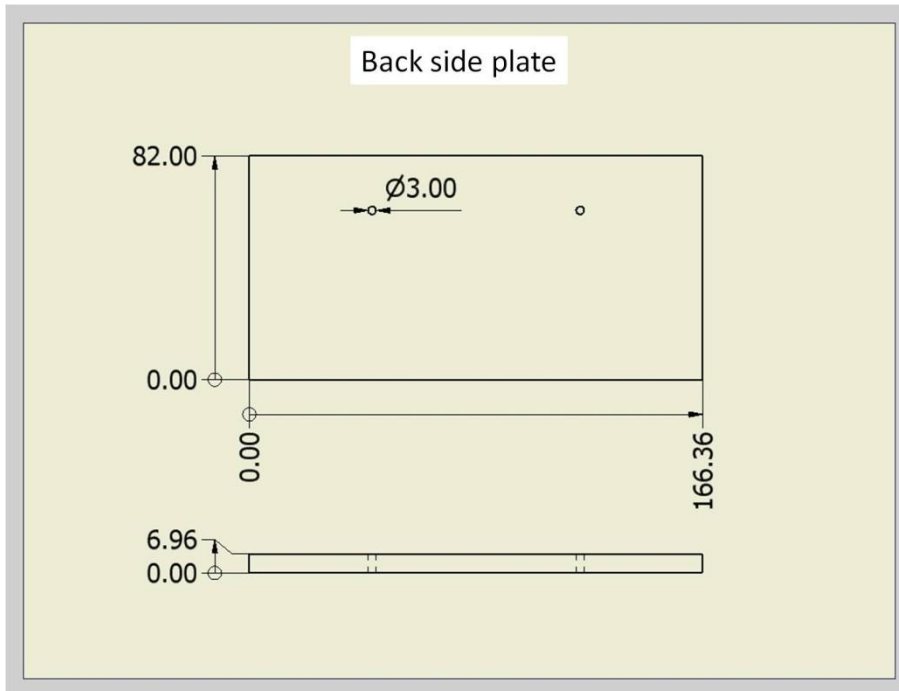


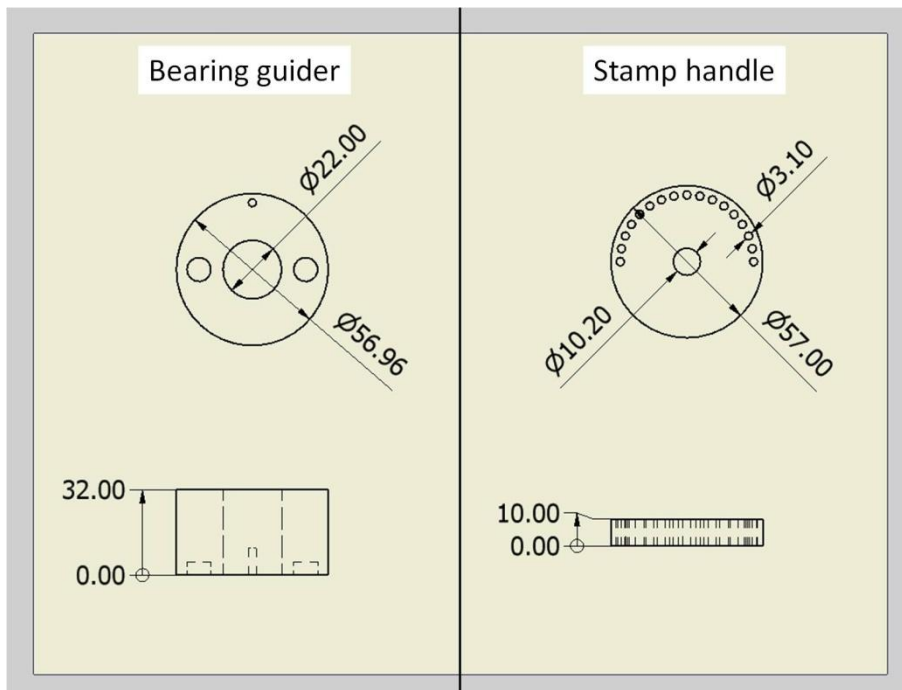
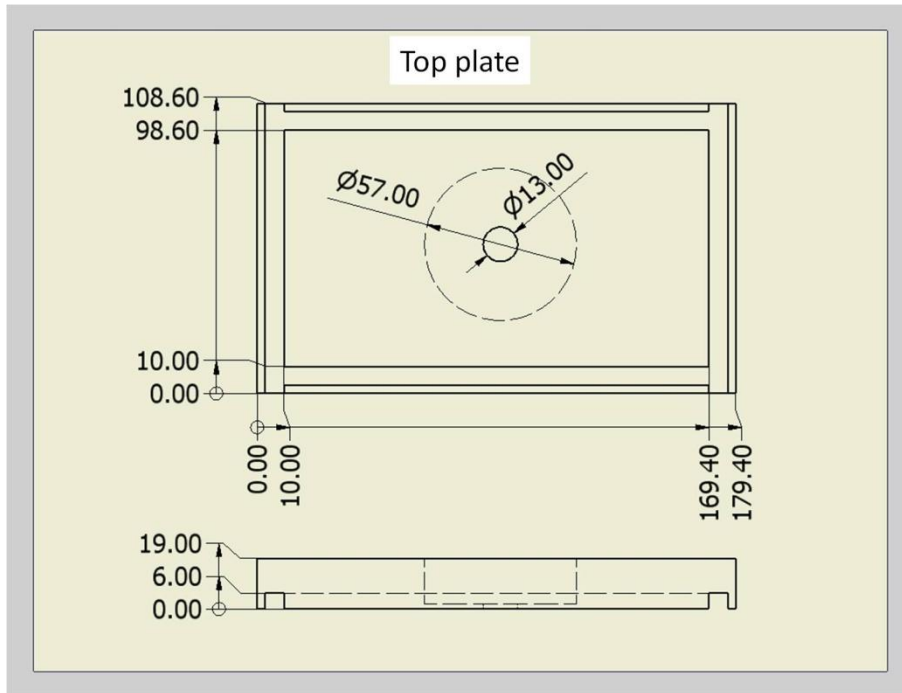
Stamp box

All measurements in the presented drawings are in millimeters.









Bibliography

-
- [1] International technology roadmap for semiconductures, <http://public.itrs.net/>
- [2] Y. Wei and D. Back. *SPIE Newsroom* doi:10.1117/2.1200703.0001.
- [3] M. D. Fischbein and M. Drndic, *Phys. Lett.*, **88**, 063116 (2006).
- [4] H. Schift and A. Kristensen in B. Bhushan (ed.). *Handbook of Nanotechnology*, Chapter 9, Springer (2010).
- [5] S. Iijima. *Nature* **354**, 56 (1991).
- [6] K. Hiruma, T. Katsuyama, K. Ogawa, M. Koguchi, H. Kakibayashi and G. P. Morgan. *Appl. Phys. Lett.* **59**, 431 (1991).
- [7] A. P. Alivisatos. *Science* **271**, 933 (1996).
- [8] BSI British Standards, <http://www.bsigroup.com>
- [9] D. J. Sirbuly, A. Tao, M. Law, R. Fan and P. Yang. *Adv. Mater.* **19**, 61 (2009).
- [10] F. Patolsky, G. Zheng and C. M. Lieber. *Nat. Protoc.* **1**, 1711 (2006).
- [11] Z. Fan, J. C. Ho, Z. A. Jacobsen, H. Razavi and A. Javey. *Proc. Natl. Acad. Sci. U.S.A.* **105**, 11066 (2008).
- [12] J. Hahm and C. M. Lieber. *Nano Lett.* **4**, 51 (2004).
- [13] Z. Chen, J. Appenzeller, Y.-M. Lin, J. Sippel-Oakley, A. G. Rinzler, J. Tang, S. J. Wind, P. M. Solomon and P. Avouris. *Science* **311**, 1735 (2006).
- [14] A. Javey, S. Nam, R. S. Friedman, H. Yan and C. M. Lieber. *Nano Lett.* **7**, 773 (2007).
- [15] B. Tian, T. J. Kempa and C. M. Lieber. *Chem. Soc. Rev.* **38**, 16 (2009).
- [16] M. Law, L. E. Greene, J. C. Johnson, R. Saykally and P. Yang. *Nat. Mater.* **4**, 455 (2005).
- [17] M. Law, D. J. Sirbuly, J. C. Johnson, J. Goldberger, R. J. Saykally and P. Yang. *Science* **305**, 1269 (2004).
- [18] Y. Huang, X. Duan and C. M. Lieber. *Small* **1**, 142 (2005).
- [19] Z. Fan, J. C. Ho, Z. A. Jacobson, R. Yerushalmi, R. L. Alley, H. Razavi and A. Javey, *Nano Lett.* **8**, 20 (2008).

-
- [20] A. L. Briseno, S. C. B. Mannsfeld, C. Reese, J. M. Hancock, Y. Xiong, S. A. Jenekhe, Z. Bao and Y. Xia. *Nano Lett.* **7**, 2847 (2007).
- [21] M. Bendikov, F. Wudl and D. F. Perepichka. *Chem. Rev.* **104**, 4891 (2004).
- [22] G. Barbaralla, M. Melucci and G. Sotgiu. *Adv. Mater.* **17**, 1581 (2005).
- [23] R. Resel. *Thin Solid Films* **433**, 1 (2003).
- [24] F. Balzer and H.-G. Rubahn. *Adv. Funct. Mater.* **15**, 17 (2005).
- [25] J. Kjelstrup-Hansen, O. Hansen, H.-G. Rubahn and P. Bøggild, *Small* **2**, 660 (2006).
- [26] F. Balzer, L. Kankate, H. Niehus, R. Frese, C. Maibohm and H.-G. Rubahn. *Nanotechnology* **17**, 984 (2006).
- [27] S. Müllegger, g. Hlawacek, T. Haber, P. Frank, C. Teichert, R. Resel and A. Winkler. *Appl. Phys. A* **87**, 10 (2007).
- [28] M. Schiek, F. Balzer, K. Al-Shamery, J. R. Brewer, A. Lützen and H.-G. Rubahn. *Small* **4**, 176 (2007).
- [29] A. Andreev, G. Matt, C. J. Brabec, H. Sitter, D. Badt, H. Seyringer and N. S. Sariciftci. *Adv. Mater.* **12**, 629 (2000).
- [30] F. Balzer, K. Al-Shamery, R. Neuendorf and H.-G. Rubahn. *Chem. Phys. Lett.* **368**, 307 (2003).
- [31] F. Balzer, V. Bordo, A. C. Simonsen and H.-G. Rubahn. *Phys. Rev. B* **64**, 115408 (2003).
- [32] M. Era, T. Tsutsui and S. Saito. *Appl. Phys. Lett.* **67**, 2436 (1995).
- [33] D. E. Williams and T. L. Starr. *Computers & Chemistry* **1**, 173 (1977).
- [34] K. N. Baker, A. V. Fratini, T. Resch, H. C. Knachel, W. W. Adams, E. P. Socci and B. L. Farmer. *Polymer* **34**, 1571 (1993).
- [35] A. Niko, F. Meghdadi, C. Ambrosch-Draxl, P. Vogl and G. Leising. *Synthetic Metals* **76**, 177 (1996).
- [36] F. Balzer. "Organic nanoaggregate" Dr. Habilitation, Mathematisch-Naturwissenschaftlichen Fakultät I der Humboldt-Universität zu Berlin
- [37] Y. Kuwahara. *Phys. Chem. Minerals* **26**, 198 (1999).
- [38] F. Pesty and P. Garoche. *Surface Science* **580**, 153 (2005).

- [39] L. Kankate, F. Balzer, Horst Niehus and H.-G. Rubahn. *J. Chem. Phys.* **128**, 084709 (2008).
- [40] F. Balzer, J. Beermann, S. I. Bozhevolnyi, A. C. Simonsen and H.-G. Rubahn. *Nano Lett.* **3**, 1311 (2003).
- [41] J. Podbrdský and V. Draho. *Czech. J. Phys. B* **18**, 1444 (1968).
- [42] C. Teichert, G. Hlawacek, A. Yu. Andreev, H. Sitter, P. Frank, A. Winkler and N. S. Sariciftci. *Appl. Phys. A* **82**, 665 (2006).
- [43] Antique stoves, <http://www.antiquestoves.com/mica/properties/index.htm>
- [44] Wikipedia, http://en.wikipedia.org/wiki/Coefficient_of_thermal_expansion
- [45] T-H Kim, A. Carlson, J.-H. Ahn, S. Wang, Y. Huang and J. A. Rogers. *Appl. Phys. Lett.* **94**, 113502 (2009).
- [46] Z. Fan, J. C. Ho, T. Takahashi, R. Yerushalmi, K. Takei, A. C. Ford, Y.-L. Chueh and A. Javey. *Adv. Mat. Rev.* **21**, 373 (2009).
- [47] M. J. Kim, J. Yoon, S.-I. Park and J. A. Rogers. *Appl. Phys. Lett.* **95**, 214101 (2009).
- [48] Z. Bao, J. A. Rogers and H. E. Katz. *J. Mater. Chem.* **9**, 1895 (1999).
- [49] P. Andersson, R. Forchheimer, P. Tehrani and M. Berggren. *Adv. Funct. Mater.* **17**, 3074 (2007).
- [50] J. Brewer, C. Maibohm, L. Jozefowski, L. Bagatolli and H.-G. Rubahn. *Nanotechnology* **16**, 2396 (2005).
- [51] J. Kjelstrup-Hansen, H. H. Henrichsen, P. Bøggild and H.-G. Rubahn. *Thin Solid Films* **515**, 827 (2006).
- [52] L. Cheng, P. Fenter, K. L. Nagy, M. L. Schlegel and N. C. Sturchio. *Phys. Rev. Lett.* **87**, 156103 (2001).
- [53] S.-H. Park and G. Sposito. *Phys. Rev. Lett.* **89**, 085501 (2002).
- [54] Patent, K. Thilsing-Hansen and H.-G. Rubahn, Nano ink ribbon, Patentnummer: PA 2007 00226.
- [55] Wikipedia, http://en.wikipedia.org/wiki/Dew_point
- [56] Patent, K. Thilsing-Hansen, Storage of Organic Nanofibres, Published.
- [57] P. Yang, R. Yan and M. Fardy. *Nano. lett.* **10**, 1529 (2010).

-
- [58] X. Duan, Y. Huang, R. Agarwal and C. M. Lieber. *Nature* **421**; 241 (2003).
- [59] D. J. Sirbuly, A. Tao, M. Law, R. Fan and P. Yang. *Adv. Mater.* **19**, 61 (2007).
- [60] A. L. Falk, F. H. L. Koppens, C. L. Yu, K. Kang, N. de L. Snapp, A. V. Akimov, M.-H. Jo, M. D. Lukin and H. Park. *Nat. phys.* **5**, 475 (2009).
- [61] J. Zaumseil and H. Sirringhaus. *Chem. Rev.* **107**, 1296 (2007).
- [62] D. R. Lide, *CRC Handbook of Chemistry and Physics*, ISBN 978-1-4200-9084-0.
- [63] N. Koch, E. Zojer, A. Rajagopal, J. Ghjisen, R. L. Johansen, G. Leising and J.-J. Pireaux. *Adv. Funct. Mater.* **11**, 51 (2001).
- [64] T. Yamao, Y. Shimizu, K. Terasaki and S. Hotta. *Adv. Mater.* **20**, 4109 (2008).
- [65] S. A. Maier, *Plasmonics – Fundamentals and Applications*, ISBN 978-0-387-33150-8.
- [66] A. Kubo, N Pontius and H. Petek. *Nano Lett.* **7**, 470 (2007).
- [67] W. Swiech, G. H. Fecher, Ch. Ziethen, O. Schmidt, G. Schönhense, K. Grzelakowski, C. M. Schneider, R. Frömter, H. P. Oepen and J. Kirschner. *Journal of Electron Spectroscopy and Related Phenomena* **84**, 171 (1997).
- [68] P. B. Johnson and R. W. Christy. *Phys. Rev. B* **6**, 4370 (1972).
- [69] V. G. Bordo. *Phys. Rev. B* **81**, 035420 (2010).
- [70] M. Schiek, A. Lützen, R. Koch, K. Al-Shamery, F. Balzer, R. Frese and H.-G. Rubahn, *Appl. Phys. Lett.* **86**, 153107 (2005).
- [71] M. Schiek, A. Lützen, K. Al-Shamery, F. Balzer and H.-G. Rubahn. *Cryst. Growth Des.* **7**, 229 (2007).
- [72] Stensborg A/S. <http://stensborg.com>